Numerical Investigations of $U(1)$ Lattice Gauge Theory

A Thesis

submitted to
Indian Institute of Science Education and Research Pune
in partial fulfillment of the requirements for the
BS-MS Dual Degree Programme

by

Amogh Rakesh

Indian Institute of Science Education and Research Pune
Dr. Homi Bhabha Road,
Pashan, Pune 411008, INDIA.

May, 2024

Supervisor: Prof. Debasish Banerjee

Certificate

This is to certify that this dissertation entitled "**Numerical Investigations of U(1) Lattice Gauge Theory"** towards the partial fulfilment of the BS-MS dual degree programme at the Indian Institute of Science Education and Research, Pune represents work carried out by Amogh Rakesh at Saha Institute of Nuclear Physics under the supervision of Prof. Debasish Banerjee, Theory Division, Saha Institute of Nuclear Physics during the academic year 2023-2024

Debasish Banerjee

Debasish Banerjee

Committee:

Prof. Debasish Banerjee

Prof. Sreejith GJ

Declaration

I hereby declare that the matter embodied in the report entitled "**Numerical Investigations of U(1) Lattice Gauge Theory**" are the results of the work carried out by me at Saha Institute of Nuclear Physics under the supervision of Prof. Debasish Banerjee, Theory Division, Saha Institute of Nuclear Physics, and the same has not been submitted elsewhere for any other degree. Wherever others contribute, every effort is made to indicate this clearly, with due reference to the literature and acknowledgement of collaborative research and discussions.

Amogh Rakesh

(20191094)

This thesis is dedicated to all my teachers, who may or may not bear that label.

Acknowledgements

This Master's thesis marks the culmination of my five-year journey at IISER Pune, and it wouldn't have been possible without the invaluable support of several individuals.

Firstly, I would like to thank my supervisor, Prof. Debasish Banerjee, for being a supportive mentor. Due to his encouragement, I was able to explore a new area during this project. Throughout this project, he has patiently answered my several questions about physics, computations, and data analysis. I am also thankful to him for hosting me at the institute. I am grateful to Dr. Aditya Banerjee for his guidance throughout the project. I am thankful for the many physics and non-physics discussions with him that helped me appreciate the broader context of my work.

I want to thank Sandip and Pallabi for helping me figure out the nuts and bolts of numerical simulations. Alessandro Mariani's notes were very helpful for my calculation of the duality mapping. I am also thankful to Chitranshi, Emanuel, and Shubhabrata for their companionship outside work.

I am grateful to the Saha Institute of Nuclear Physics for providing access to their computing cluster, which was extensively used for this project. I would like to thank the Department of Science and Technology, Government of India, for their financial support through the INSPIRE-SHE program over the past five years.

I am grateful to Prof. Sreejith GJ for introducing me to field theory and many-body physics. My projects under his supervision helped me to build a firm foundation in the subject. I would also like to thank him for agreeing to be the expert on this thesis. I am indebted to Prof. Deepak Dhar for teaching me about phase transitions and Renormalization Group. Along with physics, he also taught me how to bring clarity and precision to my thinking, presentation and arguments. I owe a huge chunk of my understanding of the field to both.

I am grateful for the vibrant atmosphere of the IISER campus, which has allowed me to meet several wonderful people. I would like to thank Aditya, Amogh Ranade, Aniketh, Garvit, Neev, Varun, Vasudha, Vatsal, Pallav, Divyansh and Jezer for their constant support, encouragement and banter through the years. I am grateful to Krishna for introducing me to quizzing and his texts about the most random topics. I am thankful for the many discussions with Parijat, which helped me appreciate the experimentalist's perspective.

Mimamsa played a huge role during my time at IISER. I am indebted to my seniors at physics

Mimamsa – Sugat and Varun, who have greatly influenced my approach to physics. I would also like to thank the rest of the physics Mimamsa gang – Soumil, Kaustubh, Dhruv, Dhairya, and others.

I am indebted to appa and amma for nurturing my curiosity and their unconditional support and encouragement. I would also like to thank the rest of my friends and family for their support through the years.

Finally, I would like to thank Ananda for creating this Latex template, and Vatsal for ensuring that Latex doesn't get the better of me.

Abstract

$U(1)$ Lattice Gauge Theory in three dimensions is a simple model that exhibits the non-trivial phenomenon of confinement. In this thesis, I numerically study this model using an extended action,

$$S = -\sum_{p} \left(\beta \cos\theta_p + \gamma \cos 2\theta_p\right) \quad .$$

This model is mapped to a dual height model defined on the dual lattice, whose partition function is given by

$$Z = \sum_{\{h_{\tilde{s}} \in \mathbb{Z}\}} \prod_{\tilde{\ell}} I^{\gamma}_{(\mathrm{d}h)_{\tilde{\ell}}}(\beta) \quad .$$

I study the effect of γ on the mass gap by performing Monte Carlo simulations of the dual model on a cubic lattice. It will be shown that γ allows us to probe the continuum behaviour of the system at relatively small β. An effective coupling β^* will also be computed using the scaling of the mass gap.

This model is also studied on a three dimensional 'triangular' lattice. In order to validate the simulations, a strong-coupling expansion calculation is performed.

I also provide a brief introduction to Lattice Field Theory and give a brief overview of the physics of 3D $U(1)$ Lattice Gauge Theory in terms of monopoles.

Contents

List of Figures

List of Tables

Notation and Conventions

We collect our definitions and conventions in this section.

Throughout this thesis, we will work in Euclidean spacetime. Except for chapter 8, we will use a cubic lattice with $L_s^2 \times L_t$ sites with periodic boundary conditions. The lattice spacing is denoted by a (or, a_t and a_s). We will usually set $a = 1$. The spatial extent of the lattice is $a_s L_s$ and the temporal extent is $a_t L_t$. We use μ to label any spacetime direction. If we need to be specific, we will use $\hat{x}$, $\hat{y}$ and $\hat{t}$. The edges for the 2D triangular lattice will be along $\hat{x}$, $\hat{l}$ and $\hat{m}$.

We use $\theta_\mu(x)$ to denote an angular link-variable defined on a link $(x; \hat{\mu})$ projecting out from the site x along the $\hat{\mu}$ direction. We use $\theta_{\mu\nu}(x)$ to denote a plaquette-variable defined on a plaquette made up of the links $(x; \hat{\mu})$ and $(x; \hat{\nu})$. We adopt the following convention:

$$\theta_{-\mu}(x) = -\theta_\mu(x - \hat{\mu}) \quad .$$

We will also use θ_ℓ and θ_p to label generic link and plaquette-variables respectively.

Repeated indices aren't usually summed over.

Chapter 1

Introduction

> I wanted to learn about elementary particles
> by studying boiling water.
>
> Alexander Polyakov [1]

Gauge theories play an important role in many areas of physics. The Standard Model of particle physics is a gauge theory with a non-Abelian gauge group $SU(3) \times SU(2) \times U(1)$. In condensed matter physics, besides the fundamental electromagnetic field in systems such as superconductors, effective gauge theories are used to describe the low-energy behaviour of systems such as spin liquids, frustrated magnets, quantum Hall systems, etc.

Asymptotic freedom is a key feature of non-Abelian gauge theories in four spacetime dimensions, which implies that these theories are strongly coupled at low energies. Amongst other things, this means that it is impossible to compute the properties of the proton from QCD using standard perturbative techniques. Hence, we turn to numerical simulations. Lattice Gauge Theory (LGT) is a lattice regularization of gauge theories introduced by Wilson [2], which allows us to study gauge theories numerically.

$U(1)$ LGT in three dimensions is a confining theory like $SU(N)$ gauge theories in four dimensions. Due to its Abelian gauge group, it allows us to study paradigmatic properties of confinement in a simpler context. Moreover, it has been extensively studied analytically and numerically (some

examples are [3, 4, 5, 6, 7, 8, 9]).

While the study of LGT using Monte Carlo simulations has been very successful, this method suffers from sign problems for systems with theta terms, finite chemical potential, etc. Recently, there have been efforts to side-step this issue by performing digital and analogue quantum simulations of Lattice Gauge Theories [10, 11, 12]. Due to its simplicity and non-trivial behaviour, 3D $U(1)$ LGT is a good candidate for performing proof of concept studies.

In this thesis, we study a 3D $U(1)$ Lattice Gauge Theory using an extended action. This local action, containing a Wilson term and an 'adjoint' term, has two couplings — β and γ. The γ coupling present in the adjoint term proves useful in two ways:

1. It serves as an extra parameter which allows us to tune physical quantities such as glueball masses and the string tension.
2. It brings the system closer to the continuum limit even at finite β.

We map our $U(1)$ LGT to a dual integer height model and study the effect of γ on the mass gap by simulating this dual model.

If we consider an experimental implementation of the 2 + 1 dimensional LGT, it is easier to implement it on a triangular lattice than a square lattice in the link basis. This is because the former involves a three-body interaction as compared to a four-body interaction for the latter. In order to simulate such a system, we study the $U(1)$ LGT on a 3D 'triangular' lattice. We also perform a strong-coupling expansion calculation on this lattice to validate our simulations.

The rest of this thesis is organised as follows:

- Chapter 2 provides an introduction to Lattice Field Theory. After warming up with a scalar theory, we motivate and construct the lattice action for a gauge theory.
- Chapter 3 gives an overview of 3D $U(1)$ Lattice Gauge Theory. We introduce the system and briefly discuss the various quantities to be measured in our simulations and their physical interpretations. Finally, we give a heuristic overview of the confining behaviour of this system and discuss the scaling of the mass gap and the string tension.
- Chapter 4 introduces the key ideas behind Markov chain Monte Carlo methods. We also discuss the algorithms which will be used in our simulations.

- Chapter 5 introduces the extended action for the $U(1)$ LGT. The results from our simulation of this model are also discussed.
- Chapter 6 presents the duality mapping from the $U(1)$ LGT to the dual height model. It uses the lattice differential forms formalism, which is explained in the appendix.
- Chapter 7 contains the main results of this thesis. It discusses the simulations of the dual model, and presents the results for the mass gap and the effective coupling.
- Chapter 8 introduces the triangular lattice. A strong-coupling calculation is performed and the simulation of the models is discussed.

Chapter 2

Quantum Fields on the Lattice

> In order to know the truth, it is necessary to imagine a thousand falsehoods.
>
> Sidney Coleman [13]

In this chapter, we will introduce the notion of lattice regularization of quantum fields. It would be instructive to first discretize scalar fields. After this, we will consider gauge fields on the lattice. This discussion can be found in standard textbooks [14][15][16][17]. We largely follow the textbook by Jan Smit [15].

Lattice Gauge Theory (LGT) was introduced by Wilson[2] as a tool to study the strong coupling behaviour of QCD such as confinement. The lattice regularization involves defining the field theory on a discrete mesh of lattice points instead of a continuum spacetime. Although treating spacetime as a discrete lattice seems artificial, it is a useful mathematical trick to study strongly coupled field theories. The lattice provides us with the only way to non-perturbatively regularize field theories. It also offers us the practical benefit of allowing numerical computations via Monte Carlo simulation.

We need to formulate the lattice theory in such a way that it has the same symmetries as the continuum theory. If we do this, wisdom from the Renormalization Group (RG) says that we will recover the same long-distance physics at the critical point. If the lattice theory has a critical point, then tuning the system to the critical point will enable us to extract the universal continuum physics.

At the critical point, the behaviour of the system is governed by long wavelength excitations. As a result, the underlying lattice structure gets washed away. Although the continuum limit corresponds to tuning the lattice spacing a to 0, in practice we accomplish this by tuning the bare coupling which changes with length scales. Since Non-Abelian gauge theories in 4D posses the property of asymptotic freedom, their continuum limit corresponds to tuning the bare-coupling to 0. We will see that for the $U(1)$ LGT in 3D, a continuum limit can be taken in this manner. While performing this tuning, it is necessary to set the proper scale by holding some quantity fixed. This requires us to understand the RG behaviour of the system.

There are two possible approaches to discretization:

- **Path Integral Approach:** We discretize the d dimensional spacetime and study the 'classical' statistical mechanics problem on the lattice. This allows us to study the discrete approximation of the path integral which is invariant under the Euclidean counterpart of Lorentz group.

- **Hamiltonian Approach:** We discretize space, while keeping time continuous. This reformulates the field theory as an n-body quantum system described by a Hamiltonian. This preserves the Hilbert space structure, but we lose explicit Lorentz invariance.

Note that in both approaches, the continuous rotational symmetry (the Euclidean counterpart to Lorentz group) is explicitly broken, but can be recovered as the lattice spacing vanishes, $a \to 0$.

In this thesis, we will only consider the Path Integral approach. If we consider lattices with different spatial and temporal lattice spacings (a_s and a_t), it is possible to recover the Hamiltonian description in the limit of $a_t/a_s \to 0$. We can use the *Transfer operator* formalism to do this.

2.1 Lattice Conventions

We will work in Euclidean spacetime. Unless stated otherwise, we will use a d dimensional, cubic lattice Λ with lattice spacing a to discretize the spacetime. We can imagine this lattice to be embedded in a continuous spacetime. We use $x = (x_1, \ldots, x_d)$ to represent the sites of the lattice and $\hat{\mu}$ to denote the unit vectors on the lattice.

2.2 Scalars on the Lattice

Let us consider a free complex scalar field. The Euclidean action in the continuum is given by

$$S = \int \mathrm{d}^d x \left\{ \partial_\mu \phi^\dagger \partial_\mu \phi + m^2 \phi^\dagger \phi \right\} \quad . \tag{2.1}$$

We can see that this action has the full symmetry of Euclidean space. In addition, it is also invariant under the action of $U(1)$, i.e., under $\phi(x) \mapsto e^{i\alpha}\phi(x)$.

We will naively discretize Eq. (2.1). The fields now reside on the sites $x \in \Lambda$ of a d dimensional cubic lattice. The partial derivatives are replaced by finite differences

$$\partial_\mu \phi(x) \mapsto \frac{\phi(x + a\hat{\mu}) - \phi(x)}{a} \quad ,$$

and the integral over spacetime is replaced by the sum

$$\int \mathrm{d}^d x \mapsto a^d \sum_x \quad .$$

Hence, we get the lattice action

$$\begin{aligned} S &= \sum_x \left\{ a^{d-2} \sum_\mu (\phi^\dagger(x + a\hat{\mu}) - \phi^\dagger(x))(\phi(x + a\hat{\mu}) - \phi(x)) + a^d m^2 \phi^\dagger(x)\phi(x) \right\} \\ &= -a^{d-2} \sum_{x,\mu} \left(\phi^\dagger(x)\phi(x + a\hat{\mu}) + \phi^\dagger(x + a\hat{\mu})\phi(x) \right) + a^d \sum_x \left(\frac{2d}{a^2} + m^2 \right) \phi^\dagger(x)\phi(x) \ . \end{aligned} \tag{2.2}$$

The partition function is given by

$$Z = \int \mathcal{D}\phi^\dagger \mathcal{D}\, \phi e^{-S} \quad , \tag{2.3}$$

where the measure is defined as

$$\int \mathcal{D}\phi^\dagger \mathcal{D}\phi := \prod_x \int \mathrm{d}\phi_x^\dagger \, \mathrm{d}\phi_x \quad .$$

The partition function (2.3) is a Gaussian integral and the model can be solved exactly. The

propagator in momentum space is given by

$$G(p) = \frac{1}{m^2 + 2a^{-2}\sum_\mu \left(1 - \cos a p_\mu\right)} \quad ,$$

In the continuum limit, $a \to 0$, we get back the familiar form for the propagator:

$$G(p) = \frac{1}{m^2 + p^2} \quad .$$

It can be seen that

$$G(\vec{x}, t) = \sum_{\vec{p}} \frac{e^{i\vec{p}\cdot\vec{x} - \omega t}}{2\sinh\omega} \quad ,$$

where ω is given by

$$\cosh\omega = 1 + \frac{1}{2}\left(m^2 + \sum_j 4\sin^2\frac{p_j}{2}\right) \quad .$$

Note that even for a free theory, lattice corrections mean that the *physical mass* will differ from the bare mass of the theory. However, it can be seen that in the continuum limit $a \to 0$, we recover the familiar dispersion relation

$$\omega = \sqrt{m^2 + \vec{p}^2} \quad .$$

2.3 Gauge Fields on the Lattice

In the previous section, we saw how we can construct the lattice action for scalar fields by naive discretization. It turns out that if we do this to gauge theories, we break gauge invariance. The machinery of renormalization group means that such a theory is unlikely to lead to the correct gauge invariant continuum theory. Hence, we need to write a lattice action which preserves gauge invariance on the lattice. In order to see how this comes about, let us first quickly review the continuum action for gauge fields.

2.3.1 The Continuum Action

In a gauge theory, we require the action to be invariant under local gauge transformations. Given a gauge group G and a scalar $\phi(x)$ in some representation of the group, the gauge transformation is given by

$$\phi(x) \mapsto \Omega(x)\phi(x), \quad \Omega(x) \in G \quad .$$

The free field action,

$$S_0 = \int \mathrm{d}^d x \left\{ \partial_\mu \phi^\dagger \partial_\mu \phi + m^2 \phi^\dagger \phi \right\} \quad ,$$

won't be invariant under the gauge transformation because

$$\partial_\mu \phi(x) \mapsto \Omega(x) \partial_\mu \phi(x) + \partial_\mu \Omega(x) \phi \quad .$$

However, by introducing the gauge field A_μ which takes values in the Lie Algebra of G, and replacing the usual derivative ∂_μ with the covariant derivative D_μ, it is possible to cancel this extra contribution.

Therefore the full action is of the form:

$$S = \int \mathrm{d}^d x \left\{ D_\mu \phi^\dagger D_\mu \phi + m^2 \phi^\dagger \phi + \frac{1}{2g^2 \rho} \operatorname{tr}\left(F_{\mu\nu}^2 \right) \right\} \quad , \tag{2.4}$$

where, the covariant derivative is defined as

$$D_\mu := \partial_\mu - i A_\mu \tag{2.5}$$

and the field-strength tensor is defined as the commutator of D_μ

$$F_{\mu\nu} := \left[D_\mu, D_\nu \right] = \partial_\mu A_\nu - \partial_\nu A_\mu - i \left[A_\mu, A_\nu \right] \quad , \tag{2.6}$$

g is the interaction strength and ρ is a representation-dependent normalization constant for the generators of G, T_ks

$$\operatorname{tr} T_k T_l = \rho \delta_{kl} \quad .$$

The gauge field $A_\mu(x)$ should transform in such a way that, under a gauge transformation

$$\phi(x) \mapsto \phi'(x) = \Omega(x) \phi(x), \quad \phi^\dagger(x) \mapsto \phi'^\dagger(x) = \phi^\dagger(x) \Omega^\dagger(x),$$

$D_\mu \phi$ transforms just like ϕ,

$$D_\mu \phi(x) \mapsto D'_\mu \phi'(x) = \Omega(x) D_\mu \phi(x) \quad . \tag{2.7}$$

This means that we require

$$A_\mu \mapsto A'_\mu = \Omega A_\mu \Omega^\dagger + i \Omega \partial_\mu \Omega^\dagger \quad . \tag{2.8}$$

Using its definition, we note that $F_{\mu\nu}$ transforms as

$$F_{\mu\nu} \mapsto \Omega F_{\mu\nu} \Omega^\dagger \quad .$$

Note that the action for a pure gauge theory,

$$S = \int \mathrm{d}^d x \, \frac{1}{2g^2\rho} \, \mathrm{tr}\Big(F_{\mu\nu}^2\Big) \quad ,$$

is independent of the particular representation of the group being used.

In coming up with the lattice action for gauge fields, we will try to ensure that the lattice covariant derivative also transforms according to Eq. (2.7).

2.3.2 The Lattice Action

We demand that the lattice action be invariant under gauge transformation $\Omega(x) \in G$ acting at each lattice site $x \in \Lambda$ as

$$\phi \mapsto \Omega(x)\phi(x), \quad \phi^\dagger(x) \mapsto \phi^\dagger(x)\Omega^\dagger(x) \quad . \tag{2.9}$$

The free lattice action (2.2) is not gauge invariant because the nearest-neighbour term transforms as

$$\phi^\dagger(x)\phi(x + a\hat{\mu}) \mapsto \phi^\dagger(x)\Omega^\dagger(x)\Omega(x + a\hat{\mu})\phi(x + a\hat{\mu}) \quad .$$

Let us define the lattice covariant derivative D_μ as

$$D_\mu \phi(x) = \frac{1}{a}\big(U_\mu(x)\phi(x + a\hat{\mu}) - \phi(x)\big) \quad , \tag{2.10}$$

where the link-variable $U_\mu(x) \in G$ resides on the directed link as shown in Fig. 2.1. Since we can label a link in two ways, we adopt the following convention:

$$U_{-\mu}(x) = U_\mu^\dagger(x - a\hat{\mu}) \quad . \tag{2.11}$$

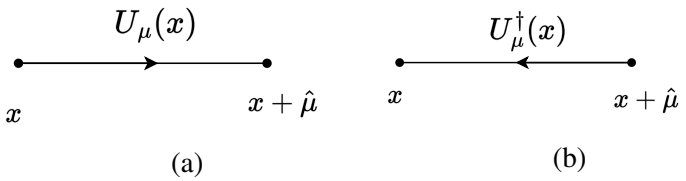

Figure 2.1: Illustration of the nearest-neighbour coupling through the link variables: (a) $\phi^\dagger(x)U_\mu(x)\phi(x+a\hat{\mu})$, (b) $\phi^\dagger(x+a\hat{\mu})U_\mu^\dagger(x)\phi(x)$.

If $U_\mu(x)$ transforms as

$$U_\mu(x) \mapsto \Omega(x)U_\mu(x)\Omega^\dagger(x+a\hat{\mu}) \quad , \tag{2.12}$$

we find that the covariant derivative transforms exactly as Eq. (2.7). We can see that the link-variable plays a similar role to the gauge fields $A_\mu(x)$ in the continuum. If we use this covariant derivative in our action, we get the appropriate lattice action,

$$\begin{aligned} S_s = &- a^{d-2}\sum_x \Big(\phi^\dagger(x)U_\mu(x)\phi(x+a\hat{\mu}) + \phi^\dagger(x+a\hat{\mu})U_\mu^\dagger(x)\phi(x)\Big) \\ &+ a^d \sum_x \Big(2da^{-2}+m^2\Big)\phi^\dagger(x)\phi(x) \quad . \end{aligned} \tag{2.13}$$

Now, the gauge transformation of $\phi(x)$ is cancelled by the transformation of $U_\mu(x)$. As a result, our action is gauge invariant. The nearest neighbour coupling is illustrated in Fig. 2.1.

We can see that the (path-ordered) product of the directed links along the elementary square of

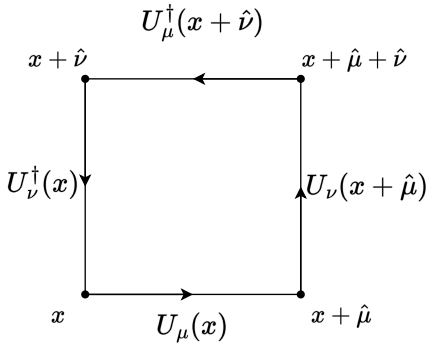

Figure 2.2: The plaquette operator is given by the product of the links.

the lattice, called the *plaquette*, as shown in Fig. 2.2, transforms as

$$\begin{aligned} U_{\mu\nu}(x) &= U_\mu(x)U_\nu(x+a\hat{\mu})U_\mu^\dagger(x+a\hat{\nu})U_\nu^\dagger(x) \\ &\to \Omega(x)U_\mu(x)U_\nu(x+a\hat{\mu})U_\mu^\dagger(x+a\hat{\nu})U_\nu^\dagger(x)\Omega^\dagger(x) \\ &= \Omega(x)U_{\mu\nu}(x)\Omega^\dagger(x) \quad . \end{aligned} \tag{2.14}$$

Therefore, $\operatorname{tr} U_{\mu\nu}(x)$ is gauge invariant. Thus, we can write the simplest action for gauge fields using these plaquette terms:

$$S_g = -\sum_{x,\mu,\nu} \frac{1}{2a^{d-4}g^2\rho} \operatorname{tr}\big(U_{\mu\nu}(x)\big) \quad . \tag{2.15}$$

This known as the *Wilson action*. In general, we could also include products of link-variables over larger loops in our action.

But what exactly is the link-variable $U_\mu(x)$?

2.3.3 Connections to Parallel Transport

Mathematically, the gauge field $A_\mu = A_\mu^k T_k$ is known as a *connection*. These fields inform us how we ought to compare matter fields $\phi(x)$ situated at different points. Suppose we have a test particle which is a vector under the gauge group. As this particle moves along a path C, from x_i to x_f, this vector will evolve through parallel transport

$$w(x_f) = U(x_i, x_f)w(x_i) \quad , \tag{2.16}$$

where the *Wilson line* $U(x_i, x_f)$ which depends on C is given by the path ordered exponential

$$U(x_i, x_f) := \mathcal{P} \exp\left(i \int_{x_i}^{x_f} \mathrm{d}x^\mu \, A_\mu(x)\right) \quad . \tag{2.17}$$

This means that, if we wished to compare our matter fields on neighbouring sites x and $x + a\hat{\mu}$, we would need the Wilson line along the link $x \to x + a\hat{\mu}$. But this is exactly what our link variable does! So, we have

$$U(x, x+a\hat{\mu}) = U_\mu(x) = e^{iaA_\mu(x)} \quad . \tag{2.18}$$

One can also see that the Wilson line obeys the same transformation law as Eq. (2.12). The plaquette operator $\operatorname{tr} U_{\mu\nu}$ corresponds to the Wilson loop along the plaquette.

Now that we know the connection between U_μ and A_μ, we can try to see what the naive continuum limit of the Wilson action Eq. (2.15) looks like. In the limit $a \to 0$, we can use $A_\nu(x + a\hat{\mu}) \approx A_\nu(x) + a\partial_\mu A_\nu(x) + \dots$. Therefore, we have that

$$\begin{aligned} \operatorname{tr}\big(U_{\mu\nu}(x)\big) &= \operatorname{tr} e^{ia^2 F_{\mu\nu}(x)} = \operatorname{tr}\left(1 + ia^2 F_{\mu\nu} - \frac{a^4}{2} F_{\mu\nu}F_{\mu\nu} + \dots\right) \\ &= -\frac{a^4}{2} \operatorname{tr} F_{\mu\nu}F_{\mu\nu} + \dots \quad . \end{aligned} \tag{2.19}$$

Thus, we recover the continuum action at leading order.

Let's bring our attention back to the Wilson action. Using $\sum_p$ to denote a sum over all the plaquettes of Λ, we have

$$\boxed{S_g = -\sum_p \frac{1}{a^{d-4} g^2 \rho} \operatorname{Re}\operatorname{tr}\big(U_p\big)} \quad . \tag{2.20}$$

Note that this action depends on which representation of G we are using. Let's refer to the plaquette operator in the d_r dimensional representation r, by $U_p^{(r)}$. Then the most general, local lattice action would involve a sum over representations r,

$$\boxed{S = \sum_p \sum_r -\frac{\beta_r}{d_r} \operatorname{Re}\operatorname{tr} U_p^{(r)}} \quad , \tag{2.21}$$

which reduces to the classical gauge-field action in the continuum limit, with

$$\boxed{\frac{1}{a^{d-4} g^2} = \sum_r \frac{\beta_r \rho_r}{d_r}} \quad . \tag{2.22}$$

Chapter 3

$U(1)$ Lattice Gauge Theory in 3D

> It has been argued that one of the appeals of science as career is that it enables one to go on playing with toys after the age when it normally ceases to be socially acceptable. Experimentalists are well supplied, although at increasing expense, with toys in the shape of complex apparatus. Theoreticians are expected to be more economical and to make their own; these are the models which all physicists use, modify, reject or justify.
>
> Rudolf Peierls [18]

In the last chapter, we discussed the basic features of Lattice Gauge Theory for a general gauge group G. Now, for the rest of this thesis, we will concern ourselves with the simplest group in the smallest non-trivial dimension – $U(1)$ Lattice Gauge Theory in 3D. In this chapter we will discuss some general features of this system.

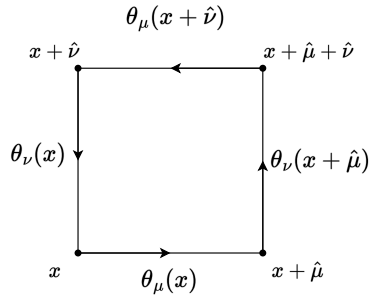

Figure 3.1: The plaquette operator

3.1 The Wilson Action

We will discuss the $U(1)$ Lattice Gauge Theory without matter. The link variables are $U_\mu(x) = e^{i\theta_\mu(x)} \in U(1)$. We will work with the angles, $\theta_\mu(x) \in [-\pi, \pi)$. We discuss this model on a 3D cubic lattice with periodic boundary conditions (PBC). From the previous chapter , we know that the Wilson action is given by

$$\boxed{S = -\beta \sum_p \cos\theta_p} \quad , \tag{3.1}$$

where, β is the interaction strength and θ_p is the angle $\theta_{\mu\nu}(x)$ appearing in the plaquette operator $U_{\mu\nu}(x) = e^{i\theta_{\mu\nu}(x)}$. Since the link and plaquette operators are specified by the angles, we will completely work with the angles and refer to them as the link and plaquette operators.

β is related to the gauge coupling g as

$$\boxed{\beta = \frac{1}{ag^2}} \quad , \tag{3.2}$$

where we introduced the lattice constant a because g^2 has dimensions of mass in 3D.

The plaquette operator $\theta_{\mu\nu}(x)$ is given by a directed sum of the link variables $\theta_\mu(x)$ along the plaquette as illustrated in Fig. 3.1,

$$\boxed{\theta_{\mu\nu}(x) := \theta_\mu(x) + \theta_\nu(x + a\hat{\mu}) - \theta_\mu(x + a\hat{\nu}) - \theta_\nu(x)} \quad . \tag{3.3}$$

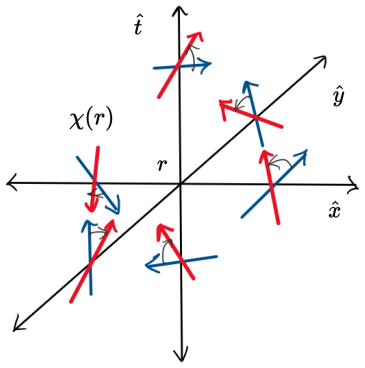

Figure 3.2: Local gauge transformation $\chi(r)$ at site r. Blue arrows denote the initial values, and red arrows denote the transformed values of the link variables.

The partition function for this theory is

$$Z := \int \mathcal{D}\theta \, e^{-S} = \int \mathcal{D}\theta \, e^{\beta \sum_p \cos\theta_p} \quad . \tag{3.4}$$

The integral is over all link variables $\theta_\ell = \theta_\mu(x)$,

$$\int \mathcal{D}\theta \; := \prod_\ell \int_{-\pi}^{\pi} \frac{\mathrm{d}\theta_\ell}{2\pi} \quad . \tag{3.5}$$

3.1.1 Gauge Transformations

For U(1) LGT, the local gauge transformation at site r consists in rotating all fields on the links connected to r by an angle $\chi(r)$. This is illustrated in Fig. 3.2. Under this transformation, a given link variable $\theta_\mu(x)$ transforms as

$$\theta_\mu(x) \mapsto \theta_\mu(x) + \chi(x) - \chi(x + a\hat{\mu}) \quad . \tag{3.6}$$

Note that this looks like the discretized version of the continuum gauge transformation of $A_\mu(x)$. We can see that due to cancellation of χs for different link variables, the plaquette operator $\theta_{\mu\nu}(x)$ is gauge invariant. As a result, the action (3.1) is also gauge invariant.

3.1.2 Naive Continuum Limit

Naively, we should get the continuum limit by taking $a \to 0$. But when we do this, various physical quantities will change as a function of a. To understand the continuum behaviour, we need

to understand how these different quantities scale with each other.

Regardless, it is instructive to see how the action behaves as $a \to 0$. This corresponds to $\beta \to \infty$. In this limit, the fluctuations in $\cos\theta_{\mu\nu}(x)$, and thus in $\theta_\mu(x)$ are heavily suppressed. Hence, by using the Taylor expansion of $\theta_\nu(x + a\hat{\mu}) = \theta_\nu(x) + a\partial_\mu\theta_\nu(x) + \ldots$, we get

$$\theta_{\mu\nu}(x) = a\big(\partial_\mu\theta_\nu(x) - \partial_\nu\theta_\mu(x)\big) + \ldots \quad .$$

Now, if we identify

$$\theta_\mu(x) = aA_\mu(x) \quad , \tag{3.7}$$

we get

$$\theta_{\mu\nu}(x) \approx a^2 F_{\mu\nu}(x) \quad , \tag{3.8}$$

where $F_{\mu\nu}(x)$ is the familiar field-strength tensor.

By using

$$\cos\theta_{\mu\nu}(x) = 1 - \frac{1}{2}\theta_{\mu\nu}(x)^2 + \ldots \quad ,$$

where we are ignoring terms of order a^6 and making the replacement $\sum_x \mapsto a^{-3}\int \mathrm{d}^3x$, we find that the action (3.1) becomes

$$S \approx \int \mathrm{d}^3x\, \frac{1}{4g^2} F_{\mu\nu}F_{\mu\nu} + \text{const.} \tag{3.9}$$

where the repeated indices are summed over. This is exactly the continuum action up to a constant.

Although this analysis validates our action, it ignores the compactness of the gauge field θ_μ. We will look at the effects of this compactness in section 3.4.1. We will also work in lattice units in the rest of our discussion, meaning we set $a = 1$.

3.1.3 Elitzur's Theorem

We would like to understand the phase structure of this theory. Usually, we can understand phase transitions in terms of spontaneous symmetry breaking. However, this is not true in gauge theories for local operators. We need to choose an appropriate extended operator which can show signs of symmetry breaking.

Elitzur's Theorem [19] states that the expectation value for any operator O which is not gauge

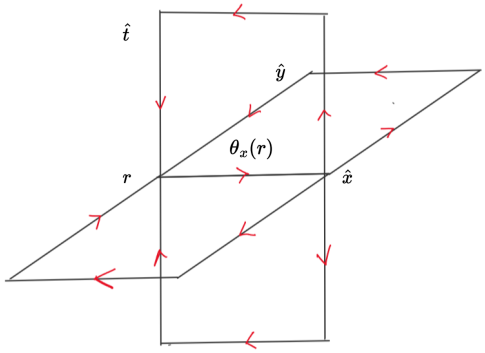

Figure 3.3: The plaquettes containing $\theta_x(r)$

invariant vanishes,

$$\langle \mathcal{O} \rangle = \frac{1}{Z} \int \mathcal{D}\theta \, \mathcal{O} e^{-S[\theta]} = 0 \quad . \tag{3.10}$$

This means that the “gauge symmetry" can never be spontaneously broken. Physically, we should understand that the gauge invariance is not a symmetry of the system but a redundancy in our description. It arises because we have chosen to describe a constrained system in terms of redundant degrees of freedom.

To illustrate this theorem, we will see how this works for the link variable, $\mathcal{O} = \cos\theta_x(r)$. We present a specific version of the general argument provided in [20, Ch. 4]. We want to compute

$$\langle \cos\theta_x(r) \rangle = \frac{1}{Z} \int \mathcal{D}\theta \, \cos\theta_x(r) e^{-S[\theta]} \quad .$$

As shown in Fig. 3.3, the variable $\theta_x(r)$ appears in 4 plaquettes in the action. Consider one such plaquette

$$\theta_{xy}(r) = \theta_x(r) + \theta_y(r + \hat{x}) - \theta_x(r + \hat{y}) - \theta_y(r) \quad .$$

We can remove $\theta_x(r)$ by making the change of variables

$$\theta_y(r) \mapsto \theta_y(r) + \theta_x(r) \quad .$$

Such a change of variable does not change the value of the integral. Similarly, we can make the

following change of variables to remove $\theta_x(r)$ from the remaining 3 plaquettes

$$\begin{aligned}\theta_t(r) &\mapsto \theta_t(r) + \theta_x(r) \quad ,\\ \theta_y(r-\hat{y}) &\mapsto \theta_y(r-\hat{y}) + \theta_x(r) \quad ,\\ \theta_t(r-\hat{t}) &\mapsto \theta_t(r-\hat{t}) + \theta_x(r) \quad .\end{aligned}$$

But doing this results in $\theta_x(r)$ reappearing in some other plaquettes. One can see that these contributions can be removed by making a final change of variable,

$$\theta_x(r-\hat{x}) \mapsto \theta_x(r-\hat{x}) + \theta_x(r) \quad .$$

So, we have made this change to the fields on all the links connected to the site r except $\theta_x(r)$ itself. Thus, we have isolated the contribution of $\theta_x(r)$ to the integral

$$\int_{-\pi}^{\pi} \frac{\mathrm{d}\theta_x(r)}{2\pi} \cos\theta_x(r) = 0 \quad .$$

Hence we see that $\langle \cos\theta_x(r) \rangle = 0$. Generically, any operator which is not gauge invariant will have such free links which integrate to 0.

3.2 Wilson and Polyakov Loops

The previous section tells us that we need to study gauge invariant operators to understand the system. We can construct such operators by taking the product of the link variables $\exp\big(i\theta_\mu(x)\big)$ along a closed loop. This ensures that the gauge transformation of two neighbouring links cancel each other, and the loop as a whole remains gauge invariant.

The *Wilson loop* $W(C)$ is defined as

$$\boxed{W(C) := \exp\left(i \sum_C \theta_\mu(x)\right)} \quad , \tag{3.11}$$

where the sum is over the link variables $\theta_\mu(x)$ on a contractible loop C. We will consider rectangular loops in our simulation. One such loop oriented in the time-like direction is shown in Fig. 3.4. We use $W(r,\tau)$ to denote a rectangular Wilson loop of size $r \times \tau$.

Since we are considering a lattice with PBC, we can also construct a non-contractible loop

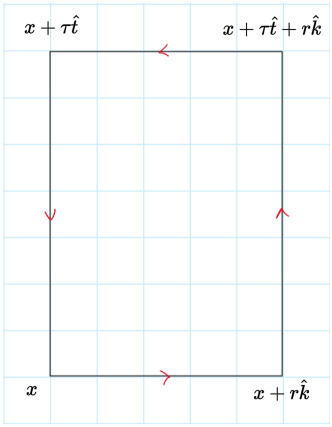

Figure 3.4: A rectangular Wilson loop oriented along the time-like direction.

which winds once around the time direction. The *Polyakov loop* $P(\vec{r})$ is defined as the product of link variables along such a loop,

$$\boxed{P(\vec{r}) := \exp\left(i \sum_{\tau=0}^{T-1} \theta_t(\vec{r}, \tau)\right)} \quad , \tag{3.12}$$

where T is the length of the lattice in the time direction.

3.2.1 Physical Interpretation

In the continuum with real time, an external current J^μ enters the path integral as

$$e^{iS[A_\mu]} \mapsto e^{iS[A_\mu] + i\int \mathrm{d}^3x J^\mu A_\mu} \quad .$$

For a line current along a path $z^\mu(\tau)$,

$$J^\mu(x) = \int \mathrm{d}\tau \, \frac{\mathrm{d}z^\mu}{\mathrm{d}\tau} \delta^3(x - z(\tau)) \quad ,$$

the phase $\exp\left(i \int \mathrm{d}^3x \, J^\mu A_\mu\right)$ takes the form

$$\exp\left(i \int \mathrm{d}z^\mu \, A_\mu(z)\right) \quad ,$$

where the integral is over the path $z^\mu(\tau)$. Now, if we perform Wick rotation by substituting $J^0 = -iJ_4, \mathrm{d}z^0 = -i\,\mathrm{d}z_4\,, A_0 = iA_4$, the phase remains a phase

$$\exp\left(i \int \mathrm{d}z_\mu\, A_\mu(z)\right) \quad . \tag{3.13}$$

Suppose now we choose $J_\mu(x)$ to run along a contractible loop. We can think of this as a charge-anticharge pair getting created, propagating in time, and then being destroyed. The partition function of such a system on the lattice is exactly the expectation value of the Wilson Loop upto a normalization,

$$Z[J] = \int \mathcal{D}\theta\, \exp\left(i \sum_C \theta_\mu(x)\right) e^{-S} = Z(0)\,\langle W(C)\rangle \quad . \tag{3.14}$$

Similarly, if we had taken $J^\mu(x)$ to result from the worldline of a stationary charge situated at $\vec{r}$, we would get the expectation value of the Polyakov loop.

3.2.2 Intercharge Potential

Let's consider a rectangular Wilson loop, $W(C) = W(r,\tau)$ oriented along the time-like direction as illustrated in Fig. 3.4. We saw that the expectation value $\langle W(r,\tau)\rangle$ is related to the ratio of partition functions

$$\langle W(r,\tau)\rangle = \frac{Z[J]}{Z[0]} \quad .$$

We also know that $Z[J]$ is equivalent to $\mathrm{tr}\left(e^{-H\tau}\right)$, where H is the Hamiltonian of the system with the external charges. In the limit $\tau \to \infty$, the partition function projects the system to the lowest state. The energy of this state would be $E_0 + V(r)$, where E_0 is the energy of the vacuum without the charges and $V(r)$ is the potential energy between the charges. Since, E_0 would cancel from the numerator and denominator, we find

$$\boxed{\lim_{\tau\to\infty} \langle W(r,\tau)\rangle \sim e^{-V(r)\tau}} \quad . \tag{3.15}$$

This argument can be made more precise by considering the Hamiltonian lattice formulation. Here, computing $\langle W(r,\tau)\rangle$ amounts to directly measuring the energy of a state containing a charge-anticharge pair connected by gauge fields. This is extensively discussed in standard textbooks [15][16] [17].

A similar analysis shows that this interpretation also holds for the Polyakov loop correlators $\left\langle P^\dagger(\vec{r})P(0)\right\rangle$

$$\boxed{\lim_{T\to\infty}\left\langle P^\dagger(\vec{r})P(0)\right\rangle \sim e^{-V(r)T}} \quad . \tag{3.16}$$

Strictly speaking, $\left\langle P^\dagger(\vec{r})P(0)\right\rangle$ informs us about the energy required to separate the charges at finite temperature.

It has not been rigorously proved that the potential computed using Wilson loops and the potential computed using the Polyakov loops are the same [16]. However, it is known that the Wilson loop potential bounds the Polyakov loop potential from above [21]. In this thesis, we will treat both these potentials on an equal footing.

3.2.3 The Confining and Coulomb Phases

We could have different phases for a pure gauge theory based on how the fields react to the presence of external charges — the *confining* phase and the *Coulomb* phase.

By performing a strong coupling expansion in the limit $\beta \to 0$ [22] , it can be seen that asymptotically for large loops, the leading behaviour of $\langle W(C)\rangle$ is

$$\boxed{\langle W(C)\rangle \sim e^{-cA}} \quad , \tag{3.17}$$

where, A is the area bounded by the loop. This is known as the *area law* behaviour. This can be explained by a potential of the form

$$\boxed{V(r) \approx \sigma r + V_0 + \dots} \quad . \tag{3.18}$$

Since this means that there is a constant force $F \approx \sigma$ between the charges, they cannot be seperated by a large distance and isolated charges are heavily suppressed. This is the confining phase of the theory. σ is known as the *string tension*.

On the other hand, by performing a weak coupling expansion in the limit $\beta \to \infty$ [22] , it can be seen that asymptotically for large loops, the leading behaviour of $\langle W(C)\rangle$ is

$$\boxed{\langle W(C)\rangle \sim e^{-cP}} \tag{3.19}$$

where, P is the perimeter of the loop. This is known as the *perimeter law* behaviour. This can be

explained by a Coulomb potential, which in 3D gives

$$\boxed{V(r) = V_0 + b \log r + \dots} \quad . \tag{3.20}$$

However, as we will see, the weak coupling analysis does not capture the effects of monopoles. In fact, the $U(1)$ LGT confines for all finite β in 3D.

3.3 Glueball Masses

As we will see, the $U(1)$ LGT in 3D is gapped at all finite β. We will use *glueball* to refer to the single particle states. We would like to measure the glueball masses. This is done by measuring the appropriate correlation function.

Suppose that some operator Φ creates the required glueball state by acting on the vacuum. Consider this operator on two time-slices $t = 0$ and $t = \tau$. We find that $\left\langle \Phi^\dagger(\tau)\Phi(0) \right\rangle$ gives us

$$\begin{aligned} \left\langle \Phi^\dagger(\tau)\Phi(0) \right\rangle &= \langle 0|\Phi^\dagger(\tau)\Phi(0)|0\rangle \\ &= \langle 0|e^{H\tau}\Phi^\dagger(0)e^{-H\tau}\Phi(0)|0\rangle \\ &= \sum_n e^{-(E_n - E_0)\tau} |\langle n|\Phi|0\rangle|^2 \quad , \end{aligned}$$

where $|0\rangle$ labels the vacuum, and we have inserted the complete set of energy eigenstates $|n\rangle\langle n|$ to go from line 2 to 3. In the limit $\tau \to \infty$, the contributions from the excited states are suppressed and we have

$$\boxed{\left\langle \Phi^\dagger(\tau)\Phi(0) \right\rangle \approx \langle \Phi(0)\rangle^2 + |\langle p|\Phi(0)|0\rangle|^2 e^{-(E_p - E_0)\tau} + \dots} \quad , \tag{3.21}$$

where $|p\rangle$ is the lowest state such that $\langle p|\Phi(0)|0\rangle \neq 0$. The mass of this state is given by

$$m_p = E_p - E_0 \quad .$$

In our system, it is known that the lightest state has quantum numbers $J^{PC} = 0^{--}$. This is a state with spin $J = 0$, which is antisymmetric under parity P and charge conjugation C operations. We create this state using the operator

$$P_-(\tau) := \frac{1}{L_s^2} \sum_{\vec{r}} \sin\theta_{xy}(\vec{r}, \tau) \tag{3.22}$$

and equate its mass with the mass gap m_D. The sum is over all points on time-slice $t = \tau$. This ensures that we are projecting to 0 momentum.

3.4 Mass Gap, Confinement and the Continuum Limit

In this section, we will discuss some general features of 3D $U(1)$ LGT whose behaviour is driven by instantons. We follow the extensive discussion provided by Athenodorou and Teper [9]. We will present some rigorously proven scaling of the mass gap m_D and the string tension σ with β, and use these to understand the continuum limit of the theory.

The long-distance universal behaviour of the $U(1)$ LGT in 3D is analytically well-understood [3, 4, 5, 6, 7]. These analyses are usually done in the Villain approximation of the Wilson action. This long-distance behaviour is captured in the scaling of m_D and σ.

In the limit $\beta \to \infty$, the scaling of mass gap and string tension was rigorously proved by Gopfert and Mack [6] , and Ito [7] for an infinite cubic lattice. Recall that $\beta = 1/ag^2$, where a is the lattice spacing. It was shown that

$$\boxed{a^2 m_D^2 = 8\pi^2 \beta \exp\{-2\pi^2 v(0)\beta\}} \tag{3.23}$$

and

$$\boxed{a^2\sigma = c' a g^2 a m_D} \quad . \tag{3.24}$$

Here, $c' = 8/\sqrt{2\pi^2}$ and $v(x)$ is the Coulomb potential on the lattice. $v(0) = 0.2527$. These constants were determined by semi-classical analysis.

The fact that the gauge fields $\theta_\mu(x)$ are compact plays a crucial role in the behaviour of the system, as shown by Polyakov [3][4]. He showed that the vacuum of this system is a dilute gas of instantons which are identified with magnetic monopoles. This screened plasma of monopoles leads to both the mass gap and linear confinement. The magnetic field in the plasma is screened with a screening length $l_D \sim m_D^{-1}$.

3.4.1 The Monopoles

Abusing notation, let's denote $\theta_{\mu\nu}$ as $F_{\mu\nu}$. We refer to $\tilde{F}_\mu$, defined by

$$\tilde{F}_\mu := \frac{1}{2}\varepsilon_{\mu\nu\rho}F_{\nu\rho} \quad , \tag{3.25}$$

as the 'magnetic' field.

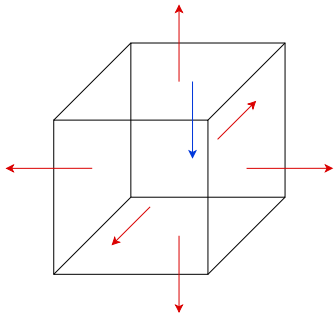

Figure 3.5: The red arrows show the configuration of the magnetic field, $\tilde{F}_\mu$, due to a monopole at the centre of the cubic. The blue arrow shows a value of plaquette which is equivalent to the red arrow on that face, but doesn't indicate a monopole ($-5\pi/$ instead of $\pi/3$).

Note that $F_{\mu\nu}$ are angular variables which are only defined modulo 2π. It can be checked that for a given unit cube c,

$$\sum_{\partial c} F_{\mu\nu}(x) = \sum_{\partial c} \tilde{F}_\mu = 0 \quad . \tag{3.26}$$

Suppose that for some cube, the plaquette value on 5 of its faces are $\pi/3$. So, Eq. (3.26) implies that the plaquette on the 6th face should be $-5\pi/3$. But this is equivalent to a value of $\pi/3 = -5\pi/3 + 2\pi$. In the approximation where the action is

$$S = -\beta \sum_{x,\mu,\nu} F^2_{\mu\nu}(x) \quad ,$$

the choice of $\pi/3$ looks more energetically favourable. This configuration of the magnetic fields on the faces of the cube is illustrated in Fig. 3.5.

Such a configuration of magnetic field $\tilde{F}_\mu$ around c is exactly what one would get if there were a monopole at the centre of the cube. The charge of this monopole is 2π. This leads to the identification of our system with a system of magnetic monopoles and antimonopoles of charge $2\pi q$ with $q \in \mathbb{Z}$, at a temperature β^{-1}. This mapping can be performed precisely by performing a saddle point analysis of the action.

It is known that in a dilute plasma, the magnetic fields are screened by the interaction of opposite charges. This is known as Debye screening. The system then has a screening length l_D, and we can identify the mass gap with the inverse screening length, $m_D = l_D^{-1}$. This is essentially the mass of the glueball which has quantum numbers $J^{PC} = 0^{--}$.

3.4.2 Monopoles and Confinement

We will now present a heuristic argument, provided by Athenodorou and Teper [9], for how monopoles lead to confinement. We need to understand the behaviour of the rectangular Wilson loop $W(r,\tau)$. Its expectation value is given by

$$\begin{aligned}\langle W(r,\tau)\rangle &= \left\langle \exp\left(i \oint_C \mathrm{d}z^\mu \, A_\mu(z) \right) \right\rangle \\ &= \left\langle \exp\left(i \int \mathrm{d}\sigma^{\mu\nu} \, F_{\mu\nu}(x) \right) \right\rangle = \langle \exp(i\Phi_B) \rangle \quad ,\end{aligned}$$

where we have converted the integral over the loop C to an integral over the rectangular area enclosed by C in going to line 2. Φ_B is the total magnetic flux $\int \mathrm{d}n^\mu \, \tilde{F}_\mu$ passing through the rectangular area bounded by the loop. We need to compute this flux from the magnetic fields of the monopoles.

We consider the vacuum to be a dilute gas of monopoles and anti-monopoles of charge $\pm 2\pi$. We make the approximation that Φ_B gets contributions only from (anti-)monopoles inside a slab extending a distance $l_D = m_D^{-1}$ on either side of the Wilson loop, whose fields aren't screened. The (anti-)monopoles outside this slab are assumed to be completely screened. Assuming symmetric fluxes from each (anti-)monopole and in the limit where $r, \tau >> l_D$, half of the (anti-)monopole's flux, i.e. $\pm\pi$ units, will pass through the rectangle. (We are neglecting the monopoles near the boundary). Monopoles and antimonopoles, and those from the upper and lower slabs would contribute independently to the flux. Hence, their contribution to $\exp(i\Phi_B)$ can be factorized.

Since this is a dilute gas, the number of (anti-)monopoles can be assumed to follow a Poisson distribution. Let the probability of finding an isolated monopole anywhere on the lattice be $c(\beta) \propto \exp(-\beta S_M)$, where S_M is the action of an isolated (anti-)monopole. $c(\beta)$ is proportional to the exponential factor $\exp\{-2\pi^2 v(0)\beta\}$ appearing in mass scaling (3.23). The average number of (anti-)monopoles inside the slab would be $n_0 = c(\beta) r \tau l_D$. Each (anti-)monopole gives a factor of $\exp(\pm i\pi) = -1$ to $\exp(i\Phi_B)$. Thus, we estimate

$$\langle \exp(i\Phi_B) \rangle = \left(\sum_n \frac{n_0^n}{n!} e^{-n_0} (-1)^n \right)^4 = e^{-8n_0} = e^{-8c(\beta) l_D r \tau} \quad . \tag{3.27}$$

The exponent 4 comes from the equal and independent contributions of monopoles and anti-monopoles, from upper and lower slabs. Comparing this to Eq. (3.15), we can see that monopoles

cause a linearly confining potential between the charges,

$$V(r) = 8c(\beta) l_D r = \frac{8c(\beta)}{m_D} r = \sigma r \quad , \tag{3.28}$$

where σ is the string tension. Now, since $c(\beta)$ is proportional to $\exp\{-2\pi^2 v(0)\beta\} \propto m_D^2$ in Eq. (3.23), we see that Eq. (3.28) gives us $\sigma \propto m_D$ just as in Eq. (3.24). So, we find that our heuristic calculation with several approximations captures how a screened monopole plasma leads to a linearly confining potential.

3.4.3 The Continuum Limits

It has been shown rigorously [6][7] that the continuum theory is a free field theory of massive particles which show linear confinement at any non-zero lattice spacing. In the $U(1)$ lattice theory, we have several ways to approach the continuum limit $a \to 0$ by choosing which physical length scale to keep fixed. These are the inverse coupling $l_g = 1/g^2$, the inverse string tension $l_\sigma = 1/\sqrt{\sigma}$, the inverse screening mass $l_D = 1/m_D$, and the average seperation between monopoles l_M. The relation between the first three length scales is given in Eqs.(3.23) and (3.24). We see that $l_D \sim g^2 l_\sigma^2$. Since we estimated that the average number of monopoles in a volume V, $n_0 = V/l_M^3$, Eq. (3.28) tells us

$$l_M^3 \sim l_\sigma^2 l_D \quad . \tag{3.29}$$

We would like to see what continuum limit we obtain if we keep each of these scales constant. In doing so, we need to take care to express our lengths and energies in terms of the physical length and energy scales involved.

1. l_g fixed as $a \to 0$
   In this limit, $m_D \to 0$ and similarly $\sigma \to 0$ because of the exponential $\exp(-c/ag^2)$. The average seperation between monopoles also goes to infinity. So, for any fixed length scale r such that $r/l_g < \infty$, there are no monopoles at all as $a \to 0$. The potential energy between external charges would be the logarithmic Coulomb potential and the excitations of the gauge fields are massless photons. However, since g^2 is the bare coupling, this limit is a bit unphysical.

2. l_σ fixed as $a \to 0$

The physical energy scale is $E_\sigma = 1/l_\sigma = \sqrt{\sigma}$. From Eq. (3.24), we see that as $a \to 0$

$$\frac{m_D}{E_\sigma} = \frac{\sqrt{\sigma}}{g^2} \to 0 \quad .$$

So, we have a system of massless particles. Now, the linearly confining potential only appears on scales $r >> 1/m_D$ and since $m_D/E_\sigma \to 0$, we have no linear potential at any finite physical distance. Therefore, we just have the Coulomb potential. The change in that potential as we change the separation from $\tilde{r}_1 l_\sigma$ to $\tilde{r}_2 l_\sigma$ ($\tilde{r}$ is a dimensionless number) is

$$\frac{\delta V}{E_\sigma} = \frac{g^2 \log(\tilde{r}_2/\tilde{r}_1)}{\pi\sqrt{\sigma}} \to \infty \quad .$$

Thus we can not couple charged particles to the theory in this limit.

3. l_D fixed as $a \to 0$
   In this limit, the physical mass is finite by definition. So we have a theory of massive particles. If we now introduce external charges at separation r, we will have a linear potential as long as $r >> l_D$ and a Coulomb potential for $r << l_D$. The change in the linear potential when we increase the separation from $\tilde{r}_1 l_D$ to $\tilde{r}_2 l_D$ is

$$\frac{\delta V}{E_D} = \frac{\sigma(\tilde{r}_2 l_D - \tilde{r}_1 l_D)}{E_D} = \frac{g^2}{m_D}(\tilde{r}_2 - \tilde{r}_1) \to \infty \quad .$$

   So in this case also we can not couple charged particles to the theory.

4. l_M fixed as $a \to 0$
   In this limit, by definition, our system will contain a non-zero density of monopoles. The corresponding energy scale is $E_M = 1/l_M$ and we can see that

$$\frac{m_D}{E_M} = (g^2 l_D)^{-1/3} \to 0 \quad ,$$

   so in this limit we have massless particles. The change in the linear potential when we increase the separation from $\tilde{r}_1 l_M$ to $\tilde{r}_2 l_M$ is

$$\frac{\delta V}{E_M} = \frac{\sigma(\tilde{r}_2 l_M - \tilde{r}_1 l_M)}{E_M} = \frac{l_M^2}{l_\sigma^2}(\tilde{r}_2 - \tilde{r}_1) \propto (g l_M)^{-1/2} \to \infty \quad .$$

   So, here also, we can not couple charged particles to the theory.

We see that the $U(1)$ LGT in 3D has different dynamical scales whose interplay leads to different physical scenarios at different length scales. The most universally accepted interpretation for the continuum limit is that of a spectrum of free massive scalar particles, with a mass $m_D \sim l_D^{-1}$, i.e. the screened massive photon.

Chapter 4

Monte Carlo Methods

> Monte Carlo is an extremely bad method; it should be used only when all alternative methods are worse.
>
> Alan Sokal [23]

In the previous chapter, we saw that determining physical quantities boils down to computing quantities like

$$\left\langle \cos\theta_{\mu\nu}(r) \right\rangle = \frac{\int \mathcal{D}\theta \ \cos\theta_{\mu\nu}(r) e^{-S[\theta_\mu(x)]}}{\int \mathcal{D}\theta \ e^{-S[\theta_\mu(x)]}} \quad .$$

The integrals above are well-defined and can be performed numerically. However, due to the extremely large number of integrals (one corresponding to each link), computing it using methods like the trapezoidal rule or Simpson's rule is not feasible.

Note that in the pure gauge theories we study, $S[\theta_\mu(x)] \geq 0$. Hence, we can interpret e^{-S}/Z as a probability distribution over the field configurations. This allows us to use importance sampling Monte Carlo integration to estimate the integrals.

This chapter largely follows the discussion in Morningstar's lecture notes on Monte Carlo methods in Quantum Field Theory [24], which has extensive mathematical exposition of Monte Carlo methods.

4.1 Markov Chain Monte Carlo

Consider the integral

$$I = \int_{-\infty}^{\infty} x p(x)\, \mathrm{d}x \quad ,$$

where, $p(x)$ is a probability distribution over x, with mean μ and standard deviation σ. Define

$$S_N := \frac{1}{N} \sum_{i=1}^{N} x_i \tag{4.1}$$

where, $x_1, \ldots, x_N$ are N independent random variables distributed according to $p(x)$. Then, from the *Law of Large Numbers*, we know that as $N \to \infty$, $S_N \to \mu$. More precisely, the *Central Limit Theorem* informs us that for a probability distribution $p(x)$ with finite mean and variance, the random variable S_N is distributed according to a Gaussian with mean μ and standard deviation $\sigma/\sqrt{N}$.

This means that, we can estimate the integral I using N independent random variables drawn from $p(x)$, x_i, as:

$$\begin{aligned} I = \int_{-\infty}^{\infty} x p(x)\, \mathrm{d}x \approx \overline{x} \pm \sqrt{\frac{\overline{x^2} - \overline{x}^2}{N}} \quad , \\ \overline{x} := \frac{1}{N} \sum_{i=1}^{N} x_i, \quad \overline{x^2} := \frac{1}{N} \sum_{i=1}^{N} x_i^2 \quad . \end{aligned} \tag{4.2}$$

From the $\sqrt{N}$ in the denominator of the error, we can see that the estimate can be made more precise by increasing the sample size N.

Applying this to LGT, we can estimate the expectation value of some operator O as

$$\langle O \rangle = \frac{1}{Z} \int \mathcal{D}\theta\, O e^{-S[\theta_\mu(x)]} \approx \frac{1}{N} \sum_{i=1}^{N} O_i \quad , \tag{4.3}$$

where, N is the number of independent field configurations distributed according to e^{-S}/Z, and O_i is the operator O computed using the ith configuration. The error in this estimate is given by

$$\sqrt{\frac{\langle O^2 \rangle - \langle O \rangle^2}{N}} \quad , \tag{4.4}$$

where $\langle O^2 \rangle$ is in turn estimated as

$$\langle O^2 \rangle \approx \frac{1}{N} \sum_{i=1}^{N} O_i^2 \quad . \tag{4.5}$$

The key challenge now is to generate configurations of the field $\theta_\mu(x)$ which is distributed according to e^{-S}/Z. This is done using *Markov Chains*

4.1.1 Markov Chains

This section follows the discussion in Morningstar [24] and in the textbook by James Sethna [25, Ch. 8].

A *Markov Chain* is a stochastic process which generates a sequence of configurations with a probability which only depends on the *current* state.

Consider a system with R states $s_1, \ldots, s_R$. Let the *transition probability* to go from state s_i to s_j be p_{ji}. We define the *transition matrix* to be an $R \times R$ real matrix $\mathbf{P}$ whose elements are the transition probabilities p_{ij}. Suppose the initial probability for being in a state s_i is $w_i^{(0)}$. Then, the probability for being in the state s_i after one time-step of the Markov chain is given by

$$w_i^{(1)} = \sum_{i=1}^{R} p_{ij} w_j^{(0)} \quad . \tag{4.6}$$

If we construct a vector $\vec{w}$ using the probabilities w_i, the distribution after a time-step is given by

$$\vec{w}^{(1)} = \mathbf{P}\vec{w}^{(0)} \quad . \tag{4.7}$$

Thus, the distribution of the states after n time-steps is given by

$$\vec{w}^{(n)} = \mathbf{P}^n \vec{w}^{(0)} \quad . \tag{4.8}$$

We are interested in the probability of finding different states at $n \to \infty$. This will be given by the asymptotic behaviour of $\mathbf{P}^n$ at large n. We define the probability vector $\vec{w}$ to be *stationary* or *invariant* under the Markov chain if

$$\vec{w} = \mathbf{P}\vec{w} \quad . \tag{4.9}$$

If our system has reached such a distribution, it is said to have reached *equilibrium*. Although we are interested in the case where the Markov chain equilibrates to a unique stationary distribution; in general, a Markov chain can have multiple stationary distributions. We would like to know under what circumstances, the Markov chain defined by **P** equilibrates to a unique stationary state.

In order to do this, let's define some terms. A state is termed as *transient* if the system eventually leaves that state, never to return. A state is *positive recurrent*, if the system returns to it in a finite time. The Markov chain can also have *cycles*, where the system shifts through a finite number of distinct classes of states before returning to the original one. All of these are obstacles for going to a unique stationary distribution. We will remove such possibilities by considering *ergodic* Markov chains. A finite-state Markov chain is ergodic if it does not have cycles and it is *irreducible*: that is, one can get from every state s_i to every other state s_j in a finite sequence of moves. We demand ergodicity because we would like to sample all possible field configurations.

The following general fact about Markov chains can be proved[24]:
An irreducible Markov chain without cycles, has a stationary distribution $\vec{w}$ if, and only if, all its states are positive recurrent, and this stationary distribution is unique and identical to the limiting distribution $w_i = \lim_{n\to\infty} p_{ij}^n$ independent of the initial state s_j.

We will concern ourselves with the more specific class of Markov chains that satisfy *detailed balance*. A Markov chain satisfies detailed balance if there is some probability distribution $\vec{w}$ satisfying

$$p_{ij} w_j = p_{ji} w_i \quad . \tag{4.10}$$

This means that the system makes the transitions $s_i \mapsto s_j$ and $s_j \mapsto s_i$ with equal rates. One can see that the probability distribution $\vec{w}$ would be stationary. The following fact is central to our use of Markov chains:
A Markov chain with a finite number of states can be guaranteed to converge to an equilibrium distribution if it is ergodic and satisfies detailed balance.

Thus, we can use Markov chains to generate field configurations which are distributed according to the stationary distribution e^{-S}/Z. In practice, we begin with some arbitrary field configuration and perform Markov chain updates to reach equilibrium. Note that the configurations thus generated

are correlated. This correlation in some operator O is quantified using the *autocorrelation* $A_O(t)$

$$A_O(t) = \frac{\langle O_i O_{i+t} \rangle - \langle O_i \rangle^2}{\langle O_i^2 \rangle - \langle O_i \rangle^2} \quad . \tag{4.11}$$

In practice, if we have N configurations from the Markov chain, we estimate $\langle O_i \rangle$ and $\langle O_i O_{i+t} \rangle$ by

$$\begin{aligned} \langle O_i \rangle &= \frac{1}{N} \sum_{k=1}^{N} O_k \quad , \\ \langle O_i O_{i+t} \rangle &= \frac{1}{N-t} \sum_{k=1}^{N-t} O_k O_{k+t} \quad . \end{aligned} \tag{4.12}$$

The asymptotic decay of the autocorrelation is exponential, $A_O(t) \sim e^{-t/\tau_O}$, which can be used to the define the autocorrelation time τ_O. Normally one instead uses the integrated autocorrelation time, which also contains contributions from the often dominant non-asymptotic behavior;

$$\tau_O^{\text{int}} = \frac{1}{2} + \sum_{t=1}^{\infty} A_O(t) \quad . \tag{4.13}$$

In practice,

$$\sum_{t=1}^{\infty} A_O(t) \approx \sum_{t=1}^{N/2} A_O(t) \quad .$$

We determine that the system has reached equilibrium by observing whether some observable O_i reaches a stable value. We begin collecting samples only after the system equilibrates. In order to ensure that the field configurations are statistically independent, the simulation data is subdivided into a number of bins, each containing some M number of configurations. M is chosen to be much larger than τ_O. Then, the average over each bin can be considered as a sufficiently uncorrelated data set. One can then use Eqs. (4.3) and (4.4) to estimate the integrals and the associated error.

4.1.2 Metropolis-Hastings Method

In order to use Markov chains, we need to construct the appropriate transition probabilities p_{ij} satisfying detailed-balance, which would equilibrate to the probability distribution

$$\pi[\theta_\mu(x)] = \frac{e^{-S[\theta_\mu(x)]}}{\int \mathcal{D}\theta \, e^{-S[\theta_\mu(x)]}} \quad .$$

The *Metropolis-Hastings* method provides a simple and general way to construct the transition probabilities. It has the advantage that we only need to compute local quantities and the partition function never enters into the calculation.

We use an *auxiliary proposal density* $R(\theta_\mu \mapsto \tilde{\theta}_\mu)$ which

- must be normalized,
- can be evaluated for all field configurations,
- can be easily sampled,
- and needs no relationship to the equilibrium probability distribution $\pi[\theta_\mu(x)]$.

Given such a proposal density, this method performs updates as follows:

1. Use $R(\theta_\mu \mapsto \tilde{\theta}_\mu)$ to propose a new configuration $\tilde{\theta}_\mu(x)$ from the current configuration $\theta_\mu(x)$.
2. Accept the new configuration with probability

$$P_{acc}(\theta_\mu \mapsto \tilde{\theta}_\mu) = \min\left(1, \frac{\pi[\tilde{\theta}_\mu]R(\tilde{\theta}_\mu \mapsto \theta_\mu)}{\pi[\theta_\mu]R(\theta_\mu \mapsto \tilde{\theta}_\mu)}\right) \quad .$$

3. If rejected, the original configuration $\theta_\mu(x)$ is retained.

It can be shown that such an update rule will satisfy detailed balance.

The simulations of the $U(1)$ LGT were performed using the Metropolis algorithm and the overrelaxation algorithm which belong to this class.

4.2 The Algorithms

In this project, we have used the Metropolis and overrelaxation algorithms to simulate the $U(1)$ LGT in terms of the link-variables. For the dual model, we were able to extract good quality data using only the Metropolis algorithm.

4.2.1 The Metropolis Algorithm

The Metropolis [26] algorithm is one of the oldest and simplest algorithms which sees widespread use. The procedure for the link-variable simulation is as follows:

1. For a given link $(x + \hat{\mu})$, propose an update for $\theta_\mu(x)$ as

$$\theta_\mu(x) \mapsto \tilde{\theta}_\mu(x) = \theta_\mu(x) + \delta\theta \quad ,$$

   where $\delta\theta$ chosen with uniform probability from the interval $[-\Delta, \Delta]$.

2. Calculate the change in the action δS due to the proposed update. This will only depend on the other link-variables which make up the plaquettes that $(x + a\hat{\mu})$ is a part of. This is illustrated in Fig. 4.1.

3. Accept the proposed link value $\tilde{\theta}_\mu(x)$ with probability min $\left(1, e^{-\delta S}\right)$.

4. Repeat this procedure for each link.

Performing this update for all links constitutes one *Metropolis sweep*. As a rule of thumb, we choose a value for Δ which ensures that the acceptance rate for the proposed configuration is around $50\% - 70\%$. If the acceptance rate is too small, then we waste a lot of resources to generate field configurations which won't be accepted. On the other hand, if the acceptance rate is too big, it means that the new configurations are always similar to the original configuration, and we won't explore the full configuration space efficiently.

This is a simple and robust update procedure, which is both ergodic and satisfies detailed balance. But it has two issues: (a) as we approach a critical point, the autocorrelation time diverges, (b) we could get stuck in a local minima. We encounter an increase in autocorrelations as we tune to large β.

A way out is to find an update which can make large changes in the field configurations, while ensuring that δS is negligible. The overrelaxation algorithm, which does this, solves both of the above issues.

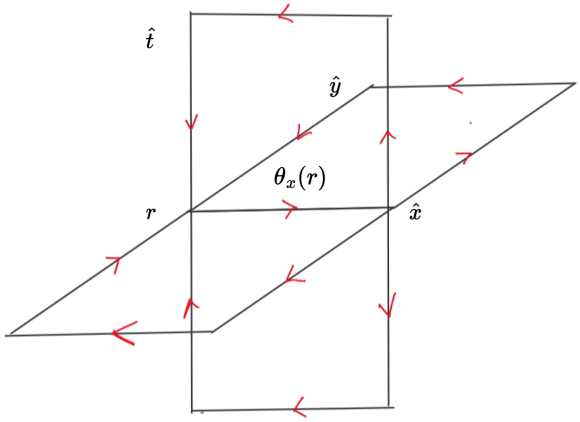

Figure 4.1: The figures shows the different plaquettes which get a contribution from the link variable $\theta_x(r)$. The sum of the remaining terms in the plaquette apart from $\theta_x(r)$ is called a 'staple'.

4.2.2 Overrelaxation Algorithm

The overrelaxation (OR) update [27] makes large changes to the field configurations with a negligible change in the action. Thus, we try to perform *action preserving* $\delta S = 0$ updates to the field at a site. This allows us to make large local changes to the field value. Because this update makes small changes to the action, we should use OR update in tandem with an action changing update such as the Metropolis.

We are studying the $U(1)$ LGT whose action is given by

$$S = -\sum_p \left(\beta \cos\theta_p + \gamma \cos\theta_p\right) \quad .$$

We first discuss OR update for $\gamma = 0$. The contribution to the action due to a given link (e.g. $\theta_x(r)$) is of the form

$$\begin{aligned} S(\theta_x(r)) &= -\beta \sum_s \mathrm{Re}(e^{i(\theta_x(r)+\theta_s)}) \\ &= -\beta\, \mathrm{Re}(e^{i\theta_x(r)} \sum_s e^{i\theta_s}) \\ &= -\beta\, \mathrm{Re}(re^{i\varphi}) \quad . \end{aligned} \tag{4.14}$$

where θ_s is the oriented sum of the link variables over each 'staple' as shown in the Fig. 4.1. The sum is over the four staples connected to the given link. In going from line 2 to 3, we have defined $re^{i\varphi} := e^{i\theta_x(r)} \sum_s e^{i\theta_s}$. Note that the only non-trivial update which keeps the action unchanged is the one which takes $\varphi \mapsto -\varphi$. Hence, the link variable is updated as

$$\theta_x(r) \mapsto \theta_x(r) - 2\varphi \quad . \tag{4.15}$$

The OR update for the case of $\beta = 0$ is analogous and also has $\delta S = 0$. When both $\beta \neq 0$ and $\gamma \neq 0$, we need to decide which of the two terms in the action to keep fixed. We choose the update which leads to the smallest change in the action. Since we work in the regime where γ is small, we use the update which keeps the β-term unchanged.

The update procedure is as follows:

1. For a given link $(x + a\hat{\mu})$, propose an update according to (4.15)
2. Accept the proposed link value with probability $\min\left(1, e^{-\delta S}\right)$.
3. Repeat this process for each link

Performing this procedure on all the links constitutes one *OR sweep*. Note that while this update satisfies detailed balance, it won't be ergodic when $\delta S = 0$.

Chapter 5

$U(1)$ LGT with an Extended Action

In this chapter, we will introduce the extended action for the $U(1)$ LGT in 3D. We will also discuss Monte Carlo simulations of this model on a 3D cubic lattice in terms of the link-variables.

5.1 The Extended Action

Recall from chapter 1 that the general action of a pure gauge theory can have a sum over its various irreducible representations. For $U(1)$, the representations are of the form $e^{in\theta}$, with integer $n \in \mathbb{Z}$. In our study, we consider the action containing an 'adjoint' term corresponding to $n = 2$ along with the usual Wilson term. Thus, our action is

$$S = -\sum_p \left(\beta \cos\theta_p + \gamma \cos 2\theta_p\right) \quad , \tag{5.1}$$

where the sum is over all plaquettes of the cubic lattice. The plaquette operator $\theta_p = \theta_{\mu\nu}(x)$ is defined as before. If we take the naive continuum limit, $a \to 0$, we get the usual continuum action

$$S = \int \mathrm{d}^3x \, \frac{1}{4g^2} F_{\mu\nu}^2$$

with

$$\beta + 4\gamma \to \frac{1}{ag^2}, \quad \text{as} \quad a \to 0 \quad . \tag{5.2}$$

The γ-term provides us with an extra parameter to tune the behaviour of the system. We are

interested in studying how physical quantities like masses and the string tension behave for different values of γ.

For the standard Wilson action, the continuum limit is taken by tuning to larger values of β. As we will see, even small values of γ allow us to probe the continuum behaviour of the system at relatively small β. We will quantify this improvement by computing an effective $\beta*$ corresponding to a given value of β and γ. This will be done using the known scaling behaviour of the mass gap and the string tension.

The $U(1)$ LGT with this extended action has been studied previously in 4D [28][29][30], where its phase structure in the β-γ plane was determined.

5.2 Numerical Simulations

We performed Monte Carlo simulations of the model on a cubic lattice of size $L_s^2 \times L_t$ with $L_s = 16$ and $L_t = 16, 24$. We enforced periodic boundary conditions (PBC). Each Monte Carlo sweep consisted of 1 Metropolis sweep and 2 overrelaxation sweeps. The numerical simulation was coded in Julia language. For computing the mass and the string tension, we ran the simulation for 10^7 sweeps after running it for 5000 sweeps to ensure that it has thermalized. We stored the data after averaging it over every 100 sweeps. The plaquette data is from a simulation with 10^4 sweeps.

We used the mean plaquette, P, to test our simulation. P is the mean of $\cos\theta_p$ over all plaquettes of the lattice,

$$P := \frac{1}{N_p} \sum_p \cos\theta_p \quad , \tag{5.3}$$

where, $N_p = 3L_s^2 L_t$ is the total number of plaquettes in the lattice.

It was noticed that as we increase β, the system became stiffer and the fluctuations in the plaquette decreased. In order to keep the acceptance rate acceptable, we decreased the Δ for our Metropolis updates. Increase in β also increased the autocorrelation and the number of sweeps required to thermalize. However, the use of overrelaxation algorithm helped in reducing the autocorrelations as can be seen from Fig. 5.1. We see that the mean plaquette reaches the equilibrium value quicker and the autocorrelation in mean plaquette also reduces.

The plaquette values computed at $\gamma = 0$ showed agreement with the values present in Loan, et. al.[8]. We also compared our data with strong-coupling[31] and weak-coupling[32] expansion

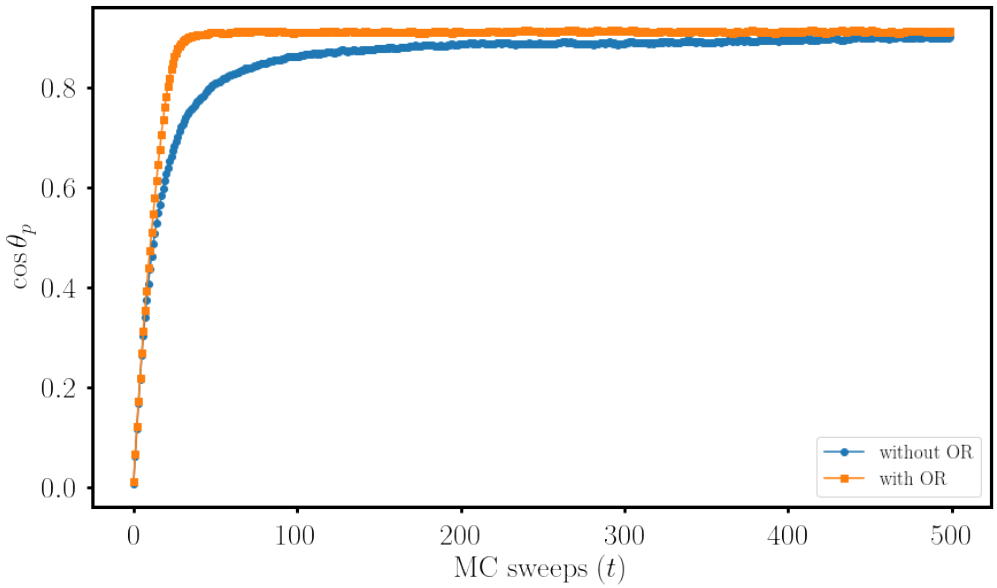

(a)

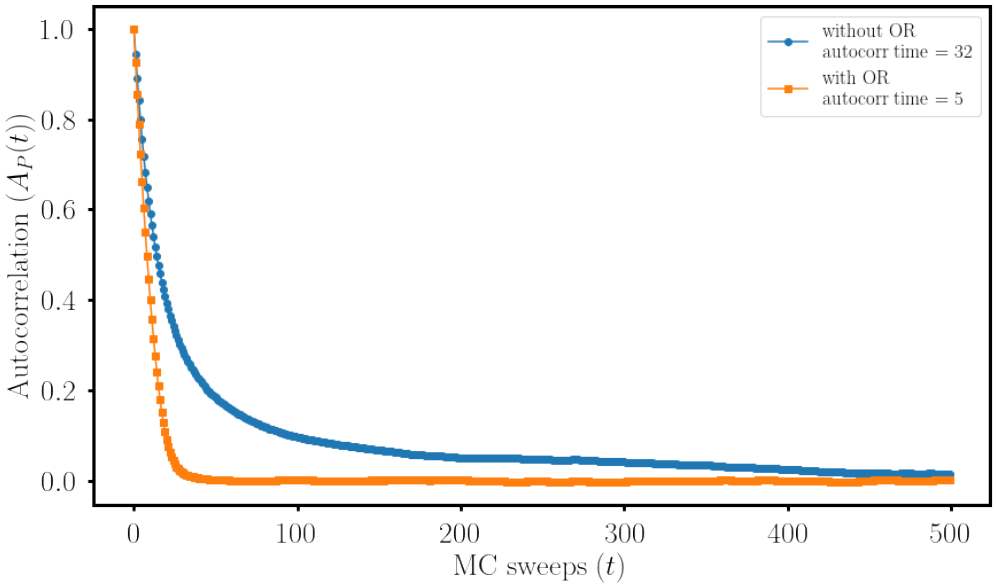

(b)

Figure 5.1: Using overrelaxation with Metropolis leads to faster thermalization. This can be seen from (a) the mean plaquette at different sweeps, and (b) the autocorrelation in the mean plaquette at $\beta = 4.0, \gamma = 0$

calculations. Fig. 5.2 shows the plot of mean plaquette data against β along with the predictions from strong-coupling expansion truncated at β^7 and weak-coupling expansion truncated at β^{-4}.

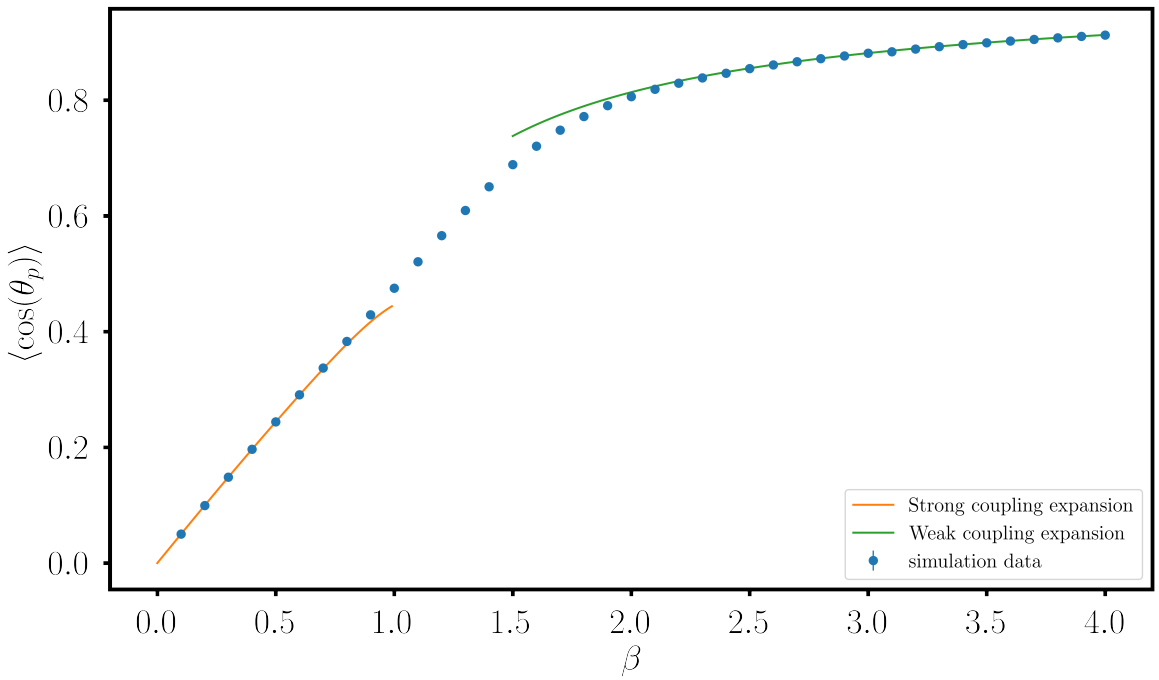

Figure 5.2: The mean plaquette computed from simulation agrees with strong and weak coupling expansions

5.2.1 Effect of γ on Mean Plaquette

We computed the mean plaquette for $0.1 \leq \beta \leq 4.0$ at increments of 0.1, and for $\gamma = 0.0, 0.1, 1.0$. This data has been presented in Fig. 5.3. We can see that as we increase γ, the plaquette asymptotes to the continuum limit faster.

5.2.2 Mass and String Tension

We are interested in studying the effect of γ on masses and string tension.

We study the mass of the lowest glueball state, i.e. the $J^{PC} = 0^{--}$ antisymmetric state. This mass is computed by measuring the correlations of the glueball operator $P_-(t)$ defined as

$$P_-(t) := \frac{1}{L_s^2} \sum_{\vec{r}} \sin \theta_{xy}(\vec{r}, t) \quad , \tag{5.4}$$

where the time-slice average is used to ensure that we create glueballs with 0 momentum. We measure the average of the product $P_-(i)P_-(i+\tau)$ over all time-slices i and $\tau = 0, \ldots, L_t/2$. A jackknife analysis was used to compute the expectation value and the errors. We extract the mass m

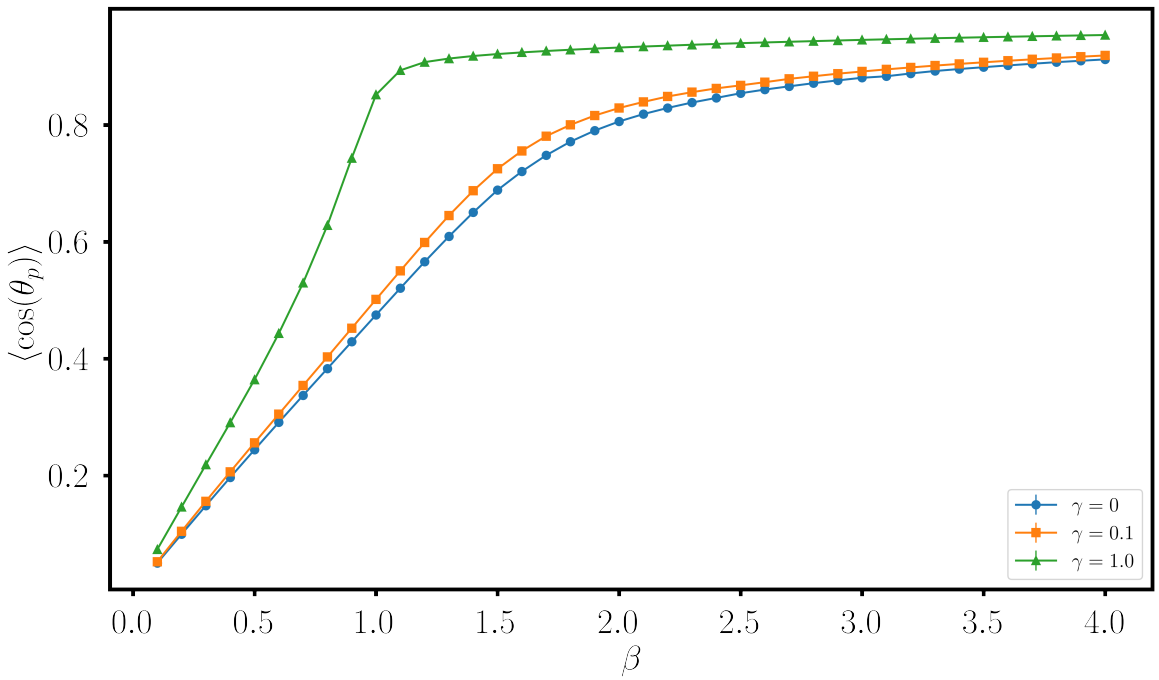

Figure 5.3: The mean plaquette as a function of β at different γ for a 16^3 cubic lattice.

by fitting the correlation function to

$$P_-(0)P_-(\tau) = c\left[e^{-m\tau} + e^{-m(L_t-\tau)}\right] \quad . \tag{5.5}$$

We performed a non-linear least-squares fit. To extract high-precision masses, it is necessary to use a variational approach which uses a linear combination of operators to estimate the 'exact' state.

We compute the string tension by measuring rectangular Wilson Loops $W(r,\tau)$ of size $r \times \tau$ oriented along the time-like direction. This was done for $r = 1, 2, 3, 4$. The potential can be extracted by recalling that in the limit $\tau \to \infty$,

$$\langle W(r,\tau) \rangle \sim e^{-V(r)\tau} \quad . \tag{5.6}$$

Since the system is in the confining phase, the Wilson loops obey the area law, i.e. the magnitude of $W(r,\tau)$ falls as $e^{-r\tau}$. However, the noise is independent of the size of the loop. Thus, we encounter bad signal-to-noise ratio for large loops. This is troubling because Eq. (5.6) is only valid for large loops. For small τ, we will have contributions from excited state which lead to errors in extracting $V(r)$.

Smearing Procedure

We use a simple *smearing* technique [8] on the space-like link variables. This allows us to suppress excited state contributions by constructing Wilson loops and glueball operators which have a large overlap with the lowest state. The Wilson Loops are constructed using space-like links which have been iteratively smeared out. In a single iteration, we replace every space-like link variable, $U_k = \exp(i\theta_k(x))$ by

$$U_k \mapsto P\left[\alpha U_k + \frac{(1-\alpha)}{2}\sum_s U_s\right] \quad , \tag{5.7}$$

where the sum is over the links in the two staples on either side of the spatial link, and P denotes a projection onto $U(1)$, by normalizing the complex number to unit magnitude. Following Loan, et. al., we use a smearing parameter $\alpha = 0.7$. We collected data for 0, 10 and 20 levels of smearing.

Mass Results

We simulated the system on a $16^2 \times 24$ cubic lattice at $\beta = 1.0, 2.0$ and $\gamma = 0.0$, with the products $P_-(0)P_-(\tau)$ computed at different smearing levels.

The data at $\beta = 1.0$ was of poor quality and the mass extracted from there didn't agree with the results in Loan, et. al. Our observations from simulations of the height model suggests that this might be because the mass is too large and we need a finer grid to correctly measure it.

We could extract good quality data at $\beta = 2.0$. It was observed that the correlation for 10 and 20 levels of smearing overlapped. The correlations without smearing displayed a different behaviour. We found that the masses for all three smearing levels agreed within errors. In lattice units, the mass of the antisymmetric state was computed to be

$$m_{--} = 0.437(1) \quad . \tag{5.8}$$

This agrees with the results in Loan, et. al. The correlation functions and the fitted curve are shown in Fig. 5.4.

Inter-charge Potential

We simulated the system on a $16^2 \times 24$ cubic lattice at $\beta = 1.0, 2.0$ and $\gamma = 0.0$, and measured the Wilson loops $W(r, \tau)$ at 0, 10 and 20 smearing levels. This was done for $r = 1, 2, 3, 4$ and $\tau = 1, \ldots, 11$. Similar to mass, we couldn't extract the potential satisfactorily for $\beta = 1.0$. The

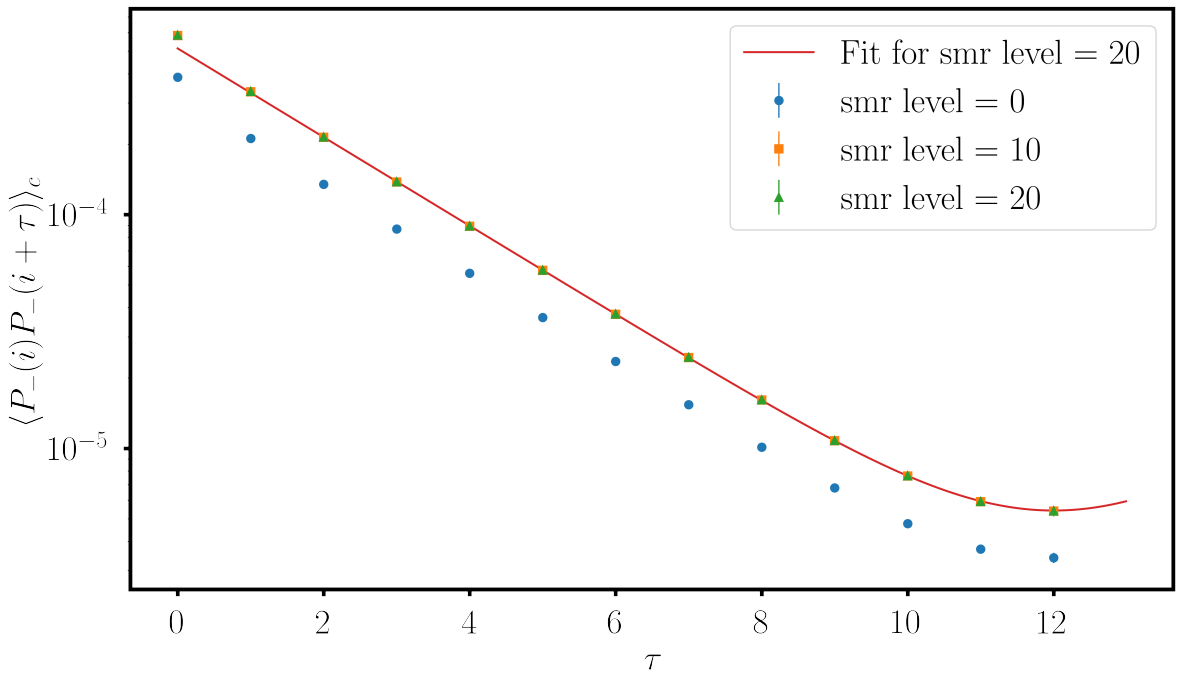

Figure 5.4: The connected correlation function for $P_-(t) = \sin\theta_p(t)$ between different time-slices. Data for different smearing levels.

analysis at $\beta = 2.0$ yielded a value of string tension which is of the same order of magnitude as the value given in Loan, et. al. However, we couldn't match the value provided there.

Using the data from the simulations, we estimated

$$\left\langle \log \frac{W(r,\tau)}{W(r,\tau+1)} \right\rangle$$

by performing a jackknife analysis. Due to the asymptotic behaviour of $W(r,\tau)$ as given in Eq. (5.6), this should asymptote to $V(r)$ at large τ. Fig. 5.5 shows this behaviour. Note that smearing allows us to reach the asymptotic limit faster. By fitting the value at large r to a horizontal, we extracted the $V(r)$ for different r. We did this for data from 10, 20 levels of smearing. Fig. 5.6 displays the plot of $V(r)$ against r. We fitted the inter-charge potential to the form

$$V(r) = a + \sigma r + b \log r \tag{5.9}$$

where, σ is the string tension and the logarithm is the Coulomb potential in 3D. We found that

$$\sigma = 0.037(1) \tag{5.10}$$

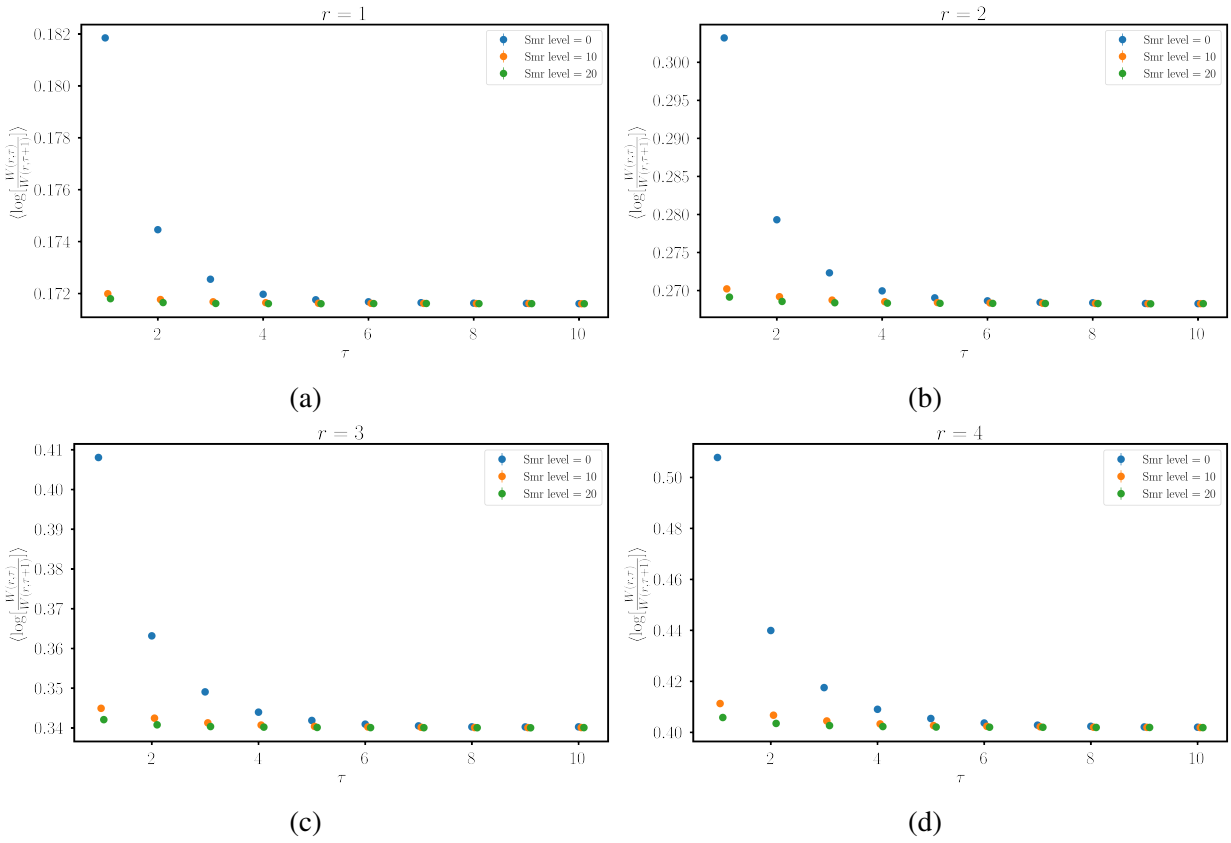

Figure 5.5: Plots of $\langle \log(W(r,\tau)/W(r,\tau+1)) \rangle$ at different τ to extract $V(r)$. The behaviour at different smearing levels can be seen. Data for a $16^2 \times 24$ cubic lattice.

which disagrees with Loan, et. al.'s value of $\sigma = 0.050$.

We note that simulating the system directly requires long runs and use of techniques like smearing in order to extract high-quality data. The data presented in this chapter were from simulations which were performed for exploratory and pedagogical reasons. In the next chapter, we will discuss an exact dual mapping to an integer 'height' model. Simulation of this dual model is much more efficient and allows us to study the system on much larger lattice. The main results of this thesis are from the simulation of the dual model.

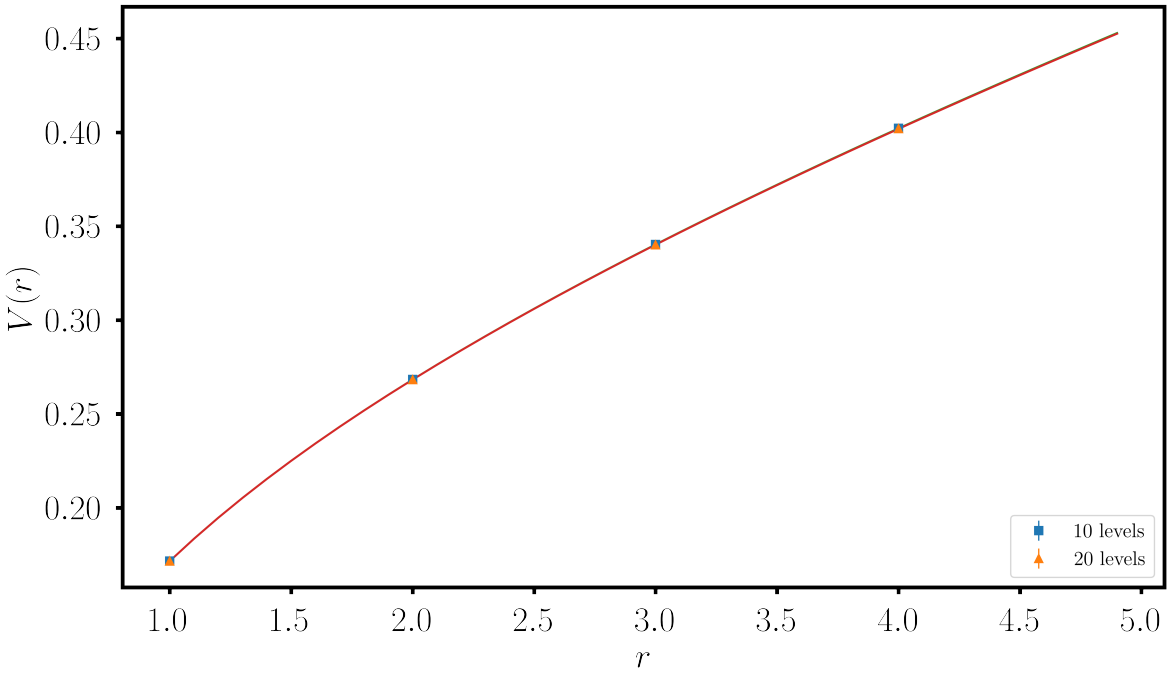

Figure 5.6: Plot of the inter-charge potential $V(r)$ against the inter-charge seperation r. Data for 10, 20 levels of smearing on a $16^2 \times 24$ lattice.

Chapter 6

The Duality Mapping

In this chapter, we will map the U(1) LGT with extended action to an integer-valued 'height' model. We follow the general approach outlined in Nguyen, Tanizaki, Unsal [33]. This computation holds for both the cubic and the triangular lattices.

It is well-known that the $U(1)$ LGT can be mapped to an integer height model using a Kramers-Wannier type duality [5, 34, 6]. In fact, the rigorous proof for confinement in 3D $U(1)$ LGT by Gopfert and Mack [6] uses the duality mapping of the Villain action to the *height model*. While these mappings begin from the Villain action, we will use the full extended action to rewrite the partition function in terms of generalized modified Bessel functions $I_k^{\gamma}(\beta)$. Note that this is an exact, non-perturbative duality and not a configuration-to-configuration mapping.

The dual model offers us practical advantages for numerical simulations. The variables of this model are integers, which makes them easier to implement. Moreover, for a 3D cubic lattice with N sites, we only need to consider N heights instead of $3N$ links. This leads to much faster run times. Another major advantage is in the computation of the inter-charge potential. In order to measure this in the link-variable formulation, we would need to measure large Wilson loops or Polyakov loop correlators, both of which suffer from a bad signal-to-noise ratio. On the other hand, the dual model allows us to directly insert charges into the system and measure the energy change. Due to these advantages, there have been several studies which have used this duality mapping. Some examples of studies with the height model dual to the Villain approximation are [35], [36]. An example of a study which uses the mapping to the modified Bessel function is [37].

To perform the calculations concisely, we will use the lattice differential forms formalism introduced in appendix A. We use s, ℓ, p, c to label the sites, links, plaquettes and cubes (or prisms) of the lattice, respectively, and $\tilde{s}, \tilde{\ell}, \tilde{p}, \tilde{c}$ to denote these structures on the corresponding dual lattice. We will use the lattice differential forms convention to rewrite the link and plaquette terms as $\theta_\mu(x) = \theta_\ell$ and $\theta_{\mu\nu}(x) = f_p$.

6.1 Dualisation of the Action

As seen in the previous chapter, the extended action for the U(1) LGT is given by

$$S = -\sum_p \left(\beta \cos f_p + \gamma \cos 2f_p\right) \quad , \tag{6.1}$$

where, $f_p = (\mathrm{d}\theta)_p$ is the plaquette operator which we usually denote as $\theta_p = \theta_{\mu\nu}(x)$, and the sum is over all plaquettes of the lattice. The partition function is

$$Z = \int \mathcal{D}\theta \prod_p \exp\big(\beta \cos\big(f_p\big) + \gamma \cos\big(2f_p\big)\big) \quad , \tag{6.2}$$

where the integration is over the link variables

$$\int \mathcal{D}\theta \; := \prod_\ell \int_{-\pi}^{\pi} \frac{\mathrm{d}\theta_\ell}{2\pi} \quad .$$

We can expand $\exp\big(\beta \cos\big(f_p\big) + \gamma \cos\big(2f_p\big)\big)$ in a Fourier series as

$$e^{\beta \cos\left(f_p\right) + \gamma \cos\left(2f_p\right)} = \sum_{k_p \in \mathbb{Z}} e^{i k_p f_p} I^\gamma_{k_p}(\beta) \quad , \tag{6.3}$$

where the coefficients $I^\gamma_{k_p}(\beta)$, known as *generalized modified Bessel functions*, are given by

$$\boxed{I^\gamma_k(\beta) := \frac{1}{2\pi} \int_{-\pi}^{\pi} \mathrm{d}x \, e^{\beta \cos(x) + \gamma \cos(2x)} \cos(kx)} \quad . \tag{6.4}$$

For $\gamma = 0$, these correspond to the usual modified Bessel functions $I_k(\beta)$.

Substituting the expansion (6.3) in the partition function (6.2), we get

$$Z = \int \mathcal{D}\theta \sum_{\{k_p \in \mathbb{Z}\}} e^{i(k,f)} \prod_p I^{\gamma}_{k_p}(\beta) \quad , \tag{6.5}$$

where the sum is over all possible integer values for k_p on each plaquette. Since $f_p = \mathrm{d}\theta_p$, we can perform integration by parts

$$(k, \mathrm{d}\theta) = (\mathrm{d}^\dagger k, \theta) \quad ,$$

to rewrite the partition function as

$$Z = \int \mathcal{D}\theta \sum_{\{k_p \in \mathbb{Z}\}} e^{i \sum_\ell (\mathrm{d}^\dagger k)_\ell \theta_\ell} \prod_p I^{\gamma}_{k_p}(\beta) \quad . \tag{6.6}$$

Performing the integrals over θ_ℓ using

$$\int_{-\pi}^{\pi} \frac{\mathrm{d}\theta}{2\pi} e^{i(\mathrm{d}^\dagger k)_\ell \theta_\ell} = \delta_{(\mathrm{d}^\dagger k)_\ell, 0} \quad ,$$

we can write the partition function as a constrained sum over $\{k_p\}$.

$$Z = \sum_{\{k_p \in \mathbb{Z}\}} \left\{ \prod_\ell \delta_{(\mathrm{d}^\dagger k)_\ell, 0} \right\} \left\{ \prod_p I^{\gamma}_{k_p}(\beta) \right\} \tag{6.7}$$

The constraint $\mathrm{d}^\dagger k = 0$ is enforced on every link of the lattice. We can use Eq. (A.11) to write k_p as

$$(*k)_{\tilde{\ell}} = (\mathrm{d}h)_{\tilde{\ell}} + (\mathrm{d}^\dagger m)_{\tilde{\ell}} + a_{\tilde{\ell}} \quad , \tag{6.8}$$

where $h_{\tilde{s}}$, $m_{\tilde{p}}$ and $a_{\tilde{\ell}}$ are integer-valued forms on the dual lattice. By setting $m_{\tilde{p}} = 0$, we can impose $\mathrm{d}^\dagger k = 0$ and convert the constrained sum over k_p to an unconstrained sum over $h_{\tilde{s}}$ and $a_{\tilde{\ell}}$.

Now, $a_{\tilde{\ell}}$ is an harmonic form satisfying $\mathrm{d}a = \mathrm{d}^\dagger a = 0$. This implies that the configurations with non-trivial $a_{\tilde{\ell}}$ look like 'domain walls' and the action of such configurations scale as L^2. Therefore, such configurations will be highly suppressed. Hence, we will set $a_{\tilde{\ell}} = 0$ for our simulations.

The decomposition (6.8) allows us to make the replacement $k_p \mapsto (*\,\mathrm{d}h)_p$ in (6.7) to get the

partition function of the dual model:

$$\boxed{Z = \sum_{\{h_{\tilde{s}} \in \mathbb{Z}\}} \prod_{\tilde{\ell}} I^{\gamma}_{(\mathrm{d}h)_{\tilde{\ell}}}(\beta)} \quad . \tag{6.9}$$

The weight for any given configuration of heights $\{h_{\tilde{s}}\}$ is given by $Z^{-1} \prod_{\tilde{\ell}} I^{\gamma}_{(\mathrm{d}h)_{\tilde{\ell}}}(\beta)$.

For $\gamma = 0$, in the limit $\beta \to \infty$, we can use the asymptotic limit of modified Bessel function

$$I_k(\beta) \sim \frac{e^{\beta}}{\sqrt{2\pi\beta}} e^{-\frac{1}{2\beta}k^2}$$

to rewrite the partition function (6.9) as

$$Z = \sum_{\{h_{\tilde{s}} \in \mathbb{Z}\}} \prod_{\tilde{\ell}} \frac{1}{\sqrt{2\pi\beta}} e^{-\frac{1}{2\beta}(\mathrm{d}h_{\tilde{\ell}})^2} \tag{6.10}$$

up to an overall normalization. This gives us the *height model* on the dual lattice whose action is given by

$$S = \frac{1}{2\beta} \sum_{\langle xy \rangle} \left(h_x - h_y\right)^2 \quad , \tag{6.11}$$

where the sum is over all nearest-neighbours.

Note that the dual model is defined on the *dual lattice*. The dual of a 3D cubic lattice with N sites is a 3D cubic lattice with N sites, and the dual of a 3D triangular lattice with N sites is a 3D *honeycomb* lattice with $2N$ sites.

6.2 Dualisation of Wilson Loops

We would like to understand what the observables look like in the dual model. Let's consider a Wilson Loop $W(C)$ which is given by the product of $e^{i\theta_\ell}$ along a closed loop C.

$$W(C) := \exp\left(i \sum_{\ell \in C} \theta_\ell\right) = \exp\left(i \sum_{\ell} \theta_\ell \zeta_\ell\right) \quad , \tag{6.12}$$

where we have introduced a 1-form ζ_ℓ which equals 1 for (directed) links $\ell \in C$, and is 0 otherwise. Note that the divergence of ζ_ℓ is 0, i.e. $\mathrm{d}^\dagger \zeta = 0$ at each site s. So we can decompose $(*\zeta)_{\tilde{p}}$ as

$$(*\zeta)_{\tilde{p}} = (\mathrm{d}\omega)_{\tilde{p}} \tag{6.13}$$

or alternatively,

$$\zeta_\ell = (\mathrm{d}^\dagger * \omega)_\ell \quad . \tag{6.14}$$

We need to choose a 2-form $(*\omega)_p$ such that

$$\begin{aligned} (\mathrm{d}^\dagger * \omega)_\ell &= 1 \quad \text{if} \quad \ell \in C, \\ &= 0 \quad \text{otherwise.} \end{aligned} \tag{6.15}$$

One choice is to keep $(*\omega)_p = 1$ for $p \in S$, where S is a surface bounded by C, and $(*\omega)_p = 0$ for other plaquettes. For convenience, we can choose S to be the minimal surface bounded by C. On the dual lattice, this corresponds to $\omega_{\tilde{\ell}} = 1$ for those links $\tilde{\ell}$ which pierce the surface S. Fig. 6.1 shows these links piercing through S.

We can do a similar computation to the one leading to Eq. (6.6) to find that the expectation value of the Wilson Loop is given by

$$\langle W(C) \rangle = \frac{1}{Z} \int \mathcal{D}\theta \sum_{\{k_p \in \mathbb{Z}\}} e^{i \sum_\ell \mathrm{d}^\dagger (k + *\omega)_\ell \theta_\ell} \prod_p I^\gamma_{k_p}(\beta) \quad .$$

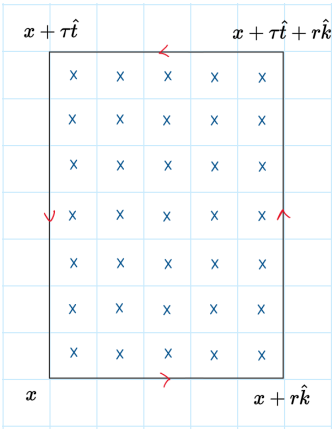

Figure 6.1: Dual links piercing the minimal surface bounded by a rectangular Wilson loop.

Performing the integral over θ_ℓ, we get a constrained sum over $\{k_p \in \mathbb{Z}\}$

$$\langle W(C)\rangle = \frac{1}{Z}\sum_{\{k_p\in\mathbb{Z}\}}\left\{\prod_\ell \delta_{(\mathrm{d}^\dagger(k+*\omega))_\ell,0}\right\}\left\{\prod_p I^\gamma_{k_p}(\beta)\right\} \quad . \tag{6.16}$$

To turn this into an unconstrained sum, we write

$$(*k)_{\tilde\ell} = (\mathrm{d}h)_{\tilde\ell} - \omega_{\tilde\ell} \quad . \tag{6.17}$$

Hence, $\langle W(C)\rangle$ is given by an unconstrained sum over $\{h_{\tilde s} \in \mathbb{Z}\}$

$$\langle W(C)\rangle = \frac{1}{Z}\sum_{\{h_{\tilde s}\in\mathbb{Z}\}}\prod_{\tilde\ell} I^\gamma_{(\mathrm{d}h)_{\tilde\ell}-\omega_{\tilde\ell}}(\beta) \quad .$$

Moreover, we can use the $h_{\tilde s} \mapsto -h_{\tilde s}$ symmetry to rewrite

$$\langle W(C)\rangle = \frac{1}{Z}\sum_{\{h_{\tilde s}\in\mathbb{Z}\}}\prod_{\tilde\ell} I^\gamma_{(\mathrm{d}h)_{\tilde\ell}+\omega_{\tilde\ell}}(\beta) \quad . \tag{6.18}$$

Let's consider the summand. Using our definition of $\omega_{\tilde\ell}$, we can rewrite it as

$$\begin{aligned}\prod_{\tilde\ell} I^\gamma_{(\mathrm{d}h)_{\tilde\ell}+\omega_{\tilde\ell}}(\beta) &= \left(\prod_{\tilde\ell\in *S} I^\gamma_{(\mathrm{d}h)_{\tilde\ell}+1}(\beta)\right)\left(\prod_{\tilde\ell\notin *S} I^\gamma_{(\mathrm{d}h)_{\tilde\ell}}(\beta)\right)\\ &= \left(\prod_{\tilde\ell\in *S}\frac{I^\gamma_{(\mathrm{d}h)_{\tilde\ell}+1}(\beta)}{I^\gamma_{(\mathrm{d}h)_{\tilde\ell}}(\beta)} I^\gamma_{(\mathrm{d}h)_{\tilde\ell}}(\beta)\right)\left(\prod_{\tilde\ell\notin *S} I^\gamma_{(\mathrm{d}h)_{\tilde\ell}}(\beta)\right)\\ &= \left(\prod_{\tilde\ell\in *S}\frac{I^\gamma_{(\mathrm{d}h)_{\tilde\ell}+1}(\beta)}{I^\gamma_{(\mathrm{d}h)_{\tilde\ell}}(\beta)}\right)\left(\prod_{\tilde\ell} I^\gamma_{(\mathrm{d}h)_{\tilde\ell}}(\beta)\right) \quad .\end{aligned}$$

Therefore, $\langle W(C)\rangle$ is the expectation value of the product of $I^\gamma_{(\mathrm{d}h)_{\tilde\ell}+1}(\beta)/I^\gamma_{(\mathrm{d}h)_{\tilde\ell}}(\beta)$ over the weights for the dual model (6.9)

$$\boxed{\langle W(C)\rangle = \left\langle \prod_{\tilde\ell\in *S}\frac{I^\gamma_{(\mathrm{d}h)_{\tilde\ell}+1}(\beta)}{I^\gamma_{(\mathrm{d}h)_{\tilde\ell}}(\beta)}\right\rangle} \quad . \tag{6.19}$$

We can perform a similar dualisation to compute the correlation function of Polyakov loops at fixed spatial seperation $\left\langle P(\vec{x})P^\dagger(\vec{y})\right\rangle$. The Polyakov loop $P(\vec{x})$ is given by the product of $e^{i\theta_\ell}$ along a non-contractible loop which winds around the time direction once,

$$P(\vec{x}) = \exp\left(i\sum_{\tau=0}^{T-1}\theta_\ell\right) \quad , \tag{6.20}$$

where T is the length of the lattice in the time direction. After the dualisation calculation we find that

$$\boxed{\left\langle P(\vec{x})P^\dagger(\vec{y})\right\rangle = \left\langle \prod_{\tilde{\ell}\in *S} \frac{I^\gamma_{(\mathrm{d}h)_{\tilde{\ell}}+1}(\beta)}{I^\gamma_{(\mathrm{d}h)_{\tilde{\ell}}}(\beta)} \right\rangle} \quad , \tag{6.21}$$

where S is the minimal surface bounded by the two Polyakov loops.

We list the dualisation of some observables which will prove useful for simulations:

$$\left\langle \exp\left(if_p\right)\right\rangle = \left\langle \frac{I^\gamma_{(\mathrm{d}h)_{\tilde{\ell}}+1}(\beta)}{I^\gamma_{(\mathrm{d}h)_{\tilde{\ell}}}(\beta)} \right\rangle \quad , \tag{6.22}$$

$$\left\langle \exp\left(i2f_p\right)\right\rangle = \left\langle \frac{I^\gamma_{(\mathrm{d}h)_{\tilde{\ell}}+2}(\beta)}{I^\gamma_{(\mathrm{d}h)_{\tilde{\ell}}}(\beta)} \right\rangle \quad , \tag{6.23}$$

$$\left\langle \exp\left(if_{p_1}\right)\exp\left(if_{p_2}\right)\right\rangle = \left\langle \frac{I^\gamma_{(\mathrm{d}h)_{\tilde{\ell}_1}+1}(\beta)}{I^\gamma_{(\mathrm{d}h)_{\tilde{\ell}_1}}(\beta)} \frac{I^\gamma_{(\mathrm{d}h)_{\tilde{\ell}_2}+1}(\beta)}{I^\gamma_{(\mathrm{d}h)_{\tilde{\ell}_2}}(\beta)} \right\rangle \quad , \tag{6.24}$$

$$\left\langle \exp\left(if_{p_1}\right)\exp\left(-if_{p_2}\right)\right\rangle = \left\langle \frac{I^\gamma_{(\mathrm{d}h)_{\tilde{\ell}_1}+1}(\beta)}{I^\gamma_{(\mathrm{d}h)_{\tilde{\ell}_1}}(\beta)} \frac{I^\gamma_{(\mathrm{d}h)_{\tilde{\ell}_2}-1}(\beta)}{I^\gamma_{(\mathrm{d}h)_{\tilde{\ell}_2}}(\beta)} \right\rangle \quad . \tag{6.25}$$

In Eq. (6.24) and Eq. (6.25), f_{p_1} and f_{p_2} are two distinct and parallel plaquettes in different time-slices. If the two plaquettes coincide, then $\left\langle \exp\left(if_{p_1}\right)\exp\left(if_{p_2}\right)\right\rangle$ will be given by Eq. (6.23) and $\left\langle \exp\left(if_{p_1}\right)\exp\left(-if_{p_2}\right)\right\rangle = 1$.

6.3 String Tension and Insertion of Charges

Consider a system consisting of dynamical gauge fields and a static charge-anticharge pair seperated by distance r. We would like to measure the string tension by measuring the potential $V(r)$ between the charges. But this is just the energy difference between a system with and without

the charge-anticharge pair.

Suppose that H_r is the Hamiltonian of the system with the charge inserted. Then, we have

$$Z = \mathrm{tr}\left(e^{-TH_r}\right) \tag{6.26}$$

and

$$E(r) = \langle H_r \rangle = \frac{1}{Z}\,\mathrm{tr}\left(H_r e^{-TH_r}\right) = -\frac{1}{Z}\frac{\partial Z}{\partial T} \quad . \tag{6.27}$$

On the lattice, we have discretized time as

$$T = a_t L_t \quad ,$$

where a_t is the temporal lattice spacing and L_t is the number of points in the time direction. We can rewrite this in terms of the spatial lattice spacing a by using $\epsilon = a_t/a$. So, we can rewrite Eq. (6.27) as

$$E(r) = -\frac{1}{Z a L_t}\frac{\partial Z}{\partial \epsilon} \quad . \tag{6.28}$$

Now, by using the expression for Z, we should be able to express the derivative in terms of some operator in the path-integral formulation. The insertion of the charge-anticharge pair corresponds to the insertion of two Polyakov loops in the original theory. Thus, using the calculation from the previous section leading up to Eq. (6.21), we see that thet new partition function is

$$Z = \sum_{\{h_{\tilde{s}} \in \mathbb{Z}\}} \prod_{\tilde{\ell}} I^{\gamma}_{(\mathrm{d}h)_{\tilde{\ell}} + \omega_{\tilde{\ell}}}(\beta) \quad , \tag{6.29}$$

where the 1-form $\omega_{\tilde{\ell}}$ equals 1 for each dual link piercing the minimal surface S bounded by the two Polyakov loops, and equals 0 everywhere else.

In order to take the partial derivative with respect to ϵ, we need to put it back explicitly in Eq. (6.29) where it is set to 1. Recall that $\beta = 1/g^2$, where $g^2 = ae^2$ in 3D is dimensionless. So, if we had different temporal and spatial lattice constants, we would have different temporal and spatial interaction strengths

$$\beta_t = \frac{\beta}{\epsilon}, \quad \beta_s = \epsilon\beta \quad . \tag{6.30}$$

Similarly,

$$\gamma_t = \frac{\gamma}{\epsilon}, \quad \gamma_s = \epsilon\gamma \quad . \tag{6.31}$$

Hence we see that in cases where $\epsilon \neq 1$, the partition function becomes

$$Z = \sum_{\{h_{\tilde{s}} \in \mathbb{Z}\}} \left(\prod_{\tilde{\ell}_t} I_{q_{\tilde{\ell}_t}}(\beta/\epsilon, \gamma/\epsilon) \right) \left(\prod_{\tilde{\ell}_s} I_{q_{\tilde{\ell}_s}}(\epsilon\beta, \epsilon\gamma) \right) \quad , \tag{6.32}$$

where $\tilde{\ell}_t$ and $\tilde{\ell}_s$ denote the dual links piercing the temporal and spatial plaquettes respectively. I have rewritten $I_k^{\gamma}(\beta)$ as $I_k(\beta, \gamma)$ and introduced

$$q_{\tilde{\ell}} := (\mathrm{d}h)_{\tilde{\ell}} + \omega_{\tilde{\ell}}$$

to declutter the notation. Using the definition of $I_k(\beta, \gamma)$ (6.4), one can see that

$$\frac{\partial}{\partial \beta} I_k(\beta, \gamma) = \frac{I_{k+1}(\beta, \gamma) + I_{k-1}(\beta, \gamma)}{2} \tag{6.33}$$

and

$$\frac{\partial}{\partial \gamma} I_k(\beta, \gamma) = \frac{I_{k+2}(\beta, \gamma) + I_{k-2}(\beta, \gamma)}{2} \quad . \tag{6.34}$$

Let us now move on to the task of computing the partial derivative of Eq. (6.32). We see that

$$\begin{aligned} \frac{\partial Z}{\partial \epsilon} = \sum_{\{h_{\tilde{s}} \in \mathbb{Z}\}} \sum_{\tilde{\ell} \in * S_t} \left[\left(\frac{\partial}{\partial \epsilon} I_{q_{\tilde{\ell}}}(\beta/\epsilon, \gamma/\epsilon) \right) \prod_{\tilde{\ell}_t \neq \tilde{\ell}} I_{q_{\tilde{\ell}_t}}^{\gamma_t}(\beta_t) \prod_{\tilde{\ell}_s} I_{q_{\tilde{\ell}_s}}^{\gamma_s}(\beta_s) \right] \\ + \sum_{\tilde{\ell} \in * S_s} \left[\left(\frac{\partial}{\partial \epsilon} I_{(\mathrm{d}h)_{\tilde{\ell}} + \omega_{\tilde{\ell}}}(\epsilon\beta, \epsilon\gamma) \right) \prod_{\tilde{\ell}_t} I_{q_{\tilde{\ell}_t}}^{\gamma_t}(\beta_t) \prod_{\tilde{\ell}_s \neq \tilde{\ell}} I_{q_{\tilde{\ell}_s}}^{\gamma_s}(\beta_s) \quad , \right] \end{aligned}$$

where S_t and S_s are the set of temporal and spatial plaquettes respectively. Using Eq. (6.33) and Eq. (6.34),

$$\begin{aligned} \frac{\partial Z}{\partial \epsilon} = \sum_{\{h_{\tilde{s}} \in \mathbb{Z}\}} - \sum_{\tilde{\ell} \in * S_t} \left(\frac{\beta}{2\epsilon^2} \Big(I_{q_{\tilde{\ell}}+1}(\beta/\epsilon, \gamma/\epsilon) + I_{q_{\tilde{\ell}}-1}(\beta/\epsilon, \gamma/\epsilon) \Big) + \frac{\gamma}{2\epsilon^2} \Big(I_{q_{\tilde{\ell}}+2}(\beta/\epsilon, \gamma/\epsilon) + I_{q_{\tilde{\ell}}-2}(\beta/\epsilon, \gamma/\epsilon) \Big) \right) \\ \times \prod_{\tilde{\ell}_t \neq \tilde{\ell}} I_{q_{\tilde{\ell}_t}}^{\gamma_t}(\beta_t) \prod_{\tilde{\ell}_s} I_{q_{\tilde{\ell}_s}}^{\gamma_s}(\beta_s) \\ + \sum_{\tilde{\ell} \in * S_s} \left(\frac{\beta}{2} \Big(I_{q_{\tilde{\ell}}+1}(\epsilon\beta, \epsilon\gamma) + I_{q_{\tilde{\ell}}-1}(\beta/\epsilon, \gamma/\epsilon) \Big) + \frac{\gamma}{2} \Big(I_{q_{\tilde{\ell}}+2}(\epsilon\beta, \epsilon\gamma) + I_{q_{\tilde{\ell}}-2}(\beta/\epsilon, \gamma/\epsilon) \Big) \right) \\ \times \prod_{\tilde{\ell}_t} I_{q_{\tilde{\ell}_t}}^{\gamma_t}(\beta_t) \prod_{\tilde{\ell}_s \neq \tilde{\ell}} I_{q_{\tilde{\ell}_s}}^{\gamma_s}(\beta_s) \quad . \end{aligned}$$

Therefore, we see that

$$\begin{aligned}\frac{1}{Z}\frac{\partial Z}{\partial \epsilon}\bigg|_{\epsilon=1} = &-\sum_{\tilde{\ell}_t}\left\langle \frac{\beta}{2}\frac{I^{\gamma}_{q_{\tilde{\ell}_t+1}}(\beta)+I^{\gamma}_{q_{\tilde{\ell}_t-1}}(\beta)}{I^{\gamma}_{q_{\tilde{\ell}_t}}(\beta)} + \frac{\gamma}{2}\frac{I^{\gamma}_{q_{\tilde{\ell}_t+2}}(\beta)+I^{\gamma}_{q_{\tilde{\ell}_t-2}}(\beta)}{I^{\gamma}_{q_{\tilde{\ell}_t}}(\beta)}\right\rangle \\ &+\sum_{\tilde{\ell}_s}\left\langle \frac{\beta}{2}\frac{I^{\gamma}_{q_{\tilde{\ell}_s+1}}(\beta)+I^{\gamma}_{q_{\tilde{\ell}_s-1}}(\beta)}{I^{\gamma}_{q_{\tilde{\ell}_s}}(\beta)} + \frac{\gamma}{2}\frac{I^{\gamma}_{q_{\tilde{\ell}_s+2}}(\beta)+I^{\gamma}_{q_{\tilde{\ell}_s-2}}(\beta)}{I^{\gamma}_{q_{\tilde{\ell}_s}}(\beta)}\right\rangle\end{aligned}, \tag{6.35}$$

where the expectation value is over the weights for the system with charges inserted, whose partition function is given by Eq. (6.29).

Hence, we can compute the energy of the system with a pair of charge-anticharge using the following expression:

$$\boxed{\begin{aligned}aE(r) = &\frac{1}{L_t}\sum_{\tilde{\ell}_t}\left\langle \frac{\beta}{2}\frac{I^{\gamma}_{q_{\tilde{\ell}_t+1}}(\beta)+I^{\gamma}_{q_{\tilde{\ell}_t-1}}(\beta)}{I^{\gamma}_{q_{\tilde{\ell}_t}}(\beta)} + \frac{\gamma}{2}\frac{I^{\gamma}_{q_{\tilde{\ell}_t+2}}(\beta)+I^{\gamma}_{q_{\tilde{\ell}_t-2}}(\beta)}{I^{\gamma}_{q_{\tilde{\ell}_t}}(\beta)}\right\rangle \\ &-\frac{1}{L_t}\sum_{\tilde{\ell}_s}\left\langle \frac{\beta}{2}\frac{I^{\gamma}_{q_{\tilde{\ell}_s+1}}(\beta)+I^{\gamma}_{q_{\tilde{\ell}_s-1}}(\beta)}{I^{\gamma}_{q_{\tilde{\ell}_s}}(\beta)} + \frac{\gamma}{2}\frac{I^{\gamma}_{q_{\tilde{\ell}_s+2}}(\beta)+I^{\gamma}_{q_{\tilde{\ell}_s-2}}(\beta)}{I^{\gamma}_{q_{\tilde{\ell}_s}}(\beta)}\right\rangle\end{aligned}} \tag{6.36}$$

Chapter 7

Simulating the Dual Model

In this chapter, we discuss the results from our simulations of the dual model on a 3D cubic lattice. Our main result is the behaviour of the antisymmetric glueball mass, m_{--}, at different βs and γs. Using the scaling of the mass gap with the Wilson term coupling β, we compute an effective coupling β^* corresponding to a given β, γ.

Note that, unless otherwise stated, we will use terms like 'mean plaquette', 'Wilson loops', etc. to refer to the corresponding dual operator on the dual lattice.

7.1 Simulation Methods

We performed Monte Carlo simulations of the dual model on a cubic lattice of size $L_s^2 \times L_t$ with PBC. Although we performed simulations for different values L_s and L_t, the mass results presented are for $L_s = 48$, $L_t = 96$. The simulations were performed using only Metropolis sweeps. We ran the simulation for 10^7 sweeps after running it for 10^4 sweeps to ensure that it has thermalized. The data was stored after averaging it over every 100 sweeps. The system was initialized in a state where $h(x) = 0$ at all sites x.

We used the following Metropolis update:

1. For a given site x, propose an update for $h(x)$ as

$$h(x) \mapsto \tilde{h}(x) = h(x) + s \quad ,$$

where s could take value ± 1 with equal probability.

2. Compute the ratio of the weight for the new configuration $P(\tilde{h}(x))$ to that for the old configuration, $P(h(x))$. This will depend on the product of $I^{\gamma}_{(\mathrm{d}h)_\ell}(\beta)$ for the nearest neighbours.

3. Accept the proposed height $\tilde{h}(x)$ with probability min $\big(1, P(\tilde{h}(x))/P(h(x))\big)$.

4. Repeat this procedure for each site.

Performing this update for all sites constitutes one *Metropolis sweep*.

We noticed that the dual model is stiffer at smaller β. This is so severe at $\beta = 0.1$ that the mean plaquette does not show any fluctuations. We have plotted the mean plaquette in Fig. 7.1. In order to confirm that the system has reached equilibrium, we considered two additional initializations – (1) Creating an 'excitation' corresponding to $h(x) = 1$ for all sites in the time-slice $t = 0$ with $h(x) = 0$ everywhere else, and (2) random initial state. As can be seen from Fig. 7.1, all three initializations reached equilibrium quickly (with the $h(x) = 0$ initialization seemingly already at equilibrium). Small autocorrelations were observed at all β and γ values.

7.2 Advantage over direct simulation

The dual model simulations are much faster than direct simulation of the $U(1)$ LGT using link-variables. For example, it took about 300 minutes to run 10^6 Monte Carlo sweeps for the $U(1)$ LGT on a 16^3 cubic lattice. On the other hand, it took merely 10 minutes for the same runs of the dual model. It must be noted that while each Monte Carlo sweep for the link-variable simulation consisted of 1 Metropolis sweep and 2 OR sweeps, we only used Metropolis to simulate the dual model. However, the data was of equal, if not higher, quality.

We can try to understand the low autocorrelation by considering the distribution of the values taken by the degrees of freedom in the direct simulation and the dual simulation. Fig. 7.2a displays a histogram of the values of the link-variable $\theta_x(0)$ at a given site, and Fig. 7.2b displays a histogram of the values of the height variable $h(0)$ at a given. Both these variables were measured over 10^4 sweeps. Due to the large sample size, we expect these distributions to equal the theoretical distribution as per the action. Note that while the height-variable is sharply peaked at 0, the link-variable appears to have a uniform distribution. This means that it is much easier to draw a 'representative' sample for the height-variable as compared to the link-variable.

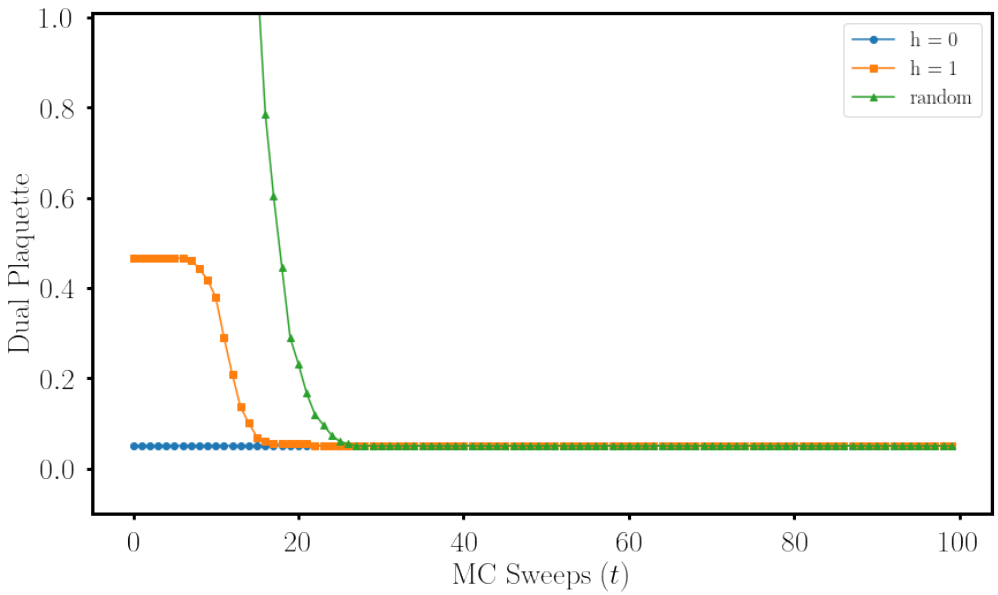

(a)

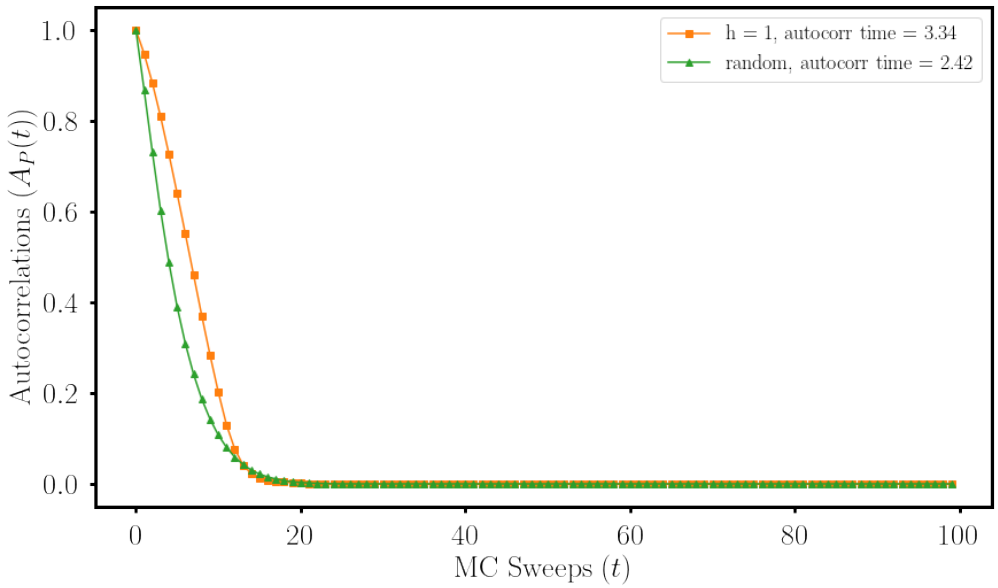

(b)

Figure 7.1: The system is extremely stiff at $\beta = 0.1$. We can see that the system has thermalized by monitoring the system with three different initial conditions – (1) $h(x) = 0$, (2) $h(x) = 1$ at time-slice $t = 0$ but 0 everywhere else, and (3) random heights. We can see from the (a) mean plaquette and (b) autocorrelation in the mean plaquette, that the system reaches equilibrium very quickly for all three cases. For (1), the mean plaquette is the same at all sweeps, so autocorrelation is ill-defined.

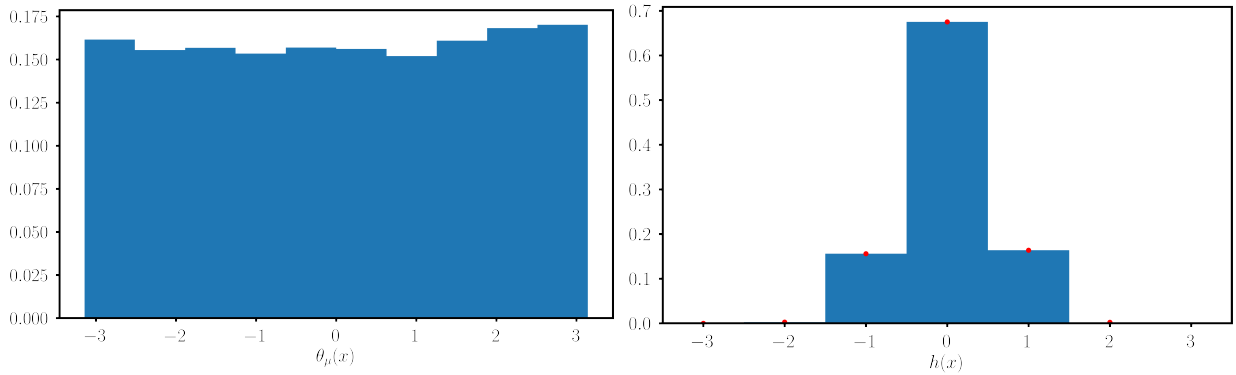

(a) (b)

Figure 7.2: Figure (a) displays the histogram of the values taken by a link-variable $\theta_x(0)$, and (b) displays the histogram of the values taken by a height variable $h(0)$. Markers have been added to (b) to improve visibility.

7.3 The Mean Plaquette

As before, we use the mean plaquette to perform the preliminary analysis. Its dual operator is given by

$$\tilde{P} := \frac{1}{N_{\tilde{\ell}}} \sum_{\tilde{\ell}} \frac{I^{\gamma}_{(\mathrm{d}h)_{\tilde{\ell}}+1}(\beta)}{I^{\gamma}_{(\mathrm{d}h)_{\tilde{\ell}}}(\beta)} \quad , \tag{7.1}$$

where $N_{\tilde{\ell}}$ is the total number of links in the dual lattice.

By performing simulations on a 16^3 lattice, we found that the mean plaquette computed using the dual model agrees with the direct simulations. Fig. 7.3 presents the plots of data from the dual model and the $U(1)$ LGT at $\gamma = 0.0$.

7.3.1 Effect of γ

We simulated the model at $\gamma = 0.0, 0.1, 0.2, 0.3, 0.4, 0.5$. Fig. 7.4 displays the plots of the mean plaquette at different values of β and γ. We can see that increasing γ leads to a faster approach of the mean plaquette the continuum value.

The values of the mean plaquette for β ranging from 1.4 to 2.3 in 0.1 increments at different γ is presented in Table 7.1. The data is mostly from simulations on a $48^2 \times 96$ lattice. The mean plaquette at $\beta = 1.4, \gamma = 0.4$. was computed for a 16^3 lattice. Although finite sized corrections to a local operator like the mean plaquette are negligible, the relatively small number of sweeps has led to a relatively larger error.

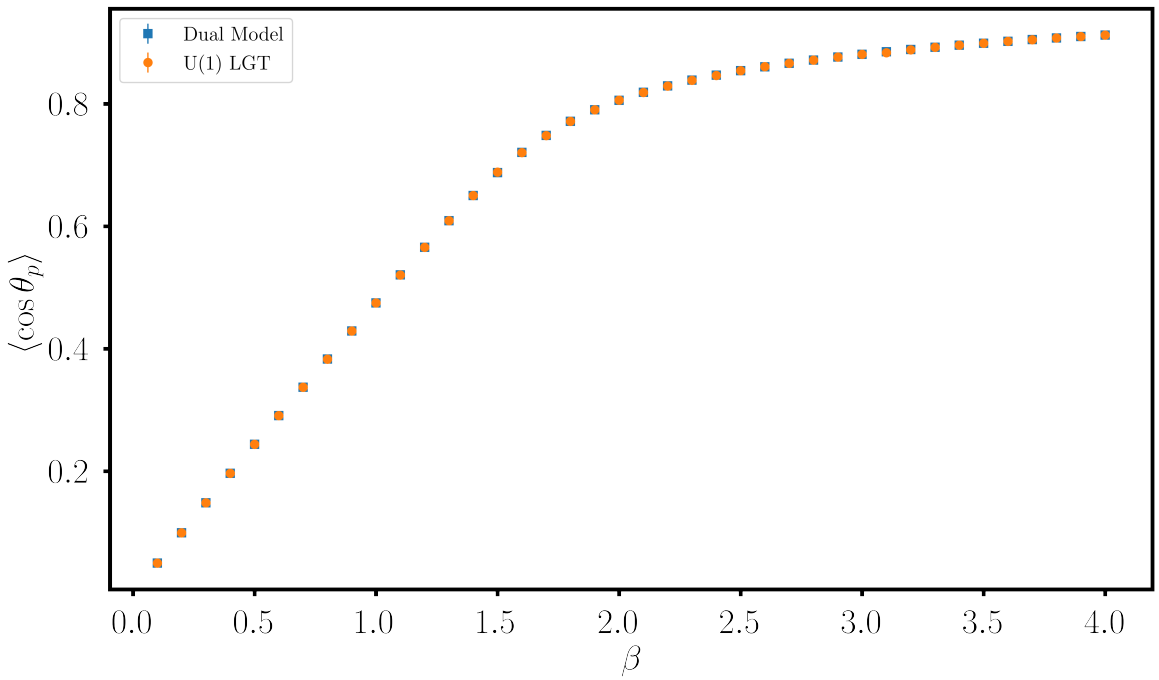

Figure 7.3: Mean plaquette data from simulation of the $U(1)$ LGT using link-variables and from simulation of the dual model show agreement.

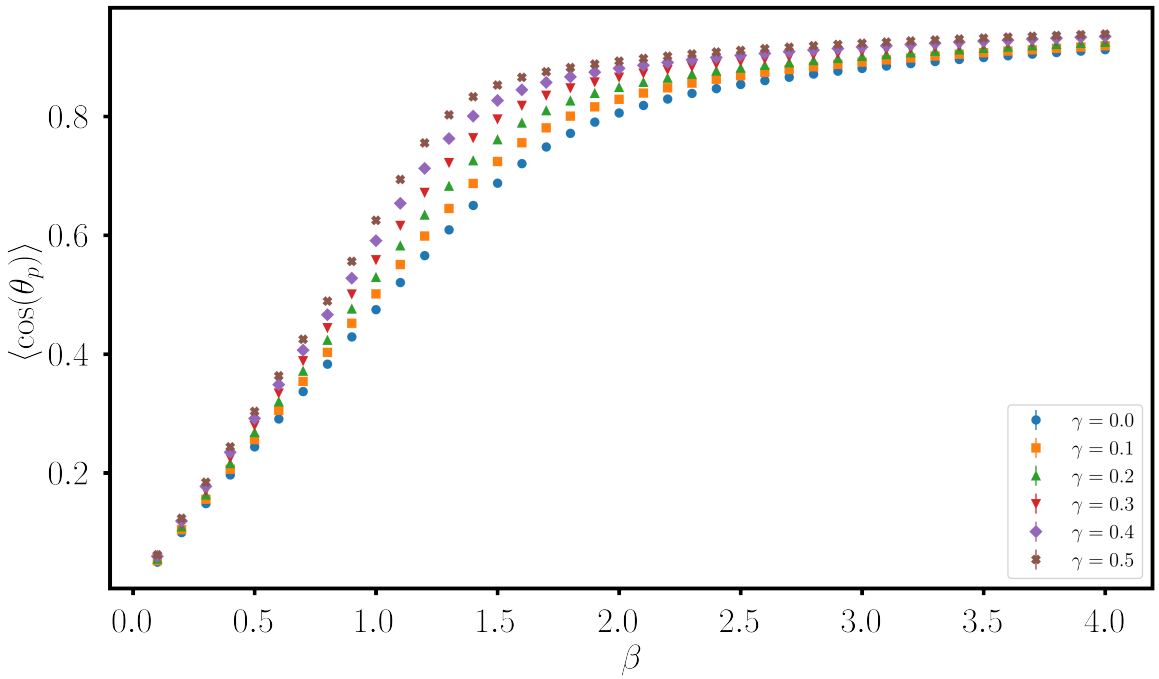

Figure 7.4: The mean plaquette as a function of β at different γ for a 16^3 cubic lattice.

	$\gamma = 0.0$	0.1	0.2	0.3	0.4	0.5
$\beta = 1.4$	0.6502916(4)	0.6873613(4)	0.7255523(5)	0.7639055(5)	0.8006(1)	0.8334329(5)
1.5	0.6877331(4)	0.7245620(4)	0.7610583(4)	0.7957443(5)	0.8268315(4)	0.8529230(4)
1.6	0.7206439(4)	0.7556780(4)	0.7888903(4)	0.8188984(4)	0.8446288(4)	0.8657827(3)
1.7	0.7485844(4)	0.7807496(4)	0.8100664(4)	0.8356698(3)	0.8572412(3)	0.8750412(2)
1.8	0.7716944(3)	0.8005749(3)	0.8261891(3)	0.8482113(3)	0.8667620(2)	0.8822434(2)
1.9	0.7905632(3)	0.8162751(3)	0.8387571(3)	0.8580317(2)	0.8743748(2)	0.8881653(2)
2.0	0.8059860(3)	0.8289232(3)	0.8488889(2)	0.8660621(2)	0.8807326(2)	0.8932194(2)
2.1	0.8187441(3)	0.8393649(2)	0.8573307(2)	0.8728585(2)	0.8862077(2)	0.8976409(2)
2.2	0.8294889(2)	0.8482072(2)	0.8645612(2)	0.8787597(2)	0.8910240(2)	0.9015779(1)
2.3	0.8387155(2)	0.8558613(2)	0.8708871(2)	0.88397812(2)	0.8953263(1)	0.9051272(1)

Table 7.1: Mean plaquette for different β (rows) and γ (columns). The error for $\beta = 1.4, \gamma = 0.4$ is relatively high because that value is from a 10^4 sweeps simulation whereas the rest are from 10^7 sweeps simulations.

7.4 The Mass Gap

We study the mass gap by studying the mass of the lowest glueball state, i.e. the $J^{PC} = 0^{--}$ antisymmetric state. We do this by measuring the time-slice correlators of the dual operators corresponding to $P_- = \sin\theta_p$. In practice, we measure the following time-slice operators

$$p_+(t) := \frac{1}{L_s^2}\sum_{\vec{r}} \frac{I^\gamma_{\mathrm{d}h_r+1}(\beta)}{I^\gamma_{\mathrm{d}h_r}(\beta)}, \quad p_-(t) := \frac{1}{L_s^2}\sum_{\vec{r}} \frac{I^\gamma_{\mathrm{d}h_r-1}(\beta)}{I^\gamma_{\mathrm{d}h_r}(\beta)} \quad , \tag{7.2}$$

where $\mathrm{d}h_r := h(\vec{r}, t+1) - h(\vec{r}, t)$. These correspond to the time-slice average of $\exp\big(i\theta_p\big)$ and $\exp\big(-i\theta_p\big)$. By using

$$\sin\theta_p = \frac{\exp\big(i\theta_p\big) - \exp\big(-i\theta_p\big)}{2}$$

we compute the correlators $P_-(0)P_-(t)$. The mass m, in lattice units, is extracted by fitting the correlation function to

$$P_-(0)P_-(\tau) = c\left[e^{-m\tau} + e^{-m(L_t-\tau)}\right] \quad . \tag{7.3}$$

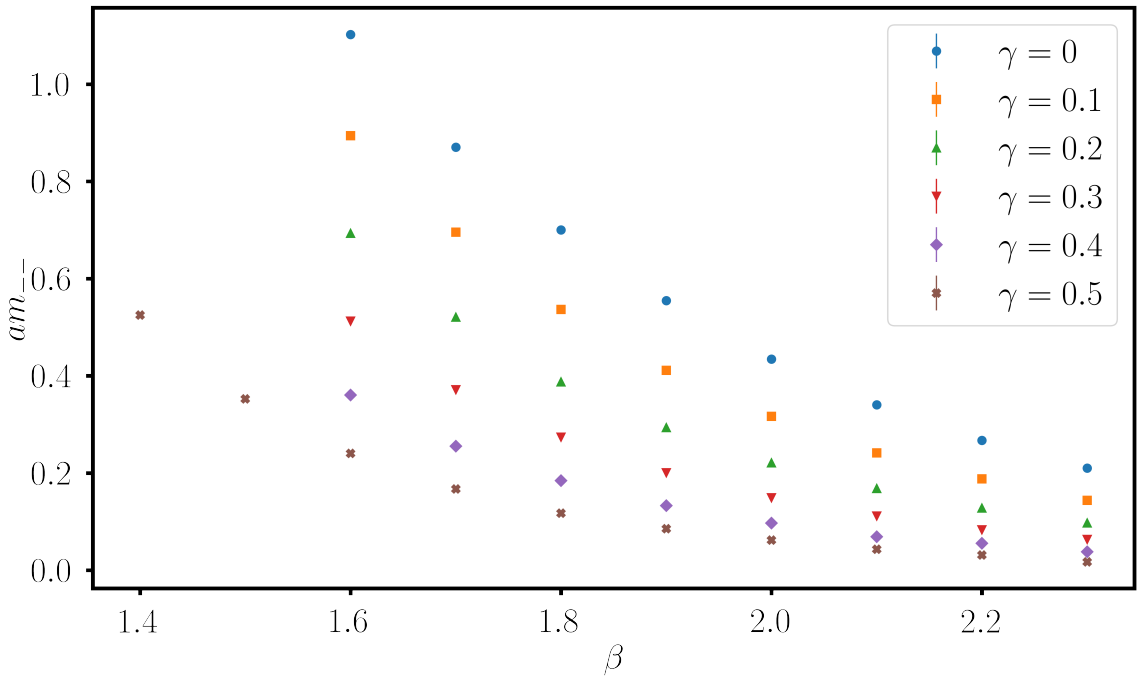

Figure 7.5: The antisymmetric glueball mass m_{--} plotted against β for different values of γ.

We were able to benchmark our code against the results provided in Athenodorou and Teper (A&T) [9]. Our antisymmetric glueball mass am_{--} (in lattice units, a being the lattice spacing) agrees with their results for different lattice sizes. The mass results that we present here are for data collected from simulations of the system on a $48^2 \times 96$ cubic lattice. We performed simulations at β ranging from 1.6 to 2.3 at increments of 0.1, and $\gamma = 0.0, 0.1, 0.2, 0.3, 0.4, 0.5$. Our results have been presented in Table 7.2. The errors were computed by performing a bootstrap analysis.

For $\beta = 1.4, 1.5$, the signal-to-noise ratio decreased very quickly with t and thus our estimates aren't reliable and haven't been presented. However, we could get good quality data for $\gamma = 0.5$ and the corresponding results have been provided. Fig. 7.5 displays the antisymmetric mass at different couplings. We can observe that the mass becomes smaller with an increase in β. The presence of γ causes this to happen faster.

Fig. 7.6 shows correlation data and our fits at different couplings. The behaviour in Fig. 7.6a is representative of a regime where we can perform a good fit. From the scaling behaviour of the mass

gap m_D, we expect m_{--} to decrease with β. Fig. 7.6b shows a sharp drop in correlation. This is due to the large mass at this coupling. Fitting the points at small τ showed that $m_{--} \approx 1.4$. This means that the correlation length is $m^{-1} \approx 0.7$ which is comparable to the lattice spacing. We believe that Fig. 7.6c shows finite volume effects. Ideally our analysis is supposed to be performed in the thermodynamic limit. In practice, we can avoid finite volume effects if $L_t >> l_D \approx m_D^{-1}$. However, at given couplings, we found $m_{--} = 0.03$. This means that the correlation length $l_D \approx 33$ is comparable to the size of the box, $L_s = 48$ leading to detectable finite volume effects.

	$\gamma = 0.0$	0.1	0.2	0.3	0.4	0.5
$\beta = 1.4$	-	-	-	-	-	0.5250(8)
1.5	-	-	-	-	-	0.3525(6)
1.6	1.102(1)	0.894(2)	0.693(1)	0.5125(8)	0.3604(6)	0.2404(6)
1.7	0.870(5)	0.6955(6)	0.5207(8)	0.3713(9)	0.2553(5)	0.1673(4)
1.8	0.700(1)	0.5367(5)	0.3877(9)	0.2738(5)	0.1844(5)	0.1174(6)
1.9	0.5548(8)	0.4111(6)	0.2937(5)	0.2006(5)	0.1331(4)	0.0855(4)
2.0	0.4342(6)	0.3166(6)	0.2210(4)	0.1492(4)	0.0969(5)	0.0621(4)
2.1	0.3405(5)	0.2415(7)	0.1684(4)	0.1115(4)	0.0690(6)	0.0434(5)
2.2	0.2672(5)	0.1879(4)	0.1280(4)	0.0831(3)	0.0556(5)	0.0315(3)
2.3	0.2101(6)	0.1439(4)	0.0974(3)	0.0634(4)	0.0380(4)	0.0174(5)

Table 7.2: Antisymmetric glueball mass am_{--} for different β (rows) and γ (column) values.

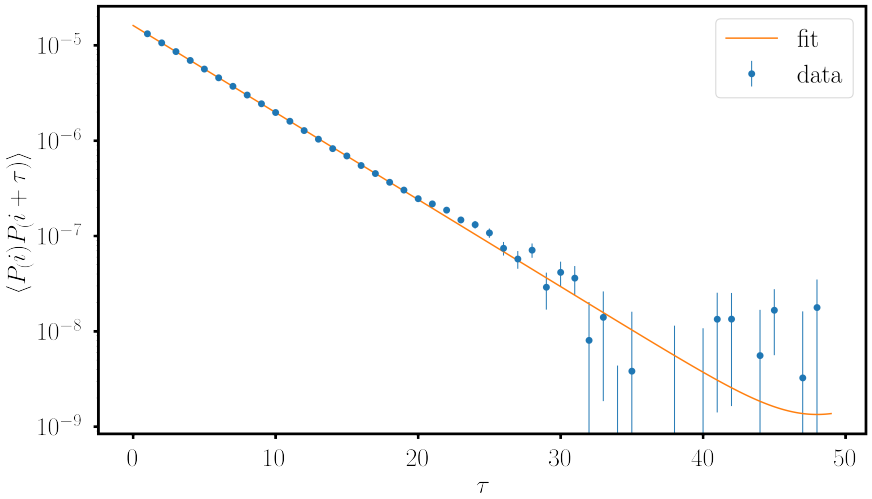

(a) $\beta = 2.3$, $\gamma = 0.0$

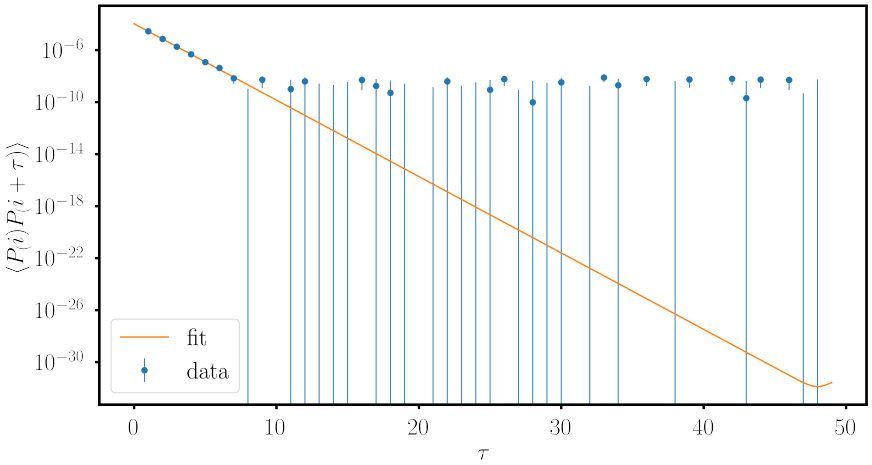

(b) $\beta = 1.5$, $\gamma = 0.0$

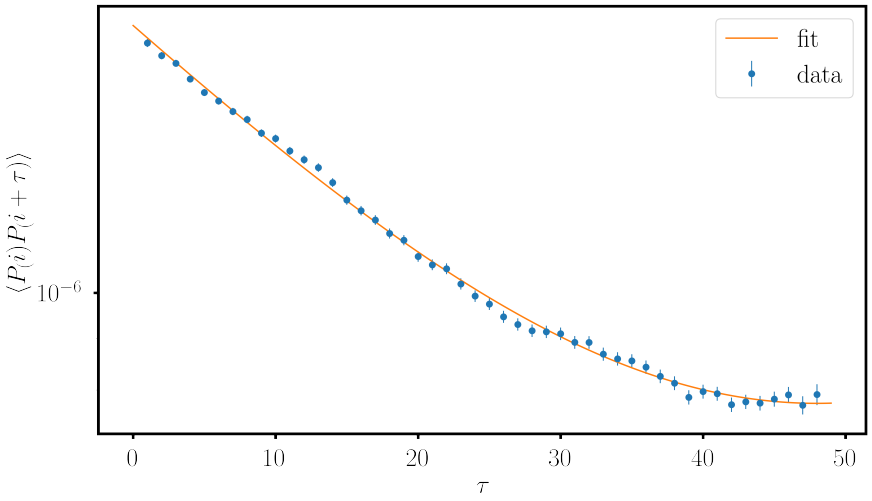

(c) $\beta = 2.2$, $\gamma = 0.5$

Figure 7.6: Correlators plotted against τ which were used to extract the masses. The fitted curve is also shown. Note the increase in relative error at large τ.

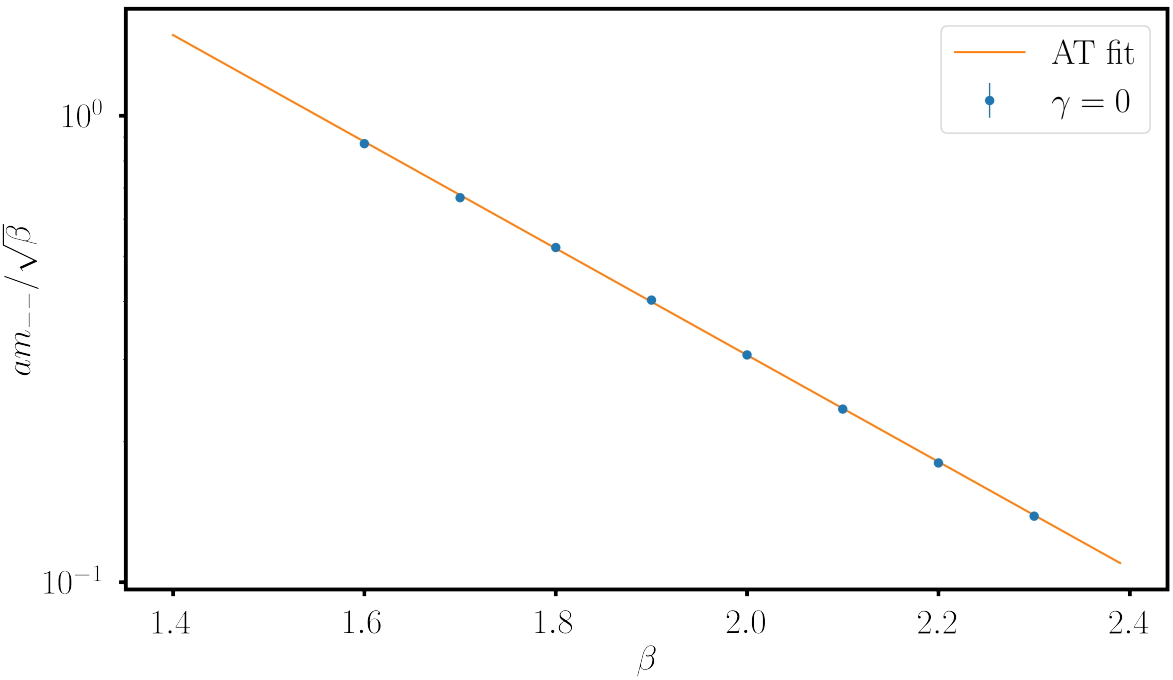

Figure 7.7: $am_{--}/\sqrt{\beta}$ has been plotted against β on a log-linear scale. The solid line is the predicted behaviour with the parameters taken from A&T.

7.4.1 Effect of γ

From Fig. 7.5, we can see that γ causes the masses to asymptote to the limiting value of 0 faster. We would like to make this precise.

Recall that for large β, the mass gap am_D scales with β as

$$a^2 m_D^2 = 8\pi^2 \beta \exp\{-2\pi^2 v(0)\beta\} \quad . \tag{7.4}$$

By plotting $am_{--}/\sqrt{\beta}$ against β on a log-linear plot, A&T [9] determined that for $1.7 \geq \beta \geq 2.8$

$$\frac{am_{--}}{\sqrt{\beta}} = 59.4(1.1)\exp(-2.633(10)\beta) \quad . \tag{7.5}$$

We observed that our masses for $\gamma = 0.0$ lies on this curve with the above parameters as shown in Fig. 7.7.

We compute an effective coupling β^* corresponding to each pair (β, γ) by using the scaling behaviour of the mass gap m_D. Using the parameters determined by A&T, we solve the following

equation for β^*,

$$am_{--}(\beta,\gamma) = 59.4(1.1)\sqrt{\beta^*}\exp(-2.633(10)\beta^*) \quad . \tag{7.6}$$

The resulting $\beta^*(\beta,\gamma)$ has been plotted in Fig. 7.8 and Fig. 7.9.

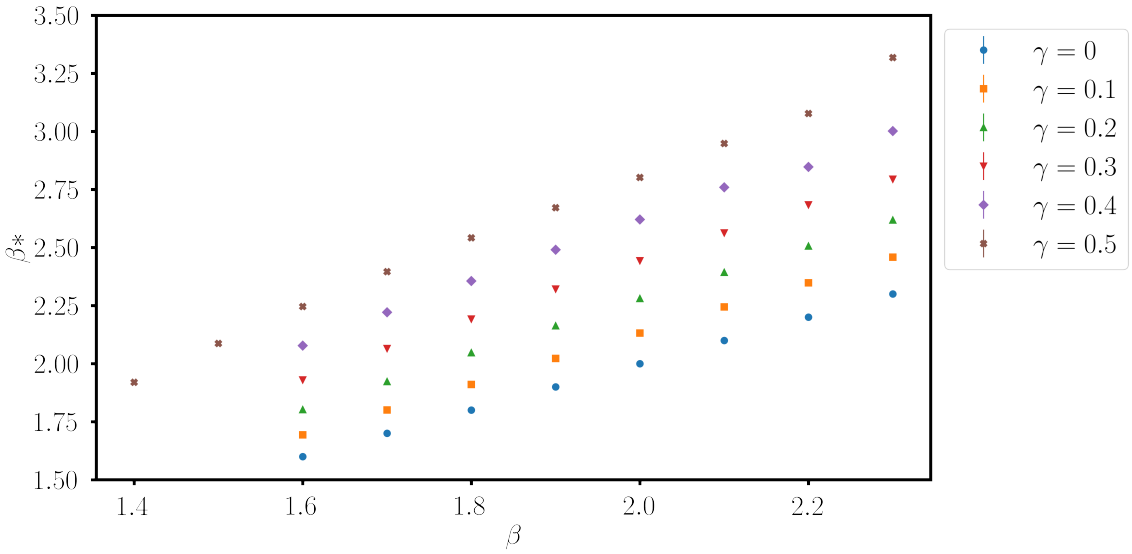

Figure 7.8: The effective coupling β^* as a function of β for different γ values.

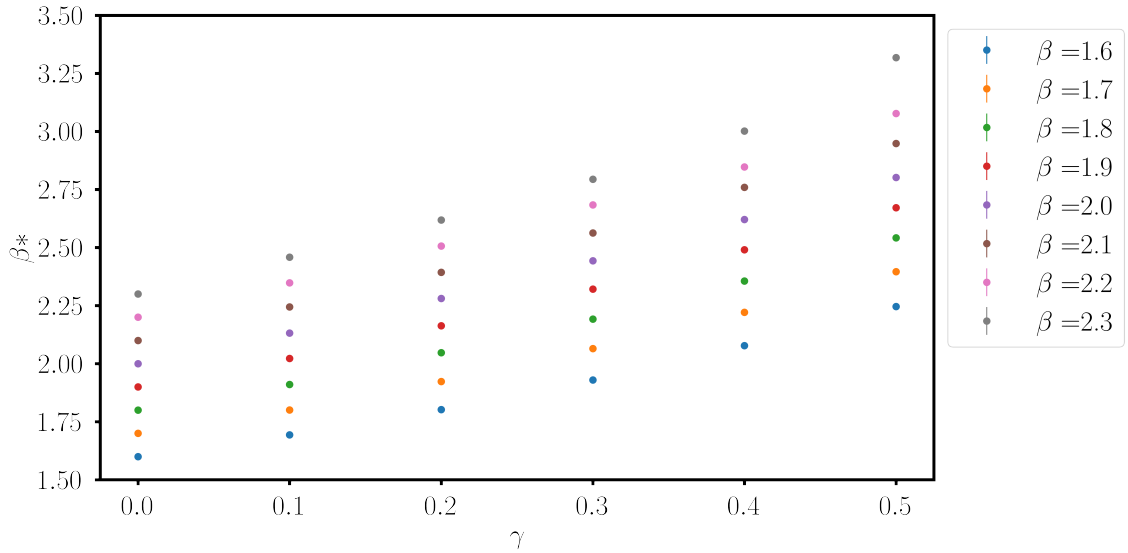

Figure 7.9: The effective coupling β^* as a function of γ for different β values.

We can see that β^* appears to scale linearly with β with a γ-dependent slope. On the other hand, β^* appears to scale non-linearly with γ.

7.5 Inter-charge Potential

We tried to measure the inter-charge potential in our system by inserting charge-anticharge pairs as discussed in the previous chapter. This is a work in progress, and we intend to thoroughly analyse the potential in the future. Currently, our measurements at $\gamma = 0.0$ do not agree with the literature.

The data from a $16^2 \times 24$ lattice at $\beta = 2.0$ has been plotted in Fig. 7.10. It shows the energy $E(r)$ for a system containing a charge-anticharge pair separated by a distance r. We can directly determine the string tension from this data by performing a curve fit.

In order to visualise the effect of the charges, we measured the energy density at each spatial plaquette, averaged over all time-slices. This is displayed in Fig. 7.11.

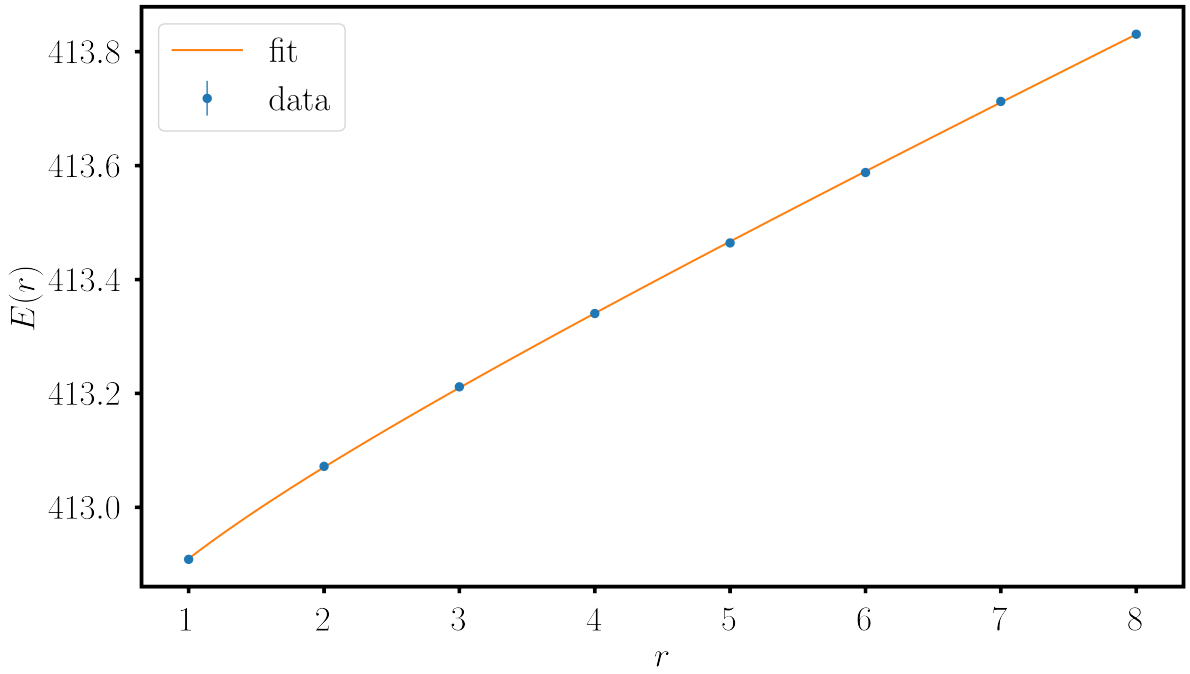

Figure 7.10: The energy of the system containing charge-anticharge pair separated by r.

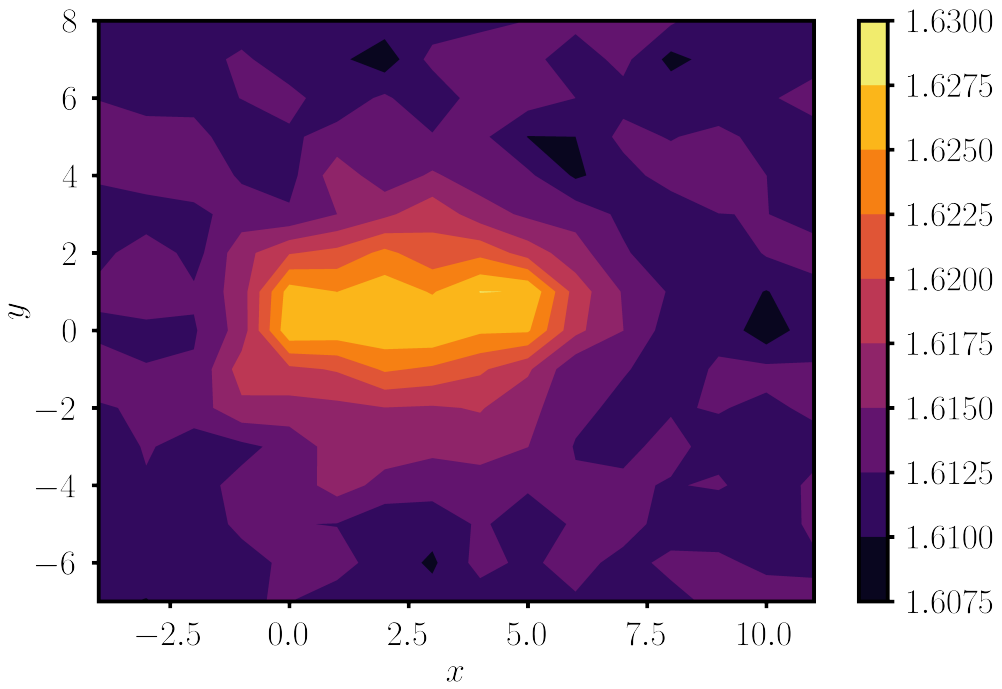

Figure 7.11: The energy density on each spatial plaquette. We can see the confined flux tubes joining the charge and the anti-charge seperated by $r = 6$.

Chapter 8

$U(1)$ LGT on Triangular Lattice

In this chapter, we discuss the 3D $U(1)$ LGT on a triangular lattice. We will discuss the preliminary results from Monte Carlo simulations. We also compute the mean plaquette by performing a strong-coupling expansion to validate the simulations.

There are several active efforts to simulate $2+1$ dimensional $U(1)$ LGT using quantum systems. As compared to a square lattice, it is easier to experimentally implement this model on a triangular lattice because that would involve three-body interactions instead of four-body interactions. While there have been studies of the Hamiltonian $U(1)$ LGT on a triangular lattice [38][39][40], we aim to study the system using a path-integral approach. This motivates us to construct a 3D 'triangular' lattice. Moreover, universality assures us that the exact details of the lattice should be irrelevant for the long-distance behaviour of the system. Hence, we would like to compare the results on this lattice with the standard results.

8.1 The Triangular Lattice

We construct our 3D lattice by stacking the familiar 2D triangular lattice on top of each other. The sites of adjacent triangular lattices are connected by time-like links. Thus, each time-slice of our lattice is a 2D triangular lattice. Fig. 8.1 illustrates a time-slice of the lattice and Fig. 8.5 shows a unit cell of the lattice. We term this, inaccurately, as the 3D triangular lattice.

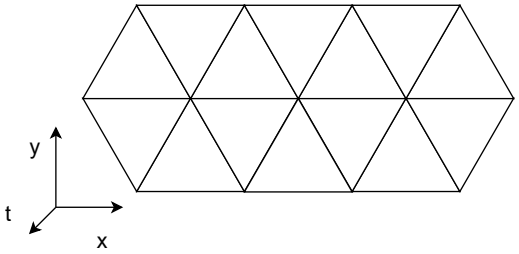

Figure 8.1: A time-slice of the triangular lattice.

We study the $U(1)$ LGT with the extended action,

$$\boxed{S = -\sum_{\square} [\beta_t \cos\theta_{\square} + \gamma_t \cos 2\theta_{\square}] - \sum_{\triangle} [\beta_s \cos\theta_{\triangle} + \gamma_s \cos 2\theta_{\triangle}]} \quad , \tag{8.1}$$

where the first sum is over the square temporal plaquettes and the second sum is over the triangular spatial plaquettes. Since our lattice is anisotropic, we need to treat the triangular spatial and square temporal plaquettes on an unequal footing. The spatial and temporal couplings are given by

$$\beta_t := \zeta^{-1}\beta, \quad \beta_s := \zeta\beta$$

where $\beta = 1/a_s g^2$, and $\zeta = a_t/a_s$ measures the anisotropy of the lattice. γ_t and γ_s are similarly defined. We use a straightforward generalisation of the usual plaquette operator to define the triangular plaquette as

$$\theta_{\triangle} := \theta_x(r) + \theta_m(r + \hat{x}) - \theta_l(r) \quad , \tag{8.2}$$

where $\hat{m}$ and $\hat{l}$ are unit vectors along the edges of 2D triangular lattice. The square plaquette is defined as usual,

$$\theta_{\square} := \theta_k(x) + \theta_t(x + \hat{k}) - \theta_k(x + \hat{t}) - \theta_t(x) \quad , \tag{8.3}$$

where, $\hat{k}$ is one of the spatial unit vectors: $\hat{x}$, $\hat{m}$, $\hat{l}$. Both of these plaquettes are illustrated in Fig. 8.3.

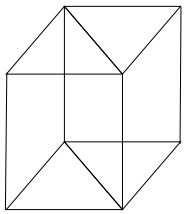

Figure 8.2: A unit cell of the triangular lattice.

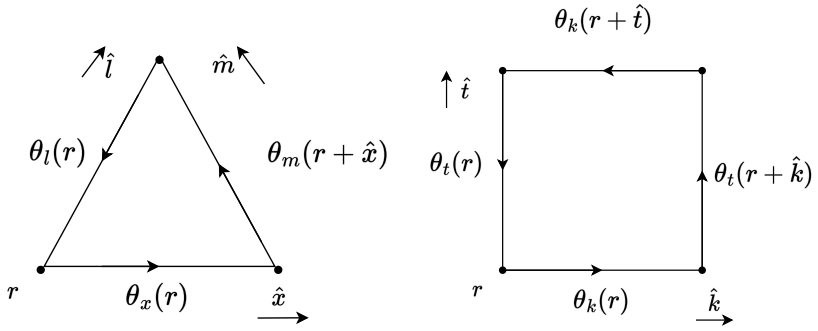

Figure 8.3: The (a) spatial, and (b) temporal plaquettes.

We will focus on the case with $\gamma = 0.0$. In order to benchmark our code, we will perform a strong-coupling expansion calculation.

8.1.1 The Dual Lattice

The duality mapping to the dual model also be performed for the triangular lattice and it proceeds exactly as before. For a triangular lattice with N sites, the dual lattice is a 3D *honeycomb* lattice with $2N$ sites. The honeycomb lattice consists of 2D honeycomb lattices stacked on top of each other. The extra factor of 2 arises from the fact that the dual of a 2D triangular lattice is a 2D honeycomb lattice with 2 dual sites for each site.

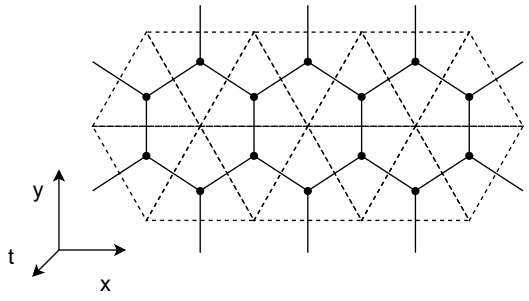

Figure 8.4: A time-slice of the honeycomb lattice is a 2D honeycomb lattice. The triangular lattice is also displayed in dashed lines.

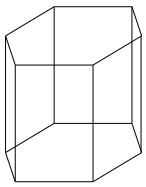

Figure 8.5: A unit cell of the honeycomb lattice.

8.2 Strong-coupling Expansion

Let us consider the Wilson action for the system ($\gamma = 0$). The partition function is given by

$$\begin{aligned} Z &= \int \mathcal{D}\theta \, \exp\left(\beta_t \sum_{\square} \cos\theta_{\square} + \beta_s \sum_{\triangle} \cos\theta_{\triangle}\right) \\ &= \int \mathcal{D}\theta \, \prod_{\square} \left(e^{\beta_t \cos\theta_{\square}}\right) \prod_{\triangle} \left(e^{\beta_s \cos\theta_{\triangle}}\right) \quad , \end{aligned} \tag{8.4}$$

where the integral is over all the link variables

$$\int \mathcal{D}\theta \; := \prod_{\ell} \int_{-\pi}^{\pi} \frac{\mathrm{d}\theta_\ell}{2\pi} \quad .$$

The strong coupling expansion consists in expanding the exponentials of Eq.(8.4) in powers of β. In the limit $\beta \to 0$ (or $g \to \infty$ i.e. *strong coupling*), we can approximate Z with the first few terms. This gives us an expansion of the Z in terms of powers of cosines.

8.2.1 Diagrams

Upon expanding the exponentials in Eq. (8.4) using Taylor series, we find

$$Z = \int \mathcal{D}\theta \, \prod_{\square} \left(\sum_n \frac{\beta_t^n}{n!} \cos^n\theta_{\square}\right) \prod_{\triangle} \left(\sum_m \frac{\beta_s^m}{m!} \cos^m\theta_{\triangle}\right) \quad . \tag{8.5}$$

Thus, the partition function is a series over integrals of finite products of cosines. Since

$$\int_{-\pi}^{\pi} \frac{\mathrm{d}\theta}{2\pi} \cos^k(\theta + a) = 0$$

for an odd k, we only need to consider terms with even powers of cosines, and terms where the same link variable appears more than once.

	Diagram	Integral	Value	Coefficient
$d_1^{(2)}$		$\frac{\beta_t^2}{2!}\int \mathcal{D}\theta\ \cos^2\theta_{\square}$	$\frac{\beta_t^2}{4}$	$a_1^{(2)} = 3N$
$d_2^{(2)}$		$\frac{\beta_s^2}{2!}\int \mathcal{D}\theta\ \cos^2\theta_{\triangle}$	$\frac{\beta_s^2}{4}$	$a_2^{(2)} = 2N$
$d_1^{(4)}$		$\frac{\beta_t^4}{4!}\int \mathcal{D}\theta\ \cos^4\theta_{\square}$	$\frac{3}{8\cdot 4!}\beta_t^4$	$a_1^{(4)} = 3N$
$d_2^{(4)}$		$\frac{\beta_s^4}{4!}\int \mathcal{D}\theta\ \cos^4\theta_{\triangle}$	$\frac{3}{8\cdot 4!}\beta_s^4$	$a_2^{(4)} = 2N$
$d_3^{(4)}$	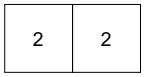	$\left(\frac{\beta_t^2}{2!}\right)^2\int \mathcal{D}\theta\ \cos^2\theta_{\square_1}\cos^2\theta_{\square_2}$	$\frac{1}{16}\beta_t^4$	$a_3^{(4)} = 18N$
$d_4^{(4)}$	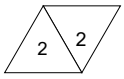	$\left(\frac{\beta_s^2}{2!}\right)^2\int \mathcal{D}\theta\ \cos^2\theta_{\triangle_1}\cos^2\theta_{\triangle_2}$	$\frac{1}{16}\beta_s^4$	$a_4^{(4)} = 3N$
$d_5^{(4)}$	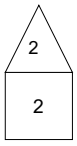	$\left(\frac{\beta_t^2}{2!}\right)\left(\frac{\beta_s^2}{2!}\right)\int \mathcal{D}\theta\ \cos^2\theta_{\square_1}\cos^2\theta_{\triangle_2}$	$\frac{1}{16}\beta_t^2\beta_s^2$	$a_5^{(4)} = 12N$
$d_6^{(4)}$	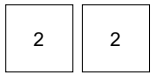	$\left(\frac{\beta_t^2}{2!}\int \mathcal{D}\theta\ \cos^2\theta_{\square}\right)^2$	$\frac{1}{16}\beta_t^4$	$a_6^{(4)} = \frac{3N(3N-13)}{2}$
$d_7^{(4)}$	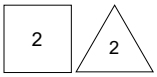	$\left(\frac{\beta_t^2}{2!}\int \mathcal{D}\theta\ \cos^2\theta_{\square}\right)\left(\frac{\beta_s^2}{2!}\int \mathcal{D}\theta\ \cos^2\theta_{\triangle}\right)$	$\frac{1}{16}\beta_t^2\beta_s^2$	$a_7^{(4)} = 6N(N-2)$
$d_8^{(4)}$	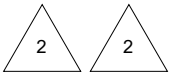	$\left(\frac{\beta_s^2}{2!}\int \mathcal{D}\theta\ \cos^2\theta_{\triangle}\right)^2$	$\frac{1}{16}\beta_s^4$	$a_8^{(4)} = 2N(N-2)$
$d_1^{(5)}$	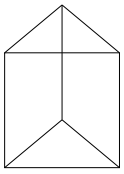	$\beta_t^3\beta_s^2\int \mathcal{D}\theta\ \cos\theta_{\triangle_1}\cos\theta_{\triangle_2}\cos\theta_{\square_1}\ldots\cos\theta_{\triangle_3}$	$\frac{1}{16}\beta_t^3\beta_s^2$	$a_1^{(5)} = 2N$

Table 8.1: The strong-coupling expansion diagrams, along with their coefficients up to order β^5

There is a nice geometric interpretation for these terms. For example, all terms of order β^2 are given by a $\cos^2\theta_p$ corresponding to some plaquette. These are denoted by the diagrams $d_1^{(2)}$ and $d_2^{(2)}$. Similarly, we will have other diagrams as shown in Table 8.1. Every diagram represents a generic integral multiplied with an appropriate power of β and the factorials arising from the Taylor expansion. We denote the kth diagram containing β^n by $d_k^{(n)}$. In the table, we have also drawn a

graphical representation of each $d_k^{(n)}$. The number inside each 'plaquette' in the diagram denotes the power of that plaquette in the corresponding integral. For example, n inside a square corresponds to a factor of $\cos^n \theta_\square$ in the integrand. Note that the diagram $d_1^{(5)}$ is significant, because it is formed by a product of $\cos\theta_p$ forming the simplest closed surface – the elementary prism.

A particular diagram, $d_k^{(n)}$, will arise in the expansion (8.5) multiple times, depending on how many such geometric 'motifs' occur on the lattice with N sites. We need to count all such occurrences to determine the coefficient for the diagram, $a_k^{(n)}$. Thus, the partition function can be written as

$$Z = 1 + a_1^{(2)} d_1^{(2)} + a_2^{(2)} d_2^{(2)} + \dots \quad . \tag{8.6}$$

Diagram Values

The integrals corresponding to each of the diagrams are shown in Table 8.1. Diagrams with shared links between plaquettes denote integrals where the same link variable shows up in multiple cosines. The values for the diagrams can be computed using the following integrals:

$$\begin{aligned}
\int_{-\pi}^{\pi} \frac{\mathrm{d}\theta}{2\pi} \cos^2(\theta + a) &= \frac{1}{2} \quad , \\
\int_{-\pi}^{\pi} \frac{\mathrm{d}\theta}{2\pi} \cos^4(\theta + a) &= \frac{3}{8} \quad , \\
\int_{-\pi}^{\pi} \frac{\mathrm{d}\theta}{2\pi} \cos(\theta + a)\cos(\theta + b) &= \frac{1}{2}\cos(a - b) \quad , \\
\int_{-\pi}^{\pi} \frac{\mathrm{d}\theta}{2\pi} \cos^2(\theta + a)\cos^2(\theta + b) &= \frac{1}{4} + \frac{1}{8}\cos(2a - 2b) \quad .
\end{aligned}$$

Combinatorics

To determine the coefficients $a_k^{(n)}$, we need to count how many times a particular motif appears in the lattice. Here, we list the multiplicities of various motifs and the corresponding $a_k^{(n)}$s. Recall that we are working on the triangular lattice (as shown in Figs. 8.1 and 8.5) with PBC.

Square plaquette

Each square plaquette corresponds to a link on the triangular lattice. There are 3 links per site, i.e. there are $3N$ square plaquettes $\Rightarrow a_1^{(2)} = a_1^{(4)} = 3N$.

Triangular plaquette

There are 2 triangular plaquettes per site on each 2D triangular lattice, i.e. there are $2N$ triangular plaquettes $\Rightarrow a_2^{(2)} = a_2^{(4)} = 2N$.

Square plaquettes sharing a link

We can have either a horizontal or a vertical pair. Each horizontal pair shares a time-like link. There are N time-like links, one corresponding to each site. At each link, 6 square plaquettes meet, of which we need to choose 2. So, there are $\binom{6}{2} = 15$ pairs per link, i.e. $15N$ total horizontal pairs. Each vertical pair shares a space-like link. There are $3N$ distinct space-like links. There is a one-to-one correspondence between a space-like link and a vertical plaquette pair. Hence, we have $18N$ pairs in total $\Rightarrow a_3^{(4)} = 18N$.

Triangular plaquettes sharing a link

There is a one-to-one correspondence between such pairs and space-like links. Hence, there are $3N$ such pairs $\Rightarrow a_4^{(4)} = 3N$.

Triangular and square plaquette sharing a link

Choose a square plaquette, there are $3N$ ways to do this. Each such plaquette is connected to 4 triangular plaquettes. Hence, there are $12N$ such pairs $\Rightarrow a_5^{(4)} = 12N$.

Square plaquette pairs not sharing a link

The first plaquette can be chosen in $3N$ ways. This is connected to 12 other square plaquettes. So, the second plaquette has to be chosen from the remaining $3N - 13$. We need to divide by two to prevent overcounting $\Rightarrow a_6^{(4)} = 3N(3N - 13)/2$.

Pair of square and triangular plaquettes not sharing a link

We can choose the square plaquette in $3N$ ways. This is connected to 4 triangular plaquettes. So, the second plaquette has to be chosen from the remaining $2N - 4$. Hence, there are $6N(N - 2)$ such pairs $\Rightarrow a_7^{(4)} = 6N(N - 2)$.

Triangular plaquette pairs not sharing a link

The first plaquette can be chosen in $2N$ ways. This is connected to 3 other triangular plaquettes. So, the second plaquette has to be chosen from the remaining $2N-4$. We need to divide by two to prevent overcounting $\Rightarrow a_8^{(4)} = 2N(N-2)$.

Prisms

We can associate a prism to each triangular plaquette. Hence, there are $2N$ prisms $\Rightarrow a_1^{(5)} = 2N$.

8.2.2 The 'Free Energy'

We can compute the expectation values of the spatial and temporal plaquettes by taking appropraite derivatives of the free energy per site,

$$F = \frac{1}{N}\log Z \quad . \tag{8.7}$$

We expect this to be independent of N. We will see that this will occur because of some nice cancellations. We have $Z = 1 + x$, with

$$\begin{aligned} x = \quad & a_1^{(2)} d_1^{(2)} + a_2^{(2)} d_2^{(2)} \\ & + a_1^{(4)} d_1^{(4)} + a_2^{(4)} d_2^{(4)} + a_3^{(4)} d_3^{(4)} + a_4^{(4)} d_4^{(4)} + a_5^{(4)} d_5^{(4)} + a_6^{(4)} d_6^{(4)} + a_7^{(4)} d_7^{(4)} + a_8^{(4)} d_8^{(4)} \\ & + a_1^{(5)} d_1^{(5)} + O\left(\beta^6\right) \quad . \end{aligned} \tag{8.8}$$

In the limit of small β, we can expand

$$\log Z = x - \frac{x^2}{2} + \frac{x^3}{3} + \ldots \quad .$$

Since we are concerned with results up to $O\left(\beta^5\right)$, we only need to worry about the first term and

some parts of the second term. Using Eq. (8.8), we find

$$\begin{aligned}\log Z = \quad & a_1^{(2)} d_1^{(2)} + a_2^{(2)} d_2^{(2)} \\ & + a_1^{(4)} d_1^{(4)} + a_2^{(4)} d_2^{(4)} + a_3^{(4)} d_3^{(4)} + a_4^{(4)} d_4^{(4)} + a_5^{(4)} d_5^{(4)} \\ & + \left(a_6^{(4)} - \frac{a_1^{(2)} a_1^{(2)}}{2} \right) d_6^{(4)} + \left(a_7^{(4)} - a_1^{(2)} a_2^{(2)} \right) d_7^{(4)} + \left(a_8^{(4)} - \frac{a_2^{(2)} a_2^{(2)}}{2} \right) d_8^{(4)} \\ & + a_1^{(5)} d_1^{(5)} + O\left(\beta^6\right) \quad .\end{aligned}$$

After substituting the values given in Table 8.1, we get

$$F = \frac{3}{4}\beta_t^2 + \frac{1}{2}\beta_s^2 - \frac{3}{64}\beta_t^4 - \frac{2}{64}\beta_s^4 + \frac{1}{8}\beta_t^3\beta_s^2 + O\left(\beta^6\right) \quad . \tag{8.9}$$

Using the definition of the free energy (8.7) and the form of the partition function (8.4), we can see that

$$\langle \cos\theta_\square \rangle = \frac{1}{3}\frac{\partial F}{\partial \beta_t} \quad \text{and} \quad \langle \cos\theta_\triangle \rangle = \frac{1}{2}\frac{\partial F}{\partial \beta_s} \quad . \tag{8.10}$$

Hence, using the series (8.9), we find that

$$\langle \cos\theta_\square \rangle = \frac{1}{2}\beta_t - \frac{1}{16}\beta_t^3 + \frac{1}{8}\beta_t^2\beta_s^2 + O\left(\beta^5\right) \tag{8.11}$$

and

$$\langle \cos\theta_\triangle \rangle = \frac{1}{2}\beta_s - \frac{1}{16}\beta_s^3 + \frac{1}{8}\beta_t^3\beta_s + O\left(\beta^5\right) \quad . \tag{8.12}$$

Note that when $\beta_t = \beta_s$, both the spatial and temporal mean plaquette have the same value. This is striking because solely from the geometry, one would expect them to be different.

8.3 Numerical Simulation

We performed Monte Carlo simulations of this model on a 16^3 lattice with PBC. Each Monte Carlo sweep consisted of a Metropolis sweep and an OR sweep. We ran the simulation for 10^4 sweeps after 5000 thermalization sweeps to measure the mean plaquette. We also implemented the dual model on the honeycomb lattice. We simulated this model using Metropolis sweeps for 10^4 sweeps after 5000 thermalization steps. We set $\beta_s = \beta_t$.

Fig. 8.6 displays the plots of the spatial and temporal mean plaquettes for the LGT and dual model. We have also plotted the strong-coupling expansion value of the mean plaquette using Eqs.

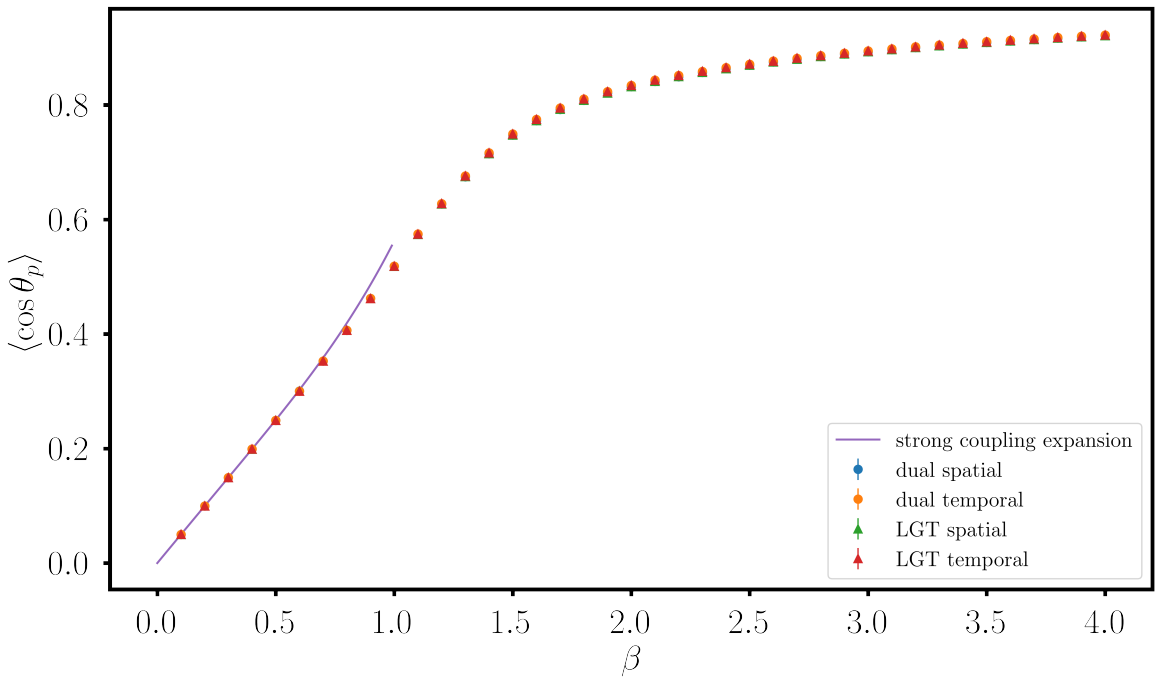

Figure 8.6: The mean plaquettes for the $U(1)$ LGT and the dual model. Note the agreement with the strong-coupling expansion.

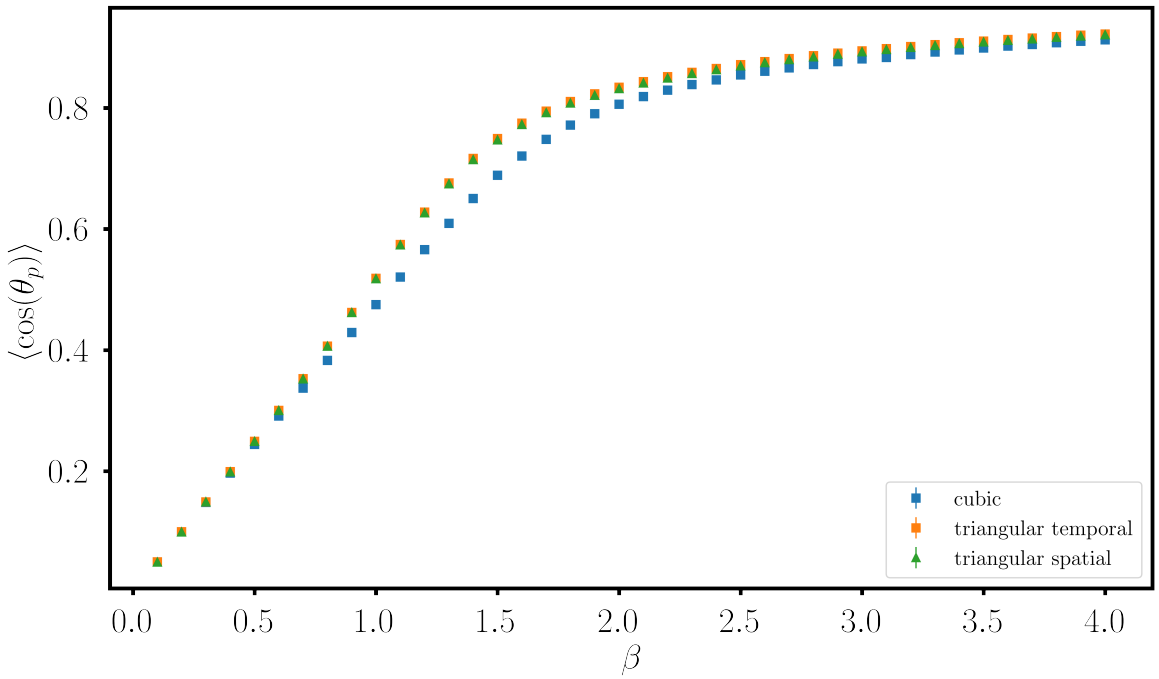

Figure 8.7: The mean plaquettes for the triangular and the cubic lattices.

(8.12) and (8.11). We can see that both of our simulations agree with the strong-coupling calculation. Significantly, we continue to see agreement between the different plaquettes at all coupling values.

We also compared the mean plaquette for the triangular lattice with the mean plaquette for the cubic lattice. This can be seen in Fig. 8.7. We see an agreement at large β which is what we expect from universality arguments. Interestingly, we also see an agreement for small β. This might be because at sufficiently small β, the system behaves like a free theory where all values of the plaquettes are equally probable.

Chapter 9

Conclusion and Further work

This chapter provides a summary of the topics covered in this thesis and gives an idea of further work that needs to be done.

Conclusion

- The formalism of lattice field theory was introduced. The $U(1)$ lattice gauge theory was discussed in detail and the expected behaviour was explained in terms of monopoles.
- An introduction to Markov chain Monte Carlo was provided. The Metropolis and overrelaxation algorithms used to perform the simulations were discussed.
- The $U(1)$ LGT with the extended action was introduced. Numerical simulations of the system were performed to develop intuition. Results from plaquette measurements gave a preliminary idea about the effect of the γ-term.
- A Kramers-Wannier type duality mapping was performed to map the $U(1)$ LGT to a dual integer-height model on the dual lattice.
- The effect of γ on the mass gap was studied by simulating the dual model. This effect was quantified by computing an effective coupling β^*.
- The $U(1)$ LGT was considered on a 3D 'triangular' lattice. The system was numerically simulated and the results for the plaquette were compared with results from the cubic lattice. A strong-coupling expansion calculation was performed to check the validity of our simulation.

Further Work

- We need to study the effect of γ on the string tension.
- We would like to analyse the dependence of β^* on β and γ. It would be interesting to check the agreement between the effective coupling computed from mass scaling and the effective coupling computed from string-tension scaling.
- The model needs to be analysed on the triangular lattice. It remains to be checked whether the scaling behaviours of the mass gap and the string tension on this lattice agree with the behaviour on the cubic lattice.

Appendix A

Differential Forms on the Lattice

This appendix introduces the notion of differential forms on lattice and defines the conventions to be used in the thesis. This discussion is based on the appendices of Sulejmanpasic and Gattringer [41], and Nguyen, Tanizaki, Ünsal [33]. The lattice differential forms formalism makes it very easy to perform lattice gauge theory manipulations. Although the below discussion will focus on 3-dimensional cubic (or triangular) lattice, the discussion holds for any d-dimensional lattice after suitable generalisation.

Consider a 3-dimensional cubic lattice Λ with periodic boundary conditions, where the lattice constant is set to 1. The lattice naturally decomposes into r-dimensional oriented *r-cells* $c^{(r)}$, with $r = 0, 1, 2, 3$. The 0-cells are the sites s, the 1-cells the links ℓ, the 2-cells the plaquettes p, and the 3-cells the elementary cubes (or prisms) c. We denote a particular r-cell $c^{(r)}$ 'attached' to a site x as $(x; \hat{\mu}_1 \dots \hat{\mu}_r)$. For instance, a link is given by $\ell = (x; \hat{\mu})$ and its oppositely oriented link is given by $-\ell = (x + \hat{\mu}; -\hat{\mu})$. Both of these correspond to the same unoriented edge of the lattice. By convention, when we write a sum or product over r-cells, we only sum over each unoriented cell.

The *boundary operator* ∂ maps an r-cell $c^{(r)}$ to the oriented sum of the $(r-1)$-cells making up its boundary. For example, it acts on a plaquette $(x; \hat{\mu}\hat{\nu})$ as

$$\begin{aligned} \partial(x; \hat{\mu}\hat{\nu}) &:= (x; \hat{\mu}) + (x + \hat{\mu}; \hat{\nu}) + (x + \hat{\mu} + \hat{\nu}; -\hat{\mu}) + (x + \hat{\nu}; -\hat{\nu}) \\ &= (x; \hat{\mu}) + (x + \hat{\mu}; \hat{\nu}) - (x + \hat{\nu}; \hat{\mu}) - (x; \hat{\nu}) \quad . \end{aligned} \tag{A.1}$$

The *coboundary operator* $\hat{\partial}$ maps an r-cell $c^{(r)}$ to the oriented sum of all the $(r+1)$-cells containing

$c^{(r)}$ in their boundary. For example, it acts on a plaquette $(x;\hat{\mu}\hat{\nu})$ as

$$\hat{\partial}(x;\hat{\mu}\hat{\nu}) := (x+\hat{\mu};\hat{1}\hat{2}\hat{3}) - (x;\hat{1}\hat{2}\hat{3}) \quad . \tag{A.2}$$

By convention, we set $\partial c^{(0)} = \hat{\partial} c^{(3)} = 0$.

We can naturally associate a *dual lattice* $\tilde{\Lambda}$ with the primary lattice Λ. It is a cubic lattice (or honeycomb lattice) that has its sites $\tilde{x}$ at the centres of the elementary cubes c (or prisms) of the primary lattice, i.e., $\tilde{x} = x + \frac{1}{2}(\hat{1}+\hat{2}+\hat{3})$. These two lattices are connected via the $*$ *dual operator* which maps an r-cell in the primary lattice to a $(3-r)$-cell in the dual lattice, and vice versa. For an r-cell $c^{(r)}$ in the primary lattice, $*c^{(r)}$ is the $(3-r)$-cell in the dual lattice such that $c^{(r)}$ and $*c^{(r)}$ intersect transversally. Taking the orientation into account, the square of the $*$ operator acting on an r-form is identity up to a sign:

$$*^2 = (-1)^{r(3-r)} \tag{A.3}$$

We define an *r-form* on the lattice ω to be a function which assigns a value $\omega_{c^{(r)}}$ to each r-cell $c^{(r)}$ in Λ. We are already familiar with a few lattice r-forms from Lattice Gauge Theory. For example, the link variable $\theta_\mu(x) = \theta_\ell$ is a 1-form with $\ell = (x;\hat{\mu})$. Note that $\omega_{-c^{(r)}} = -\omega_{c^{(r)}}$.

We define the *exterior derivative* operator d as the linear map which takes r-forms to $(r+1)$-forms as follows

$$(d\omega)_{c^{(r+1)}} := \sum_{c^{(r)} \subset \partial c^{(r+1)}} \omega_{c^{(r)}} \quad . \tag{A.4}$$

We can see that familiar plaquette operator in LGT $\theta_{\mu\nu}(x)$, which is a 2-form f_p, is in fact the exterior derivative of the link variable θ_ℓ,

$$f_p = (\mathrm{d}\theta)_p = \theta_\mu(x) + \theta_\nu(x+\hat{\mu}) - \theta_\mu(x+\hat{\nu}) - \theta_\nu(x) \quad . \tag{A.5}$$

We also define the *co-differential* $\mathrm{d}^\dagger$ as the linear map which takes r-forms to $(r-1)$-forms as

$$(\mathrm{d}^\dagger\omega)_{c^{(r-1)}} := \sum_{c^{(r)} \subset \hat{\partial} c^{(r-1)}} \omega_{c^{(r)}} \quad . \tag{A.6}$$

It can be seen that $\mathrm{d}^2 = \mathrm{d}^{\dagger 2} = 0$. Additionally, the star operator $*$ induces a map from r-forms on Λ to $(3-r)$-forms on $\tilde{\Lambda}$, and vice versa, as

$$(*\omega)_{c^{(3-r)}} := \omega_{*c^{(3-r)}} \quad . \tag{A.7}$$

Using the analogous relation for r-cells (A.3) , it can be seen that

$$*^2\,\omega_{c^{(r)}} = (-1)^{r(3-r)}\omega_{c^{(r)}} \quad . \tag{A.8}$$

Note that $*\mathrm{d} = \mathrm{d}^\dagger *$.

We can define an inner-product on the space of r-forms as follows:

$$(\omega, \tau) := \sum_{c^{(r)}} \omega_{c^{(r)}}\tau_{c^{(r)}} \quad . \tag{A.9}$$

The exterior derivative operator d and the co-differential operator $\mathrm{d}^\dagger$ are dual to each other with respect to this inner-product. This means that they obey the *partial integration formula*

$$\sum_{c^{(r)}} (\mathrm{d}\omega)_{c^{(r)}}\tau_{c^{(r)}} = (-1)^r \sum_{c^{(r)}} \omega_{c^{(r-1)}}(\mathrm{d}^\dagger\tau)_{c^{(r-1)}} \quad . \tag{A.10}$$

This is the most useful feature of the lattice forms notation which allows us to 'integrate by parts' mechanically.

There is also a lattice analogue of the *Hodge Decomposition*. It states that for any r-form $\omega_{c^{(r)}}$, there exist an $(r-1)$-form $\alpha_{c^{(r-1)}}$, an $(r+1)$-form $\beta_{c^{(r+1)}}$ and a *harmonic* r-form $\eta_{c^{(r)}}$ obeying $\mathrm{d}\eta = \mathrm{d}^\dagger\eta = 0$, such that

$$\omega = \mathrm{d}\alpha + \mathrm{d}^\dagger\beta + \eta \quad . \tag{A.11}$$

References

[1] Alexander Polyakov. *Interview with Alexander Polyakov*. 2003. URL: https://wayback.archive-it.org/9060/20230418132451/https://authors.library.caltech.edu/5456/1/hrst.mit.edu//hrs/renormalization/Polyakov/index.html (visited on 03/25/2024).

[2] Kenneth G. Wilson. "Confinement of quarks". In: *Phys. Rev. D* 10.8 (Oct. 1974). Publisher: American Physical Society, pp. 2445–2459. DOI: 10.1103/PhysRevD.10.2445.

[3] A. M. Polyakov. "Compact gauge fields and the infrared catastrophe". In: *Physics Letters B* 59.1 (Oct. 1975), pp. 82–84. ISSN: 0370-2693. DOI: 10.1016/0370-2693(75)90162-8.

[4] A. M. Polyakov. "Quark confinement and topology of gauge theories". In: *Nuclear Physics B* 120.3 (Mar. 1977), pp. 429–458. ISSN: 0550-3213. DOI: 10.1016/0550-3213(77)90086-4.

[5] T. Banks, R. Myerson, and J. Kogut. "Phase transitions in Abelian lattice gauge theories". In: *Nuclear Physics B* 129.3 (Oct. 1977), pp. 493–510. ISSN: 0550-3213. DOI: 10.1016/0550-3213(77)90129-8.

[6] Markus Göpfert and Gerhard Mack. "Proof of confinement of static quarks in 3-dimensionalU(1) lattice gauge theory for all values of the coupling constant". en. In: *Commun.Math. Phys.* 82.4 (Jan. 1982), pp. 545–606. ISSN: 0010-3616, 1432-0916. DOI: 10.1007/BF01961240.

[7] K. R. Ito. "Upper and lower bound for the string tension in the three-dimensional lattice quantum electrodynamics". In: *Nuclear Physics B* 205.3 (June 1982), pp. 440–448. ISSN: 0550-3213. DOI: 10.1016/0550-3213(82)90368-6.

[8] Mushtaq Loan et al. "Path Integral Monte Carlo Approach to the U(1) Lattice Gauge Theory in (2+1) Dimensions". In: *Phys. Rev. D* 68.3 (Aug. 2003). arXiv:hep-lat/0209159, p. 034504. ISSN: 0556-2821, 1089-4918. DOI: 10.1103/PhysRevD.68.034504.

[9] Andreas Athenodorou and Michael Teper. "On the spectrum and string tension of U(1) lattice gauge theory in 2+1 dimensions". In: *J. High Energ. Phys.* 2019.1 (Jan. 2019). arXiv:1811.06280 [hep-lat], p. 63. ISSN: 1029-8479. DOI: 10.1007/JHEP01(2019)063.

[10] Mari Carmen Bañuls et al. "Simulating lattice gauge theories within quantum technologies". en. In: *Eur. Phys. J. D* 74.8 (Aug. 2020), p. 165. ISSN: 1434-6079. DOI: 10.1140/epjd/e2020-100571-8.

[11] Alberto Di Meglio et al. "Quantum Computing for High-Energy Physics: State of the Art and Challenges. Summary of the QC4HEP Working Group". In: (July 2023). arXiv: 2307.03236 [quant-ph].

[12] Christian W. Bauer et al. "Quantum simulation of fundamental particles and forces". In: *Nature Rev. Phys.* 5.7 (2023), pp. 420–432. DOI: 10.1038/s42254-023-00599-8.

[13] Robert Socolow. *Reminiscences of Sidney Coleman*. URL: https://web.archive.org/web/20190415092256/http://media.physics.harvard.edu/QFT/PDFs/Letters-to-Sidney.pdf.

[14] Michael Creutz. *Quarks, Gluons and Lattices*. Cambridge Monographs on Mathematical Physics. Cambridge: Cambridge University Press, 2023. ISBN: 978-1-00-929038-8. DOI: 10.1017/9781009290395.

[15] Jan Smit. *Introduction to Quantum Fields on a Lattice*. Cambridge Lecture Notes in Physics. Cambridge: Cambridge University Press, 2002. ISBN: 978-0-521-89051-9. DOI: 10.1017/CBO9780511583971.

[16] Christof Gattringer and Christian B. Lang. *Quantum Chromodynamics on the Lattice: An Introductory Presentation*. en. Vol. 788. Lecture Notes in Physics. Berlin, Heidelberg: Springer, 2010. ISBN: 978-3-642-01849-7 978-3-642-01850-3. DOI: 10.1007/978-3-642-01850-3.

[17] Thomas DeGrand and Carleton DeTar. *Lattice Methods for Quantum Chromodynamics*. WORLD SCIENTIFIC, 2006. DOI: 10.1142/6065.

[18] Debashish Chowdhury and Dietrich Stauffer. *Principles of Equilibrium Statistical Mechanics*. First Edition. Wiley-VCH, 2000. Chap. 7. ISBN: 3-527-40300-0.

[19] S. Elitzur. "Impossibility of spontaneously breaking local symmetries". In: *Phys. Rev. D* 12.12 (Dec. 1975). Publisher: American Physical Society, pp. 3978–3982. DOI: 10.1103/PhysRevD.12.3978.

[20] David Tong. *Lectures on Gauge Theory*. https://www.damtp.cam.ac.uk/user/tong/gaugetheory.html.

[21] Christian Borgs and Erhard Seiler. "Quark deconfinement at high temperature: A rigorous proof". In: *Nuclear Physics B* 215.1 (Jan. 1983), pp. 125–135. ISSN: 0550-3213. DOI: 10.1016/0550-3213(83)90270-5.

[22] John B. Kogut. "An introduction to lattice gauge theory and spin systems". In: *Rev. Mod. Phys.* 51.4 (Oct. 1979). Publisher: American Physical Society, pp. 659–713. DOI: 10.1103/RevModPhys.51.659.

[23] Alan D. Sokal. *Monte Carlo Methods in Statistical Mechanics: Foundations and New Algorithms*. 1997.

[24] Colin Morningstar. *The Monte Carlo method in quantum field theory*. arXiv:hep-lat/0702020. Feb. 2007. DOI: 10.48550/arXiv.hep-lat/0702020.

[25] James P. Sethna. *Statistical Mechanics: Entropy, Order Parameters, and Complexity*. Second Edition. Oxford Master Series in Physics. Oxford, New York: Oxford University Press, Mar. 2021. ISBN: 978-0-19-886525-4.

[26] Nicholas Metropolis et al. "Equation of State Calculations by Fast Computing Machines". en. In: *The Journal of Chemical Physics* 21.6 (June 1953), pp. 1087–1092. ISSN: 0021-9606, 1089-7690. DOI: 10.1063/1.1699114.

[27] Michael Creutz. "Overrelaxation and Monte Carlo simulation". en. In: *Phys. Rev. D* 36.2 (July 1987), pp. 515–519. ISSN: 0556-2821. DOI: 10.1103/PhysRevD.36.515.

[28] Gyan Bhanot. "Compact QED with an extended lattice action". In: *Nuclear Physics B* 205.2 (May 1982), pp. 168–172. ISSN: 0550-3213. DOI: 10.1016/0550-3213(82)90382-0.

[29] Isabel Campos, Andres Cruz, and Alfonso Tarancon. "A study of the phase transition in 4D pure compact U(1) LGT on toroidal and spherical lattices". In: *Nuclear Physics B* 528.1-2 (Sept. 1998). arXiv:hep-lat/9803007, pp. 325–354. ISSN: 05503213. DOI: 10.1016/S0550-3213(98)00452-0.

[30] Michele Vettorazzo and Philippe de Forcrand. "Electromagnetic fluxes, monopoles, and the order of the 4d compact U(1) phase transition". In: *Nuclear Physics B* 686.1-2 (May 2004). arXiv:hep-lat/0311006, pp. 85–118. ISSN: 05503213. DOI: 10.1016/j.nuclphysb.2004.02.038.

[31] R. Balian, J. M. Drouffe, and C. Itzykson. "Gauge fields on a lattice. III. Strong-coupling expansions and transition points". In: *Phys. Rev. D* 11.8 (Apr. 1975). Publisher: American Physical Society, pp. 2104–2119. DOI: 10.1103/PhysRevD.11.2104.

[32] Roger Horsley and Ulli Wolff. "Weak coupling expansion of Wilson loops in compact QED". In: *Physics Letters B* 105.4 (Oct. 1981), pp. 290–296. ISSN: 0370-2693. DOI: 10.1016/0370-2693(81)90891-1.

[33] Mendel Nguyen, Yuya Tanizaki, and Mithat Ünsal. "Semi-Abelian gauge theories, non-invertible symmetries, and string tensions beyond N-ality". In: *J. High Energ. Phys.* 2021.3 (Mar. 2021). arXiv:2101.02227 [hep-lat, physics:hep-th], p. 238. ISSN: 1029-8479. DOI: 10.1007/JHEP03(2021)238.

[34] Robert Savit. "Duality in field theory and statistical systems". In: *Rev. Mod. Phys.* 52.2 (Apr. 1980). Publisher: American Physical Society, pp. 453–487. DOI: 10.1103/RevModPhys.52.453.

[35] L. Polley and U. -J. Wiese. "Monopole condensate and monopole mass in U(1) lattice gauge theory". en. In: *Nuclear Physics B* 356.3 (June 1991), pp. 629–654. ISSN: 0550-3213. DOI: 10.1016/0550-3213(91)90380-G.

[36] Alessandro Mariani et al. "A new type of lattice gauge theory through self-adjoint extensions". In: *PoS* LATTICE2022 (2023), p. 377. DOI: 10.22323/1.430.0377. arXiv: 2210.11154 [hep-lat].

[37] Marco Panero. "A numerical study of confinement in compact QED". In: *J. High Energy Phys.* 2005.05 (May 2005). arXiv:hep-lat/0503024, pp. 066–066. ISSN: 1029-8479. DOI: 10.1088/1126-6708/2005/05/066.

[38] Richard C. Brower, David Berenstein, and Hiroki Kawai. *Lattice Gauge Theory for a Quantum Computer*. arXiv:2002.10028 [hep-lat, physics:quant-ph]. Feb. 2020.

[39] Emilie Huffman, Miguel García Vera, and Debasish Banerjee. "Toward the real-time evolution of gauge-invariant ${\mathbb{Z}}_{2}$ and $U(1)$ quantum link models on noisy intermediate-scale quantum hardware with error mitigation". In: *Phys. Rev. D* 106.9 (Nov.

2022). Publisher: American Physical Society, p. 094502. DOI: 10.1103/PhysRevD.106.094502.

[40] D. Banerjee et al. "Nematic confined phases in the U(1) quantum link model on a triangular lattice: Near-term quantum computations of string dynamics on a chip". en. In: *Phys. Rev. Research* 4.2 (June 2022), p. 023176. ISSN: 2643-1564. DOI: 10.1103/PhysRevResearch.4.023176.

[41] Tin Sulejmanpasic and Christof Gattringer. "Abelian gauge theories on the lattice: θ-terms and compact gauge theory with(out) monopoles". In: *Nuclear Physics B* 943 (June 2019). arXiv:1901.02637 [cond-mat, physics:hep-lat, physics:hep-th], p. 114616. ISSN: 05503213. DOI: 10.1016/j.nuclphysb.2019.114616.